A Thesis Submitted for the Degree of PhD at the University of Warwick

Permanent WRAP URL:

http://wrap.warwick.ac.uk/169291
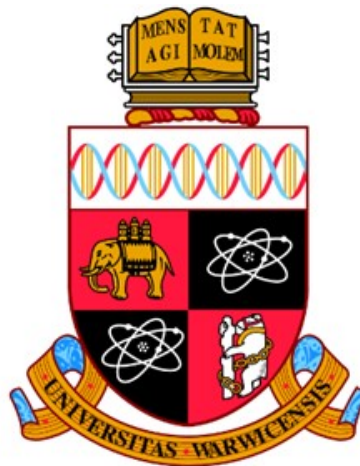
warwick.ac.uk/lib-publications

Fluxing Behaviour - Reactions Between Iron Ore and Fluxing Agents in the Cyclone Converter Furnace of Hlsarna

by

James C. Whiston

A thesis submitted in part fulfilment for the

degree of Doctor of Philosophy in Engineering

University of Warwick

Warwick Manufacturing Group

2021

Contents

List of Figures

List of Tables

Acknowledgments

There are many people who without their aid this thesis would not have come to fruition. To these people I would like to express my thanks.

Firstly, I would like to thank Dr Zushu Li for his supervision throughout my project. He always made time for my work and allowed me to follow my own path towards my goals.

I would also like to thank Dr Stephen Spooner. Your enthusiasm in the beginning stages of my time at WMG went far beyond the role of research fellow. You pushed me to always be better and you were always available to talk through even the craziest of ideas. It was a pleasure to work with you and you have become a close friend. You will always be welcome for a cup of tea with biscuits and cake.

I would like to express my gratitude to Mr Koen Meijer and Dr Hans Hage and the rest of the Tata Steel Europe HIsarna team for the materials you have sent for this project and for always giving an interesting update of the goings on of the HIsarna pilot plant. You have always been welcoming and engaging with the technical questioning of my work. I hope all your hard work on HIsarna allows the process to reach its potential. I also hope we can have a bowling rematch at some point.

Thank you to all my colleagues at WMG past and present for your aid in my work, to name a few, Dr Geoff West, Mr Darbaz Khasraw, Miss Theint Htet, Mr Michael Green, Mr Stephen Hewitt, Miss Chloe Patel and Dr Sam Marks. Your technical advice, help, support, and chats over coffee/tea has been greatly appreciated over the course of the project. I would also like to add special thanks to Professor Claire Davis and Dr Carl Slater. You allowed me to widen my knowledge

List of Publications

Parts of this thesis have been published by the author:

1. Whiston, J., Spooner S., Meijer K., and Li Z., "Observation of the Reactions between Iron Ore and Metallurgical Fluxes for the Alternative Ironmaking HIsarna Process". Iron and Steelmaking. (Accepted June 2021)

Parts of this work was also presented at conference:

1. Whiston, J., Spooner S., Meijer K., and Li Z. 2019, "Observation of the Reaction between Iron Ore and Metallurgical Fluxes for Improved Pre-reduction", Advanced real time imaging, TMS, 12th March, San Antonio Texas.

   Whiston, J., Spooner S., Meijer K., and Li Z. 2019, "Observation of the Reaction between Iron Ore and Metallurgical Fluxes for Improved Pre-reduction", Advanced Real Time Imaging, TMS, 12th March, San Antonio Texas. (Awarded Third Place Prize for "Best Oral Presentation Competition" in the Advanced Real Time Imaging symposium)

List of Abbreviations

BF	Blast Furnace
BOF	Basic Oxygen Furnace
BOS	Basic Oxygen Steelmaking
C_2S	Di-calcium silicate
$C_2S - C_3P$	Di-calcium silicate-calcium phosphate
CaL	Calcium Looping
CANMET	Canada Centre of Mineral and Energy Technology
CBF	Converted Blast Furnace
CCF	Cyclone Converter Furnace
CCS	Carbon Capture & Storage
DRI	Direct Reduced Iron
DSC	Differential Scanning Calorimetry
EAF	Electric Arc Furnace
EU	European Union
FEG-SEM	Field Emission Scanning Electron Microscope
HRDF	HIsmelt Research and Development Facility
HT-CSLM	High Temperature Confocal Scanning Laser Microscope
HTF	Horizontal Tube Furnace
INCAR	Carbon Science and Technology Institute
IR	Infrared Radiation
ITRI	Industrial Technology Research Institute
JSPL	Jindal Steel and Power Limited
MoU	Memorandum of Understanding
MS	Mass Spectroscopy
SDC	Sessile drop camera
SEM	Scanning Electron Microscopy
SRV	Smelting Reduction Vessel
ULCORED	Ultra Low CO_2 Direct Reduction
ULCOS	Ultra Low CO_2 Steelmaking
ULCOWIN	Ultra Low CO_2 Electrowinning
XCT	X-ray Computer Tomography

Declarations

This thesis is submitted to the University of Warwick in support of my application for the degree of Doctor of Philosophy. It has been composed by myself and has not been submitted in any previous application in my degree. The work presented (including the data collection and generation) was carried out by the author except for the case below.

- X-ray Computed Tomography scanning and image analysis was carried out by Dr Guillaume Remy.

Abstract

Steel is under increasing pressure from governments and environmental groups to cut CO_2 emissions. To fight this, a number of alternative ironmaking processes have been devised to replace the blast furnace (BF) ironmaking process in modern integrated steel plants. The blast furnace has been targeted, as it is the highest producer of greenhouse gases in the steel plant. This is due to the high use of coal as an active ingredient and the energy intensive processing of raw materials for use in the furnace such as coking ovens and sintering. Tata Steel Europe have been developing an alternative iron making plant called HIsarna that is a combination of two technologies: cyclone converter furnace and HIsmelt smelting reduction vessel. The trials have shown that the process can cut CO_2 emissions drastically compared to the current BF ironmaking and has greater flexibility in the raw materials and energy used for the process.

With the development of new processes, the issues that arise from new reactions means that new fundamental knowledge is needed to understand the certain phenomena in the. In this thesis, the interaction between iron ore and Ca-based materials (lime, limestone, and basic oxygen steelmaking slag) will be studied with an interest of these reactions occurring in the CCF. The process has seen issues of accretions building up in the region between the CCF and SRV, and requires a solution to dissuade the agglomeration of such accretions.

The accretions found in the process were taken from the IJmuiden HIsarna pilot plant and analysed by examining the structure, composition, and thermal properties. The structure and porosity were examined with XCT and microscopy.

The sample had two defined sections (dense and porous) with some microstructural aspects. The composition was detected by electron dispersal spectroscopy (EDS) and was used to study the chemistry of the accretion against the iron ore used in HIsarna. The thermal properties indicated the temperature at what temperature the material will be molten to understand and stop the accretion forming. The results allowed for the orientation of the accretion to be determined and theories on how the formation of the accretion. It shows that how the classic formation via alkalis of accretions found in a BF do not seem feasible due to the higher temperatures in the HIsarna.

The interactions between iron ore and Ca-based materials were then conducted with the aim to show the benefits of doping the CCF with CaO to reduce the melting point of the ore to increase fluidity. To increase HIsarna's flexibility of raw materials, three Ca-based fluxes (lime, limestone and BOF slag) were compared to show how they work in terms of reactivity and effectiveness in increasing the molten material. This was done with in situ experimentation and post experimental analysis of the flux-iron ore interface. The finding showed that limestone was the most reactive from the test with a high molten fraction and evidenced from SEM imaging. The BOF slag was also showed to be a potential source of fluxing material in the HIsarna process. Using BOF slag would help increase the environmental benefits to the process and industry as this promotes recycling of BOF slag produced in an integrated plant.

Finally, the study progresses from small scale bulk reactions to a single particle reaction with a Ca based pellet (lime and limestone) to test likelihood of how the particles react in the CCF. This allowed for a more varied compositions of iron ore due to the heterogeneous nature of particles to be studies with higher content of impurities such as SiO_2, Al_2O_3 and MgO. The test used a unique method implementing a sessile drop camera (SDC) with the high temperature confocal scanning laser microscope (HT-CSLM) to obtain a two-plane in situ view of a particle interacting at high temperatures. The test showed that a high SiO_2 content in the particle increased the melting point of a $CaO-FeO_x$ system. Al_2O_3/MgO also ef-

fected the interaction negatively but by a smaller degree. The visualisation from two angles allowed the particle to be measured over a period of 60 s and allowed for a kinetic study of the interaction. This found that the composition of each particle had a greater effect on the rate of reaction rather than the shape, size, and temperature. It also provided further evidence of the increased activity of newly formed CaO from calcination of limestone.

Chapter 1

Introduction

The indispensable nature of steel within our modern society becomes apparent when considering the vast industries reliant upon its production; these include major applications in construction, mechanical engineering, white goods production, automotive industry, oil and gas, and aerospace. Due to the uptake of iron and steel production processes by the sector globally, multiple steps of the steel manufacturing process consume high amount of carbon as fuels and reaction agents resulting in the steel industry producing 1.878 billion tons of crude steel in 2020 according to the world steel association. With a CO_2 emission per tonne of steel being around 2 2.2 tonnes via the integrated steel plant and equates to 3.756-4.136 billion tonnes of CO_2 produced by the steel industry[1]. This amount of CO_2 emission is approximately 7 % of the CO_2 emissions produced globally [2] and is unsustainable for the steel industry. These figures have resulted in the EU to issue a challenge to cut CO_2 emissions by 80 % to 95 % by 2050 [3] compared to the 1990 level.

Each step of the integrated BF-BOF (basic oxygen furnace) steelmaking process contributes to the emissions of the overall process. Figure 1-1 [4], shows each part of the integrated steelmaking process and its CO_2 emissions with the blast furnace (BF), coke making and sintering producing the most. The current BF ironmaking process is energy efficient but energy intensive and accounts for around 69 % of CO_2 emissions of the whole BF-BOF integrated steel manufacturing process.

72 kWh
138 kg scrap

coal = 1710 kgCO₂
limestone = 105 kgCO₂ → total CO₂ emission:
1815 kg/t rolled coil

288 kg
5-10% CO₂

BF gas

1255 kg CO₂-e
in BF gas

709 kg
20% CO₂

CO₂

coal 12 kg
limestone 133 kg

329 kg
25% CO₂

CO₂

CO₂

blast
furnace
hot blast

stoves

power
plant

sinter strand
pellet plant

coke

coal
187 kg

57 kg
30% CO₂

84 kg
10% CO₂

CO₂

CO₂

285 kg
25% CO₂

CO₂

hot strip
mill

lime kiln

coke
oven gas

flares, etc
63 kg

converter gas

coke
plant

steel
plant

limestone
109 kg

coal
382 kg

carbon-bearing materials

CO₂ emissions expressed as volume (kg/t
rolled coil) and concentration in flue gas (vol%)

Figure 1-1: Flow diagram of the integrated steel making process with figures of the input of coal or coke and the output of CO_2 from each step from data from 2012. [4]

The challenge to substantially reduce CO_2 emissions from the steel industry has increased the activity in research and development on more sustainable ways of producing liquid iron instead of BF process. Meanwhile, the fast-increasing demand in steel in China, India and other growing Asian countries has led to an increase in the price of raw materials on international market and the shortfall of premier iron ore. These reasons cause a desire to find an alternative ironmaking process that can substantially reduce CO_2 emissions and to reduce the cost of raw materials by using flexible raw materials.

The HIsarna technology offers great potential to be flexible in raw materials and energy sources and to substantially reduce CO_2 emissions from ironmaking process. HIsarna process is a combination of Rio Tinto's HIsmelt SRV [5] and Tata Steel's CCF [6]. It is one of the four technologies (the other three are top gas recycling, ULCORED and ULCOWIN) identified by the EU ULCOS programme since its start-up in 2004. Although so far it has gone through five successful cam-

paigns, there is a serious lack of fundamental understanding of mechanisms involved in the new technology. Uncovering the fundamental mechanisms of the reactions in the HIsarna process will greatly accelerate the development and upscaling of the promising technology.

In 2017, it was reported that globally the production of lime (CaO) is estimated to be 350 million tons with the steel industry using between 140 to 160 million tons. The EU uses 20 million tons of lime with 40 % being consumed by the iron and steel industry [7]. Most lime is produced at steel mills from the calcination of limestone. Lime in the iron making industry is known as a fluxing agent and is used as a chemical cleaner to remove unwanted materials [8]. The removed are silica, alumina, sulphur and phosphorous, and the chemical equations of each can be presented below in equations (1.1a - 1.1d).

$$2SiO_2 + 5CaO \rightarrow (Ca_2SiO_4) + (Ca_3SiO_5), \tag{1.1a}$$

$$9Al_2O_3 + 16CaO \rightarrow (CaAl_2O_4) + (Ca_3Al_2O_6) + (Ca_{12}Al_{14}O_{33}) \tag{1.1b}$$

$$2S + 2CaO \rightarrow 2CaS + O_2 \tag{1.1c}$$

$$2P + 3CaO + 5FeO \rightleftharpoons 3CaO \cdot P_2O_5 + 5Fe \tag{1.1d}$$
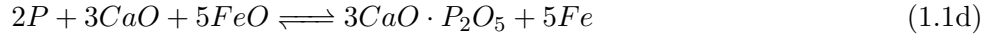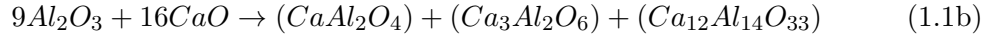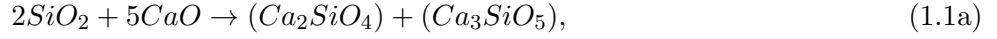
Lime is also used by the steel industry in forming sinters in the iron making process as a binding agent and aids the quality of the sinter. This is due to its ability to form a uniform blend, which influences the permeability of the charge and increases the heat transfer. It is suggested that lime doping during the sinter process can increase the productivity of the process by 20 % and reduce the costs, raw materials used and CO_2 of the process [9].

1.1 Objectives of Study

The objective of this study is to investigate how using lime based fluxing agents in the HIsarna process can benefit and offer fundamental understanding of the interactions between lime based fluxing agents and HIsarna raw materials (e.g., iron ore) that are likely to occur. This will include the introduction of such lime into the CCF where it will interact solely with the iron ore. Understanding the reaction between iron ore and CaO will offer insight into the potential benefits and drawbacks of lime charging in the CCF.

First, the potential benefits of the lime addition (injection to CCF) will be studied on the build up of accretions in the HIsarna process. This will be studied by

analysing an accretion sample taken from the HIsarna plant IJmuiden, in terms of composition, structure and properties, using microscopy, X-ray Computed Tomography (XCT) and calculations from the software FactSage^{TM}, and then theorising the growth of accretions in the process and how fluxing can change/ avoid it.

Further study of the reaction kinetics between iron ore and different fluxing agents (lime, limestone and BOF slag) will be carried out using the High Temperature Confocal Scanning Laser Microscope (HT-CSLM). Three fluxing materials will be compared by testing the properties of each and judging the viability and effectiveness of each material in terms of interaction with iron ore in HIsarna.

A novel study of a single particle from iron ore reacting with a fluxing agent will be developed to allow for a full investigation of the interaction between iron ore and fluxing materials. Using a Sessile Drop Camera (SDC) with the HT-CSLM, the particle (iron ore) can be viewed in two planes and the spread of a molten particle (iron ore) on the fluxing surface can be measured. This will provide important information to HIsarna process on the viability of other Ca based fluxing agents, the understanding of the reaction kinetics, and the optimal conditions that can alter the process.

1.2   Thesis Structure

Following this introduction, the layout of the thesis will be as followed.

Chapter 2 is "Literature Review". This chapter will examine the current integrated steel plant as well as new alternative ironmaking processes including HIsarna, COREX$^{®}$ and FINEX$^{®}$. It will then examine such topics as dissolution of fluxing agents into slags, key thermodynamic models, unique lime use and studies on reactivity and Kinetic models such as the shrinking sphere model.

Chapter 3 is "Hypothesis". The hypotheses are identified with reasons gained from the previous chapter (Chapter 2: Literature Review) and how they will be investigated.

Chapter 4 "Materials" and Chapter 5 "Equipment" shows and describes the materials and equipment used throughout this body of work, and more in-depth descriptions of the experimental.

Chapter 6 is "Characterisation of an Accretion Sample Taken from HIsarna Pilot Plant to Investigate the Agglomeration in the CCF". This chapter will analyse the accretion sample taken from HIsarna plant, evaluate the properties, and use literature to determine possible explanations for growth/build-up. In addition, how the use of fluxing agents can solve the build-up of such material.

Chapter 7 is "Observation of the Reactions between Iron Ore and Metallurgical Fluxes for the Alternative Ironmaking HIsarna Process". This chapter tests three different fluxing agent against each other in terms of interactions and viability as an alternative to quick lime in HIsarna. With a kinetic study gained from SEM analysis of post experimental samples.

Chapter 8 is "Investigation into the effect of Iron Ore Particle Composition on the Melting and Fluxing Behaviour with Calcium Oxide and Limestone". This chapter investigates how different compositions in an iron ore can affect the interaction with a fluxing material and a full kinetic study of a particle using a novel in situ experimentation.

Finally, Chapter 9 "Conclusion" and Chapter 10 "Future Work" will bring together the findings of the research in the thesis and comment on the impact they can have on the HIsarna process. In addition, it will suggest ways to continue the work and to guide any further development, and greater understanding of the ideas that are presented.

Chapter 2

Literature Review

2.1 Modern Integrated Steel Plant

The modern integrated steel plant refers to a steel plant consisting of BF ironmaking (including coke making and sintering) and basic oxygen steelmaking (BOS), in comparison to the mini mill of EAF steelmaking process. The BF-BOF integrated process produced 74.2 % of the world crude steel in 2015 with the EAF producing 25.2 % [10].
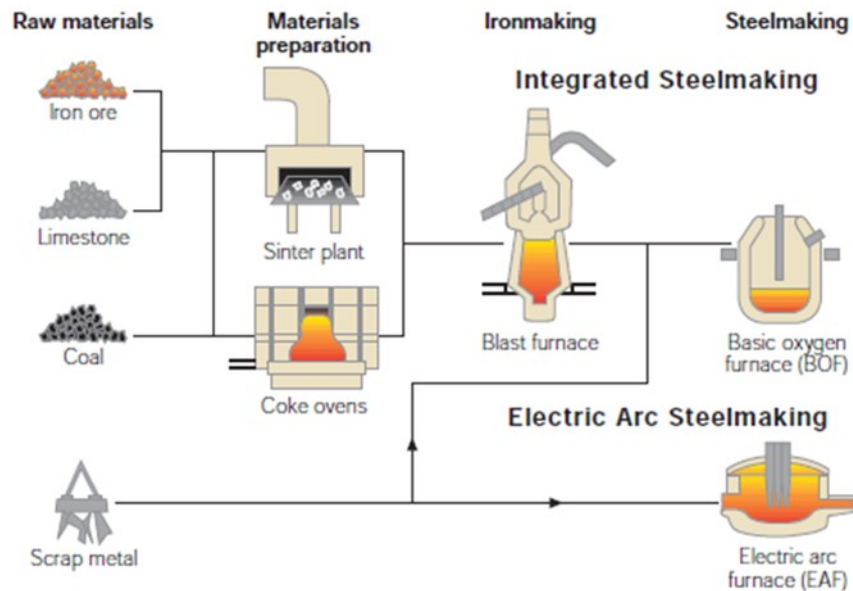
Figure 2-1: A flow diagram of the integrated steel plant with EAF plant [11].

The BF ironmaking process produces hot metal by using coke from coke

6

making step and sinters of iron ore from sintering step [11]. The BF ironmaking process is unable to utilise non-coking coal (which is much cheaper and widely available than coking coal) and unprepared iron ore. The BOS process produces crude steel by blowing supersonic oxygen into the hot metal in the BOF converter. On the contrary, the mini mill produces crude steel in the electric arc furnace by using scraps and direct reduced iron (DRI) as raw metal materials.

2.1.1 Coke Making

Coke is a purified form of coking coal; it is produced in an oven through loading of coal and heating to 1100 °C under an oxygen deficient atmosphere [12]. This softens the coal and once cooled, hard porous lumps are left.

The reason for this process is to remove some major impurities (moisture, volatile matter, etc.) that would affect the overall performance of the coal in iron making. The heat removes most of the impurities and leaves a carbon-rich coke.

Coke has three specific / important roles in the BF ironmaking. Firstly, the coke acts as a reducing agent by producing carbon monoxide through combustion which, reacts with iron oxides to form metallic iron [13].

$$Fe_nO_m + mC \rightarrow nFe + mCO \tag{2.1a}$$

$$Fe_nO_m + mCO \rightarrow nFe + mCO_2 \tag{2.1b}$$

Secondly, the combustion of coke acts as a heat source for the furnace, providing the high temperatures required for the melting of iron and slag. In addition, as the reduction of iron oxide is an endothermic reaction, the heat from the combustion of coke will help drive the reaction to completion. Finally and most importantly, it provides a physical support for the burden as a permeable matrix through which gases and liquids can pass allowing for separation [14].

Coke is produced in a coke battery which contains multiple coke ovens stacked in rows, the coke is loaded and baked for 28 hours [15]. These chambers usually have a width range of 450-600 mm, a height of 4-8 m and a length of 12-18 m. These dimensions correspond to a volume of between 40-70 m^3 which equates to a production range from 6,200 to 17,000 t/year or 25 to 36 kg m^{-3}h^{-1} [16]. The heat permeates the chamber from the outside and causes the coking process to instigate which is dependent on the temperature of the chamber. The general trend of behaviour with respect to temperature is outlined below [17]:

A. <100 °C - The coal blend is dried (hydroscopic water is evaporated).

B. 100-350 °C - Absorbed gases such as nitrogen, methane and carbon dioxide are extracted, and the coal is dehydrated. Above 250 °C, the first products of thermal decomposition appear.

C. 350-480 °C - The coal loses its strength, and its plastic properties appear; the coal swells which leads to the porous structure of the final product. At these temperatures bitumen is evaporated.

D. 480-600 °C - Semi-coke is formed. The crack distribution is determined due to shrinkage.

E. 600-1100 °C - Final coke is formed.

The lettering of the list corresponds to those shown in Figure 2-2, depicting what happens at the given temperatures in the chambers [18].
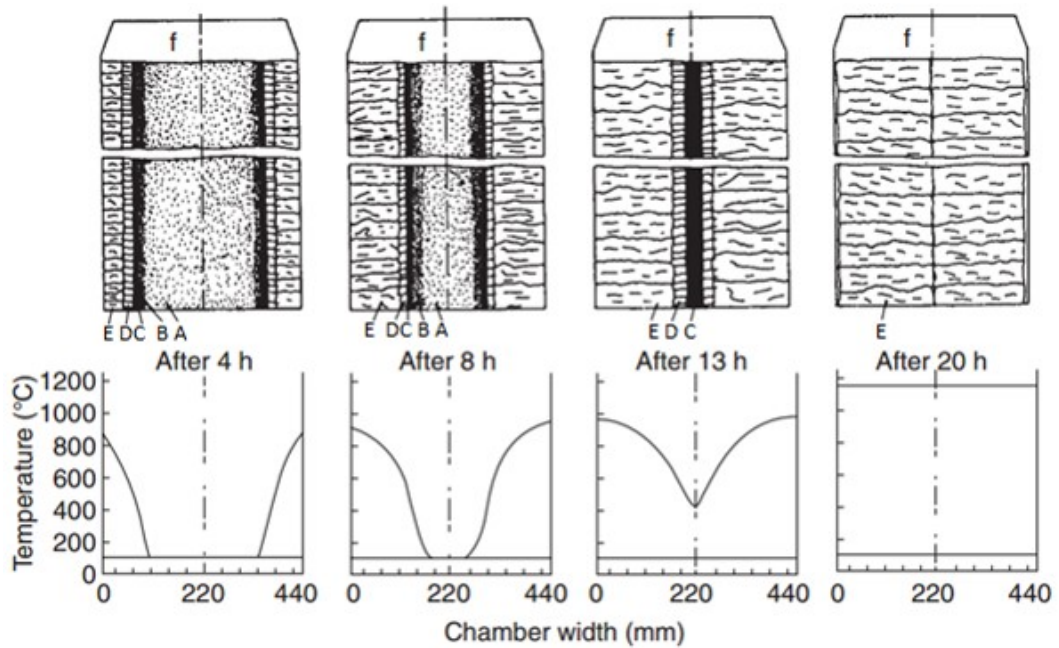
Figure 2-2: A schematic of a cross section of a coke oven at different times of the process with corresponding temperature analysis of the cross sections. [18]

Coking coal is a highly sought-after resource especially in the steel making industry however it is dependent on the source and market fluctuations. For example, India had shortage issues during 2011-2012 as the demand for coal was projected to be 731 million tonnes over these years [19]. Therefore, the desire to remove coking

8

from the integrated process is of great interest to the industry. Removing this will cut CO_2 emissions as Coking contributes to 5 % of the overall CO_2 emission from the BF method of steel manufacturing [20]. The possible fuel flexibility in iron-making process will allow for lower costings due to the choice for fuel and ability to switch to a cheaper alternative fuel.

2.1.2 Blast Furnace Ironmaking

The BF is currently responsible for producing 95 % of liquid iron used around the world, however this is predicted to reduce to 60 % by 2050. This reduction is because of harsher climate laws / environmental regulations, which accelerate other processes being discovered and introduced commercially [21]. Currently the BF ironmaking step including coke making and sintering contributes 69 % of all the CO_2 emissions produced by the integrated steel manufacturing route [20].

The furnace is charged with iron ore sinters or briquettes, coke and flux bearing materials to the top of the furnace. As the coke combusts there is a release of carbon monoxide, this in turn reduces the iron oxide in the ore to metallic iron. The molten metal drips through the porous coke and is collected in the hearth, ready for tapping as shown in Figure 2-3 [22].
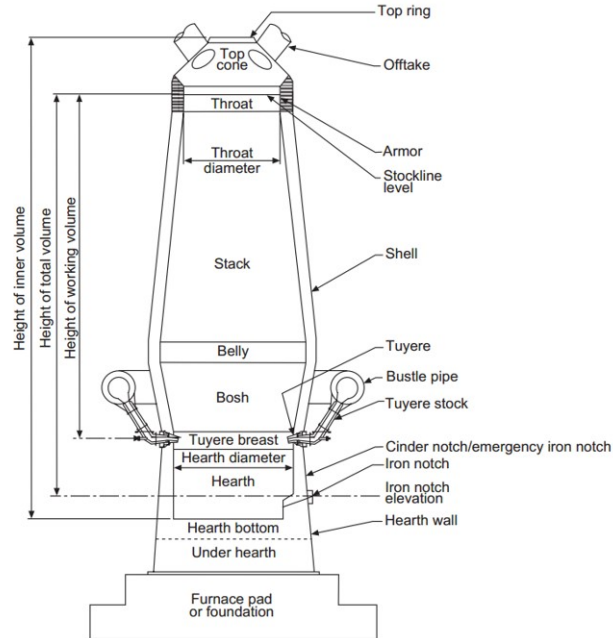
Figure 2-3: A schematic of a cross section of a BF with labelled components. [22]

Coke goes through several reactions in the BF. The first of which is combustion which creates the heat for the melting of iron as well as promoting the endothermic reduction for iron oxide. The combustion produces carbon monoxide either directly (see reaction 2.2) or at high temperatures (above 900-1000 °C) by means of the Boudouard reaction (see reaction 2.3) [23].

$$2C + O_2 \rightarrow 2CO \tag{2.2}$$

$$C + O_2 \rightarrow CO_2, \tag{2.3a}$$

$$CO_2 + C \rightarrow 2CO \tag{2.3b}$$
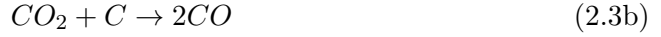
The reduction of iron ore has multiple oxidation states that are achieved through the BF. The process of reduction is a two or three step reaction; the given pathway is temperature dependant. For temperatures higher than 570 °C, hematite (Fe_2O_3) is reduced to magnetite (Fe_3O_4), then into wüstite (FeO) and finally into metallic iron. However, below 570 °C the reaction skips the creation of wüstite, as at this temperature wüstite is not thermodynamically stable. The reactions of the reductions are given in equations 2.4 - 2.6.

$$3Fe_2O_3 + CO \rightarrow 2Fe_3O_4 + CO_2 \tag{2.4}$$

$$Fe_3O_4 + CO \rightarrow 3FeO + CO_2 \tag{2.5}$$

$$FeO + CO \rightarrow Fe + CO_2 \tag{2.6}$$
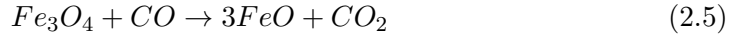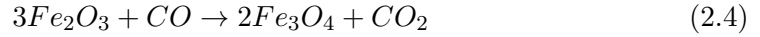
2.1.3 Basic Oxygen Steelmaking

Basic oxygen Steelmaking (BOS) is the process of taking the pig iron from the BF and converting it to steel. The technology is referred to as basic due to the fluxes, which are chemically basic. These fluxes are used to remove the impurities from the pig iron, and to protect the lining of the converter. The most common fluxes used in this step are burnt lime (CaO) and dolomite ($CaMg(CO_3)_2$). These compounds are basic and are used to offer a physical and chemical pathway for the removal of acidic oxides such as SiO_2, Al_2O_3 and P_2O_5 from the hot metal, which are produced due to oxygen reacting with residual elements. The oxygen is used to remove carbon from the pig iron to create a low-carbon steel, which encompasses the most common commercial steel grades, also creating a low alloyed product for further chemical engineering for specialised applications. The main process with BOS is a basic oxygen furnace (BOF), this is an open top vessel with a retractable lance that blows high purity oxygen at 100-150 psi to the surface of the molten pig

iron. A schematic of a BOF is given in Fig 2-4. [24]
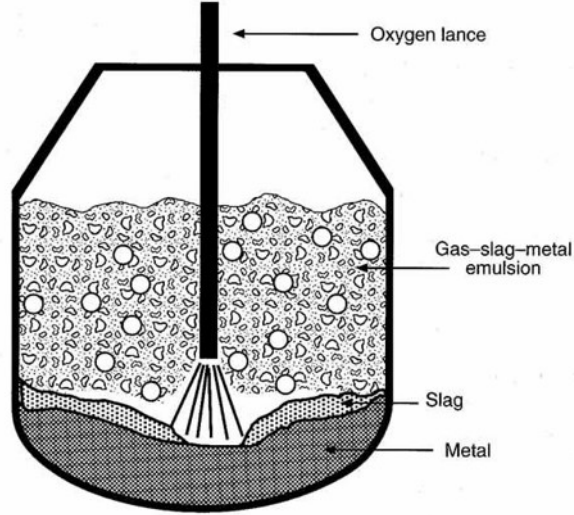
Figure 2-4: Schematic of a cross section of a basic oxygen furnace with notation of material layers. [24]

The CO_2 emission is quite substantial as the reaction of carbon and oxygen creates CO and CO_2 as seen in equations 2.3. The BOF method equates to 11 % of CO_2 production for the entire process, this is second only to the BF itself (approximately 7 times more) [20].

2.2   Alternative Ironmaking Technology

2.2.1   COREX®

COREX® is a smelting-reduction process that is industrially and commercially viable with plants in operation around the world. These include two in China (Bayi Steel and Baosteel), two in India (Essar steel and Jindal South west (JSW)) and one in South Africa (Arcelor Mittal) [25]. This process works with two separate reactors of the reduction shaft and the melter-gasifier.

The reduction shaft sits above the melter and an iron ore mix of 30-80 % lumpy ore and 70-20 % pellets are charged into the shaft with some coals to avoid clumping [26]. A reduction gas is introduced at 850 °C at 3 bars of pressure, which reduces the iron containing material to 95 % metallisation. This process is called direct reduction ironmaking (DRI). The product is then discharged into the melter-gasifier which continues the process. [27]

11

The melter-gasifier, where the product of the reduction shaft is charged can be split into three clear sections. The freeboard, fluidised bed and the moving bed all of which is presented in Figure 2-5 [28]. The free board is a large dome structure with temperatures up to 1000-1100 °C in this section there are several tuyeres for introducing material into the furnace including coal, coke, and iron ore to form the DRI. There are also exhaust for the gases that are used in the DRI. The fluidised bed is rested on a layer of liquid slag is where the coal from the freeboard is charred. On the side are raceways in which oxygen is blown in and reacts with the coal following equation (2.2 and 2.3) making CO. The moving bed acts like a hearth in a BF where there is a layer of slag and the hot metal [29].
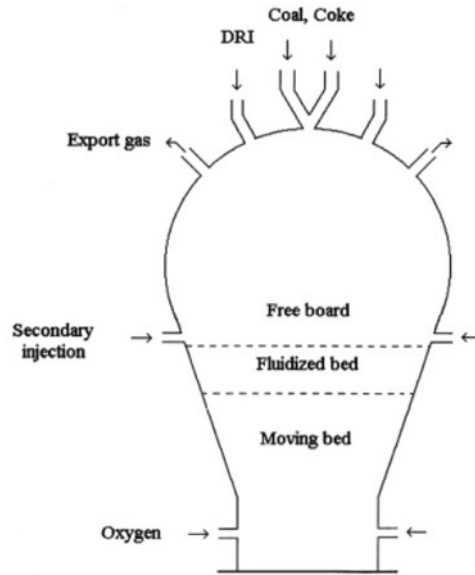
Figure 2-5: Schematic of the COREX® melter-gasifier with labelled sections of the smelter. [29]

The process benefits from lack of necessity of coke and therefore the use coking oven compared to BF ironmaking. A fuel saving of 18 % aided by the reduction of the fuel rate form the re-circulation of the top gas back into the shaft furnace and an oxygen reduction of 13 %. It also reduces emissions of gases such as CO_2 (20 % per tonne), NOx (30 % per tonne), significantly lower SOx and zero volatile organic compound (VOC) emissions. The slag in the process is also reduced by 18 % that has been industrially demonstrated in India. The process also offers lower investment and operational cost to the BF. There are drawbacks of the process that can affect its operation as a commercial process. The process cannot use 100 %

iron ore fines and therefore must be combined with iron lumps affecting material synergy and there are restrictions on the amount of non-coking coal.

2.2.2   FINEX®

FINEX® is a process that was developed by Primetals and POSCO combines COREX® and FINMET technologies [30]. FINMET uses extremely dry iron ore fines and of less than 12 mm in size for better flow in the process. The ore travels down four fluidised beds while a reducing atmosphere travels up through the ore with the reactors starting at 400 °C in R3 to 800 °C in R1 [31]. This is then added to a COREX® smelter that continues the DRI reaction to produce molten iron product. The FINEX® flowsheet can be found in Figure 2-6 [32].
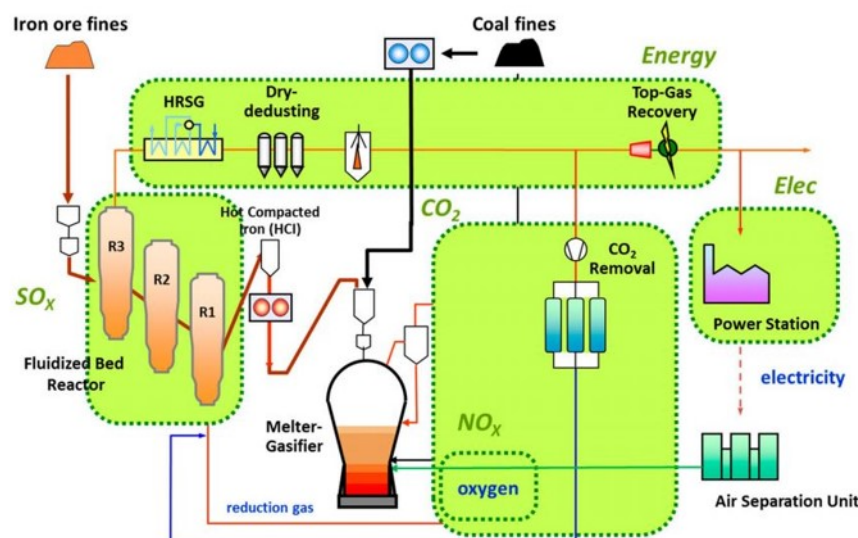
Figure 2-6: An image showing the flow of materials of the FINEX® process [32]

The FINEX®. process benefits from low cost raw materials meaning that both the investment and production cost are lower than the BF. The process also claims that a 1.5 Mtpa FINEX® process can produce hot metal more cost effective than a 3 Mtpa BF [26]. There have been two commercial plants in Pohang works the first in 2007 with a capacity of 1.5 Mtpa and the second one in 2014 with a capacity of 2.0 Mtpa [33]. The first commercial plan has been in operation since and producing 4300 tons per day with the best operational performance being 715 kg/THM for fuel [32].

2.2.3 EAF-DRI

The US produces 60 % of its steel production from scrap steel recycling and is most done by the EAF route. The recycled scrap does not require the energy needed to reduce the iron ore or make coke drastically reducing the CO_2 emissions when compared to the BF. The issue with scrap is the content of impurities such as copper and tin that can cause issues like cracking during casting.

The addition of DRI into the process, allows these materials in the scrap to be lower thus increasing the quality of the steel. Secondly, the process is less reliant on scrap and the cost it incurs from the scrap market price. Finally, the DRI pellets can be produced on site of a steel plant off gases from other processes cutting the cost of transport [34].

2.3 HIsarna Technology

HIsarna is an emerging technology for alternative iron making. The technology came together after the formation of ULCOS programme; a consortium of 48 European companies that have committed to cooperative research and development to reduce CO_2 emissions from the steelmaking process [35]. The HIsarna process is a strategic merger between two technologies: smelt cyclone technology owned by Tata steel and HIsmelt owned by Rio Tinto [36]. A pilot plant has been built up in Tata Steel IJmuiden site, Netherlands, with a capacity of 60,000 t/a.

The IJumiden pilot plant has a SRV with a diameter of 2.5 m and a CCF that was used previously in the original tests from the mid 1990's. The output is 8 t/h of hot metal from a feed of 13-14 t/h of ore. As seen in Figure 2-7, HIsarna is arranged with these two innovations working in tandem and is emerging as an attractive option for future ironmaking with the success of initial campaigns. The HIsarna pilot plant has successfully gone through five campaigns since 2011. The proved advantages of the HIsarna process are:

1. It is flexible in raw materials and energy sources. It uses thermal coals (instead of metallurgical coal or coke) and potentially new energy sources. It can use low quality iron ore feed materials, complex iron ores, wastes and scraps.

2. There is no need of coke making and sintering as it uses fines of coal, iron ore and fluxing agents. This can substantially reduce the CO_2 emissions.

3. (3) Reduction in over 25 % CO_2 emissions was achieved in the first four campaigns, and 50 % CO_2 emissions reduction was achieved in the 5th campaign without CCS, >80 % with CCS.

4. High concentration CO_2 in the off-gas as toxic CO is post combusted in the CCF. The high concentration makes it easier for capture for geological storage [36].

5. The hot metal from HIsarna was found to have a carbon content of 4.0 % [36]. Which is around the same levels of carbon (4.5 %) [37] found in the BF hot metal.
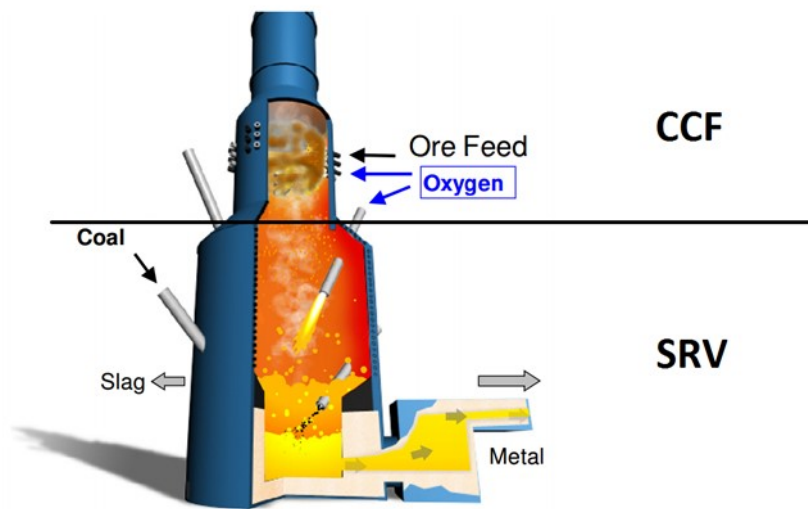
Figure 2-7: The HIsarna smelting vessel with labelled sections [36].

2.3.1 Cyclone Converter Furnace (CCF)

The CCF is a direct smelting technique originated from the CBF (Converter Blast Furnace), which was created by three steel businesses in 1986: Hoogovens, British Steel Technical and Ilva. The CBF uses lumpy ore, which is highly pre-reduced in a shaft with final reduction and melting happening in an iron bath with vaporised fine coal to aid reduction. This made the coke making process redundant. However, there were problems with ore agglomeration. Due to the agglomeration the CBF was modified to the CCF, which incorporated a melting cyclone to aid in pre-reduction and ore melting. A small CCF plant was built in Taranto, Italy in 1989 [38].

The CCF implements a BOF type converter on which, a cyclone is mounted on top of the BOF vessel. Coal and oxygen are supplied continuously to the molten bath, ensuring constant carbon content in the bath and the temperature of the bath by controlled combustion. Fine iron ore and coal are added tangentially with lances using a carrier gas. The combustion results in hot gases which rises into the

cyclone; where they mix with injected reactants, melting and pre-reducing the iron ore. The molten pre-reduced iron ore collects onto the water-cooled walls and drips into the molten bath below for final reduction. The waste gases leave the cyclone at temperatures of 1600 °C-2000 °C. The expelled gases power a steam turbine and are recovered and processed for reuse in the CCF or captured for other uses [39]. Figure 2-8 shows a schematic of a CCF including a flow of waste gases.
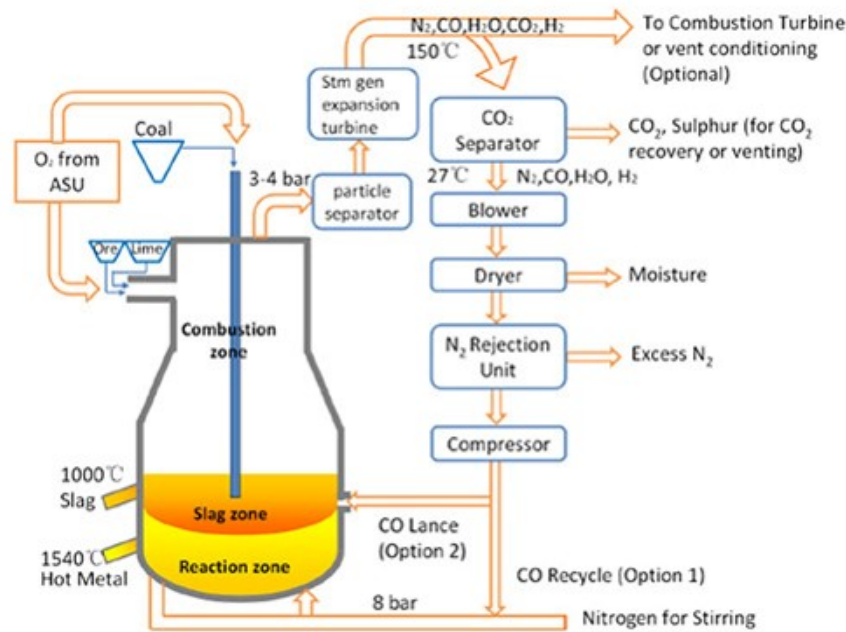
Figure 2-8: A schematic of a CCF with labelled sections of the furnace and flow diagram of reactants, products and waste. [6]

The CCF had potential to reduce CO_2 emissions by two methods: firstly, the cyclone allows the iron ore to be pre-reduced and melted in the exhaust gases from the bath, meaning less thermal energy is needed for final reduction and thus less coal input would be required. Secondly, the exhaust gases used in the CCF are post combusted therefore the gas released is predominately CO_2 instead of a mix between CO_2 and CO. This means the gas is easier to store as the gas does not need to be separated when being stored.

2.3.2   HIsmelt Plant

The HIsmelt process was started in the 1980's by Rio Tinto Limited and a small-scale plant was built at Maxhutte Works in Germany. The plant had campaigns run with a 60 metric tonnes converter and designed around an enclosed horizontal vessel

to overcome process containment issues [5]. After these successful campaigns the HIsmelt Research and Development Facilities (HRDF) was established in Kwinana, Australia. A plant with a capacity of 100,000 t/a was constructed which was a direct scale up from the small scale plant in Germany [40]. The HRDF offered valuable operational data, which was instrumental in HIsmelt being commercialised and the first production facility was also located in Kwinana. It has a 6 m wall SRV and designed to produce at 100 tonnes per hour of hot metal (800,000 t/a). [5] See Figure 2-9 and Figure 2-10 for a schematic of HIsmelt.
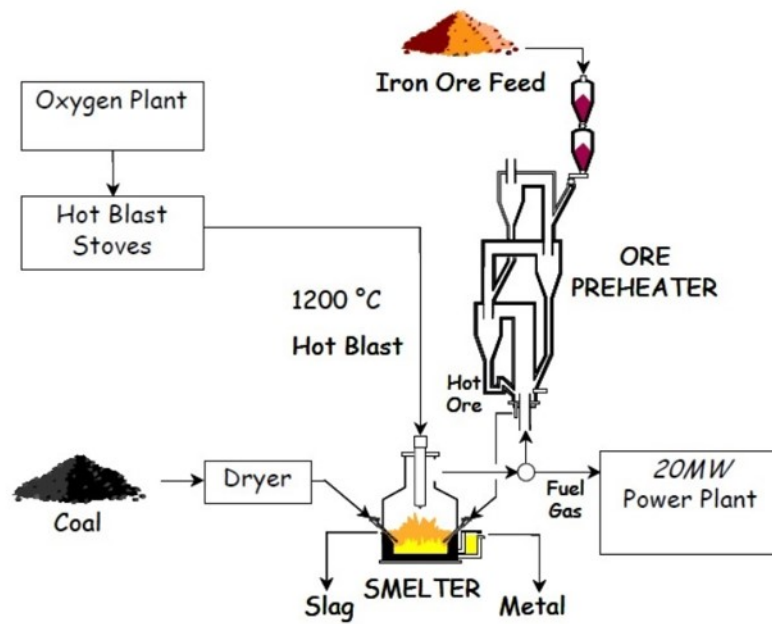
Figure 2-9: Flow chart of the material and process of the HIsmelt Process. [5]

HOT AIR BLAST
1200 C
(OXYGEN ENRICHED)

OFFGAS

WATER-COOLED
PANELS IN TOPSPACE

COAL & ORE   COAL & ORE

METAL

SLAG

REFRACTORY LINED HEARTH
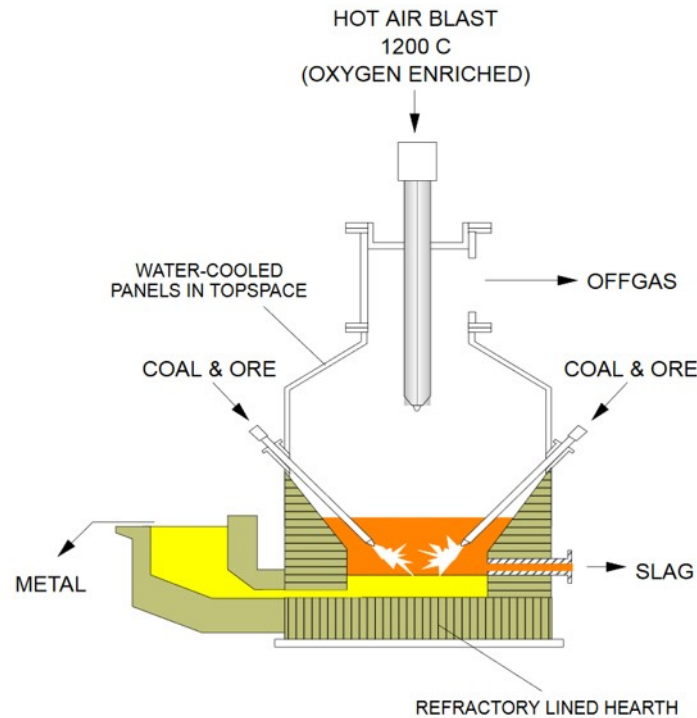
Figure 2-10: Labelled schematic of the SRV in the HIsmelt. [5]

The Kwinana HIsmelt was commissioned in April 2005 and operated at 80 tonnes per hour until December 2008 when it was forced to shut down due to financial issues within the company. [41] To continue the development of the method, Rio Tinto signed a MoU with JSPL of India [40]. The plant was then moved from Kwinana to JSPL's existing plant in Angul, Orissa under the terms of the MoU. A portion of the Kwinana HIsmelt equipment was shipped to Molong (China) in 2013 and the Molong HIsmelt plant started operation in 2016.

HIsmelt is an air direct smelting method that is simple yet innovative in its design. It offers the benefits of using coal and iron ore without any need of preparation, such as coking before the smelter. The core of the HIsmelt is the SRV that replaces the functionality of the BF. The SRV hearth contains a molten iron bath and a slag layer above the iron bath. Iron ore fines, coals, and fluxes are added by a lance into the bath, where the iron ore fines are reduced on impact with the slag layer; more specifically the carbon dissolved in the bath, this reaction produces iron and carbon monoxide [42]. The bath also rapidly heats the coal causing the volatile matter in the material to crack resulting in the production of hydrogen. A fountain of molten material (mainly slag and hot metal) erupts into the top space

by the expulsion of gases such as, hydrogen, carbon monoxide and nitrogen (carrier gas) from the bath [42]. Hot air enriched with oxygen at 1200 °C is blasted into the top space of the SRV with a water cooled lance. The carbon monoxide and hydrogen rising from the hearth are post combusted with the oxygen from the hot air blasted releasing large amounts of energy. The heated metal and slag carried in the expulsion of gas falls back down into the hearth, then using the thermal energy from the gas combustion the iron ore is directly smelted to iron. The off gases are stored and partially cooled. The energy from the off gases is reused in HIsmelt for processes such as preheating, pre-reduction and calcination of the metallic feed and fluxes. The off gases are cleaned with a scrubber and used for fuel for the hot blast heaters or in a cogeneration plant.

2.3.3 Difference Between HIsmelt and HIsarna

The main difference between HIsmelt and HIsarna is the implementation of the CCF to the SRV of the HIsmelt. This increases the efficiency of the process as the CCF pre-reduces the iron ore before it moves into the SRV; lowering the thermal energy needed for reduction of ore to pig iron. As well as the pre-reduction the CCF also uses the gases coming from the SRV for the thermal energy for the pre-reduction in the CCF. The energy efficiency was reported to be above 97 % in HIsarna campaigns. The CO_2 concentration in the CCF off-gas is very high after pre-reduction and post-combustion, which benefit the future CCS of the off-gas. The two systems work in tandem and work together which gives HIsarna advantages over the HIsmelt.

2.3.4 HIsarna Campaigns

The HIsarna pilot plan was built in Tata Steel IJmuiden site with the aim of testing the technology for upscaling demonstration. Campaigns have been running since 2011 and plan to continue until 2018 on the pilot plant. The first three campaigns (A, B and C) are summarised below. The fifth campaign (campaign E) is completed but the information is not available yet.

2.3.4.1 Campaign A

Campaign A was the first time that the pilot plant was used and as such the main aim was to have HIsarna running to facilitate later tests with a usable procedure. The campaign was planned to have four start-ups between May and June 2011. The objectives of the Campaign were: to hot commission the pilot plant and to develop safe and reliable procedures and demonstrate safe shutdown procedure for

tapping of the slag and metal; to identify any plant modifications and to point out any investigations to tackle in Campaigns B and C.

After Campaign A, modifications were identified, and changes were made so that the next experimental campaign could provide vital data for commercialisation. A redesign and rebuild of the fore hearth overflow and product runner were required due to a breakout from the fore hearth which consequently terminated campaign A. The product runner was repositioned allowing for lancing operations in the fore hearth between runs. The new product runner was along the axis of the fore hearth connection into the SRV thus removing the possible damage to the refractories in the fore hearth side wall that caused the breakout.

Campaign A also saw issues with the process of adding ore and slag sand to the SRV because the only method was through the melting cyclone. This caused heavy accretions of unmelted materials during start up phases and when the cyclone was cool. The problem was resolved for the next campaign by installing an uncooled lance for direct addition of slag sand and ore. The accretions were a consistent problem during campaign A as further accretions of solid iron oxide were found on the lower levels of the cyclone below the ore and oxygen injectors. Another material blowing lance was added to combat this problem. The lance was water cooled and situated in the sloping roof of the SRV below the cyclone to increase gas temperature in the area via a staged combustion strategy [43].

2.3.4.2 Campaigns B and C

After Campaign A finished and all the modifications were made two more campaigns were planned. As the goal of HIsarna is to become commercially viable, these campaigns were the first look at how a scaled-up furnace should proceed.

The objectives for the new campaigns were: to investigating gas post-combustion and how various factors such as oxygen distribution over cyclone and smelter affect the reaction as well as lance positions; look at the optimisation of the productivity, by observing and eliminating any process bottlenecks; to test the refractory strategy and look at wear of the refractory in the slag regions; research different prime raw materials being used in the furnace was introduced to improve knowledge on the flexibility of materials used in the HIsarna; study the secondary raw materials such as sludges and dust that arise during the campaign run will be tested for understanding of any future issues.

Another objective for the campaigns was the introduction of a pressure-less cooling system however, this was dropped due to the need to redirect effort to complete the modifications identified in campaign A. [43]

2.3.4.3 Campaigns B

The campaign took place in Autumn 2012 and the main aims of this campaign were to confirm feasibility of the process devised in campaign A at production efficiency and over a long period of time, allowing for reliable and reproducible data. This was to be done by attempting to achieve 75 % of nameplate capacity of the plant (6 t HMm/h), which was maintained for a period of 24 hours at 90 % plant availability. Campaign B had a secondary objective to explore the operational window, by improving the process performances and improve the operating points. This was looked at over a period of 12 hours minimum at 90 % plant capacity.

The Campaign managed to produce the 2 and 3 t HM/h with a coal input of 1500 kg/t.HM. This was below the aimed rate however, issues with slag foaming caused problem during the testing. The plant operated safely throughout the campaign including times of difficult start-ups and the slag foaming events. This showed that the robust safe operating procedure devised in campaign A was successfully followed [43].

2.3.4.4 Campaigns C

Campaign C was designed with following the collective feedback from the previous campaigns, in spring 2013 the campaign began. The main objectives of this campaign were to extend the duration and availability at 75 % of the nameplate capacity of the plant (6 t HM/h) and to increase the production rate and maintain stable conditions for more than 12 hours. This was the first campaign where a range of raw materials were tested including two high grade hematite ores (with different particle size and distribution.), a low-grade ironstone ore, a semi-anthracic coal (used in campaigns A and B) and a mid-volatile coal. The campaign also wanted to test other secondary raw materials specifically, a BOF sludge from IJmuiden as a lime substitute.

The BOF sludge was unsuccessful in campaign C during a test run because of inadequate control of feed rate. The addition of this sludge would have been interesting to see the interaction with the iron ore and the pre-reduced iron ore.

Cyclone pre-reduction degree varied from 12.6 % to 26.9 %; this is in line with previous results from the melting cyclone. This area may benefit from further study as to improve these rates the thermal energy required will be reduced allowing for greater efficiency [43].

2.4   Fluxing

Flux from a metallurgical standing is a chemical cleaning agent or purifying agent, which are used in both extraction and joining of metals. The flux material that is added during smelting is bound to unwanted minerals to help remove them, forming slags [8]. As this is an important part of the iron making and steelmaking processes, it has seen a large level of interest from the research community. Specifically, on the ability of dissolution of fluxes in slag, research has focused on the dissolution of CaO. As this is an effective flux and already implemented in steelmaking processes due to its price and availability. Thus, experimentation on finding the kinetics of the dissolution of fluxes in slags is a specific area of interest.

Mstsushima et al [44] studied the kinetics of lime dissolution in slag by using a rotating CaO cylinder in slag. They tested various aspects effecting the rate of dissolution including the effect of FeO content in slag, rotation speed and temperature. They concluded that the mass transfer was the rate-determining step. Natalie and Evans [45] then investigated the effect of lime properties on the rate of dissolution in a $CaO - SiO_2 - FeO$ slag, this was done using a rotating disk apparatus. They reported that the porosity of the lime played an important role in the dissolution of the CaO. These early experiments were done in small laboratory tests under static conditions and observing the slag penetration into the rotating lime rod via post-mortem analysis.

However, these conditions are not close to those found in the actual BOS process. Li et al [46] investigated the dissolution of lime in BOS-type slags from three different sized furnaces: a 40 Kg induction furnace, a 6 tonnes pilot plant converter and a 320 tonnes industrial converter. By observing the lime-slag interface the behaviour of lime in the BOS-type slag samples from the three furnaces, the results from each furnace differed. For the induction furnace across the slag-lime interface there was two layers, a dense and continuous di-calcium silicate-calcium phosphate ($C_2S - C_3P$) solid solution layer next to bulk slag and a FeO/MnO rich layer next to the lime. However, in the 6 tonne pilot plant and the 320 tonne industrial converter no continuous layer of $C_2S - C_3P$ was observed. This was due to the dynamic conditions in the furnaces where the boundary layer surrounding the lime particle that had the possibility of forming the di-calcium silicate (C_2S) layer was moved away.

The fluxing practice used in HIsarna campaigns B and C was to inject lime into the slag layer in the SRV vessel [43]. This is the standard process in the HIsmelt that the HIsarna inherited from. However, the HIsarna technology could introduce

flux in the CCF, which not only uses the heat in the CCF to calcinate the flux but also brings forward the reactions between the fluxing agents and iron ore from SRV to CCF. Introducing flux in the CCF will potentially result in the increased efficiency in energy utilisation and production. Because of the innovative nature, there has been no research on how a flux will interact with (pre-reduced) iron ore in the CCF.

The reports related to lime dissolution in slags offer good insights to the current research on the interaction between fluxing agent and (pre-reduced) iron ore in the CCF. The fluxing agents (e.g., lime, limestone, recycled BOF slag) will be injected through lances into the CCF along with iron ore fines. The dynamic situation surrounding the injected powders of fluxing agent and iron ore caused by the carrier gas will have high mass transfer, which potentially benefit the dissolution of the flux or the interaction of flux with iron ore. The investigation by Natalie and Evans [45] gives information on the porosity of the lime aids in dissolution, effecting the current studies of using different forms of CaO including lime, limestone, BOF slag and dolomite. Each of these have different properties that may affect the dissolution and consequently the pre-reduction of iron ore. From the test done by Li et al [46] it is proposed that fast moving conditions such as in the CCF may affect how the lime and other CaO containing material react with iron ore under these conditions.

2.5 Calcination

Limestone is a material that widely used in industrial processes usually as an alkali due to its large availability. However, for the full use of the material the limestone ($CaCO_3$) must decompose to lime (CaO) this process is commonly known as calcination. Calcination can be expressed with the equation 2.7.

$$CaCO_3 + heat \rightleftharpoons CaO + CO_2 \qquad (2.7)$$
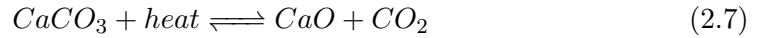
The reaction kinetics were studied by observing limestone particle (25 mm) decomposing in a lime kiln. This study can be used to describe the decomposition of limestone as well as dolomite and magnesian/dolomitic limestones. The particle is heated to 800 °C and at this temperature; the pressure of the CO_2 produced by the decomposition equals the partial pressure of CO_2 in the kiln gases. The temperature of the limestone begins to rise allowing the surface layer to decompose, when the temperature rises to 900 °C this layer of lime will be 0.5 mm thick. This corresponds to around 5 % by the weight of quicklime for this size of particle. As the particle increases past 900 °C the partial pressure and exceeds 1 atm; the dissociation can

proceed deeper into the particle and the lime produced begins to sinter. However, the lime sinters if the calcium carbonate dissociate before leaving the calcination zone, this is very limited during the dissociation deep into the particle but can be disregarded in most systems. Particles of lime are left and can have some residual limestone and cooled. [47]

2.5.1 Ca Looping a carbon capture system

Calcium looping (CaL) is a carbon capture system that utilises the calcination reaction to react with combusted CO_2 with CaO to form $CaCO_3$ in a carbonator. Then the $CaCO_3$ can then be heated to remove the cleaned CO_2 in a calciner to form CaO that can be recycled in the process. The process is designed to remove CO_2 from the off gas of industrial industries to protect the environment and purify the CO_2 from off gases from other gases for containment or even resale. The process was developed by Shimizu et at in 1999 and through in lab scale test the process and sorbent behaviour was studied with the main method being TGA [48]. This allowed the process to be developed further with bigger scale lab systems. A schematic of the process can be seen in Figure 2-11. [49]
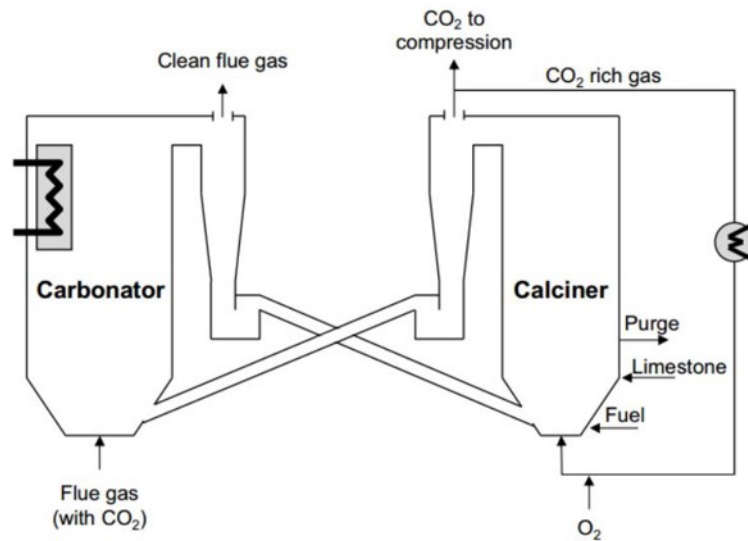
Figure 2-11: A simple schematic of a CaL system with flow of materials through the process [49]

The work from Shimizu et al 1999, CaL was studied in further and between 2005 and 2010 with several lab scale plants. The first of these were 30 kWth system in Oviedo, Spain at the carbon science and technology institute (INCAR) [50],

75 kWth in Ottawa, Canada at Canada centre of mineral and energy technology (CANMET) [51] and a 10 kWth at the university of Stuttgart [52]. Further plants were opened later however the results from the initial lab scale plants showed the process as a feasible method of carbon capture systems. With the INCAR process showing a capacity of 90 % while CAMET and the Stuttgart facility reported 94 % and 93 % respectively.

These lab scale tests increased the interest in and the further need to test the process at a greater scale and under conditions that are more realistic. Three CaL plants were built in Europe and a fourth in Taiwan. The three European ones include a 1.7 MW_{th} at La Pereda by a consortium in Spain in 2011 [52], a 1 MW_{th} at TU Darmstrat, Germany in 2012 [53] and a 200 kW_{th} at the university of Stuttgart, Germany in 2010 [54]. One more pilot plant was set up outside of Europe and is a 1.9 MW_{th} plant at Industrial Technology Research Institute (ITRI) in Taiwan [55]. The European plants and Taiwan plant differ as the European plant are used as a CCS for cleaning power plant off gas while the Taiwan plant is used in CCS with cement applications.

2.5.1.1 Advantages

The main advantage of the process when compared to amine scrubbing include its overall efficacy, the materials needed for the process and its ease of upgrading current CO_2 sources with the system.

The efficiency of the CaL has been shown to capture 89.4 % of overall CO_2 while this is lower than an amine scrubber that had a CO_2 capture of 90 %. However, the plant overall had a lower net output of 700 MW while with the amine scrubber increased to 900 MW. Hence the efficacy ratings were lower for the CaL when compared to amine with a penalty of 5-8 % and 8-12.5 % respectively [56]. This shows that even though CaL has 0.6 % less CO_2 capture the process over all is more energy efficient.

The material needed for CaL is limestone, which is a natural product that is already readily available to worldwide due to its use in multiple industries such as Ironmaking and cement making. It is non hazardous meaning it can be disposed of easily and can even be used in the cement industry in its manufacturing. The availability of the material also leads it to being cheap when compared to the chemicals needed for amine scrubbers.

The ability to implement it to existing power stations and other CO_2 producing industries has been shown as the process is like current large scale circulating fluidised bed combustors. While amine scrubbers require more bespoke solvent

scrubbers. This means that CaL should be more attractive to industries as the literature on these system using limestone is large allowing greater expertise on the systems [56].

2.5.1.2 Drawbacks

The pilot plants have been promising as an alternative to amine scrubbing. However, the main issues facing the process are sorbent degradation and other technical implications.

Sorbent degradation is used to describe the reduction in activity of the sorbent used in the CaL process and occurs in three ways. The first of these is called attrition which is where the natural brittle properties of lime causes the particles to break apart on collision in the fluidised bed this decreases the pore size and increases the sintering of the particles [57]. The second and third are caused by the sulphation of the lime and limestone this is called indirect and direct sulphation the equations for each is presented in 2.8 and 2.9 respectively [58]. These reactions are due to the presence of SO_2 in off gases and means the sorbent only lasts several cycles before needing to be replaced.

$$CaO + SO_2 + \frac{1}{2}O_2 \rightarrow CaSO_4 \tag{2.8}$$

$$CaCO_3 + SO_2 + \frac{1}{2}O_2 \rightarrow CaSO_4 + CO_2 \tag{2.9}$$
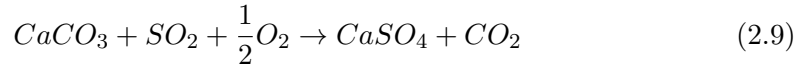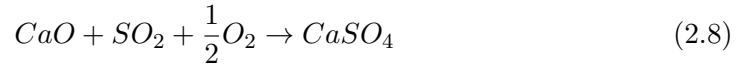
The technical implication is twofold: the first is the closure of the pores and the second is sintering. Closure of the pores inhibits the absorption of CO_2 and its ability to reach the reactive surface in the particle [59]. This is due to the surface of the material becoming smoother over a series of calcinations and carbonations. The sintering is aided by the attrition as the CaO particles are smaller and thus removing void space which would allow for the adsorption of CO_2 [58]. A good visualisation of the structure changes is presented in Figure 2-12 [56].
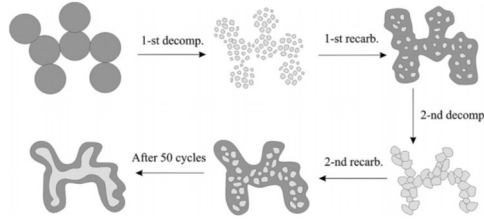
Figure 2-12: Schematic representation of the CaO sorbent over cycles in the CaL with CaO represented in light grey and $CaCO_3$ in dark grey [56]

2.5.1.3 How the iron industry can benefit

The iron industry is primed for the introduction of such systems as it is a high CO_2 industry that has access to limestone on most integrated steel plants. The high temperature of the process can also be utilised to heat the CaL process to the temperatures needed, thus saving more energy in heating the process. These plants also have infrastructure such as fluidised beds which are already implemented for the storage of material for the plant.

Another benefit is that research is being carried out on the possibility of using BF slag as a sorbent in the material [60]. This is beneficial to the industry to make judgments on if the material in the CO2 scrubbing process can be used as a flux once it has deteriorate or sell it onto cement companies. Increasing the circular economy of the materials used on plant.

The HIsarna process has the potential of using this process as a CCS to reach the full potential to reduce CO_2 emissions. The high purity of the CO_2 released from the process could be used with little prior processing to scrub impurities from the off gas. There is also possibility of that the degradation of the sorbent may be utilised as a fluxing agent in the process as this should not affect the chemical properties however the structure and size may reduce the reactivity of the material and will need further research. The research that has been done on CaL such as the work on the sorbent degradation and the kinetics of calcination of limestone can also benefit by to maximise the use of these materials at high temperature. This will include the structure of the material and how it changes the reactivity, how the material will react under high CO_2 atmosphere like those found in the CCF of HIsarna and the kinetics of the limestone as it goes through calcination with its metastable state. All of these can be used to discuss reaction with other substances in high temperature environment.

2.6 Phase diagram for $CaO - Fe_tO$ system
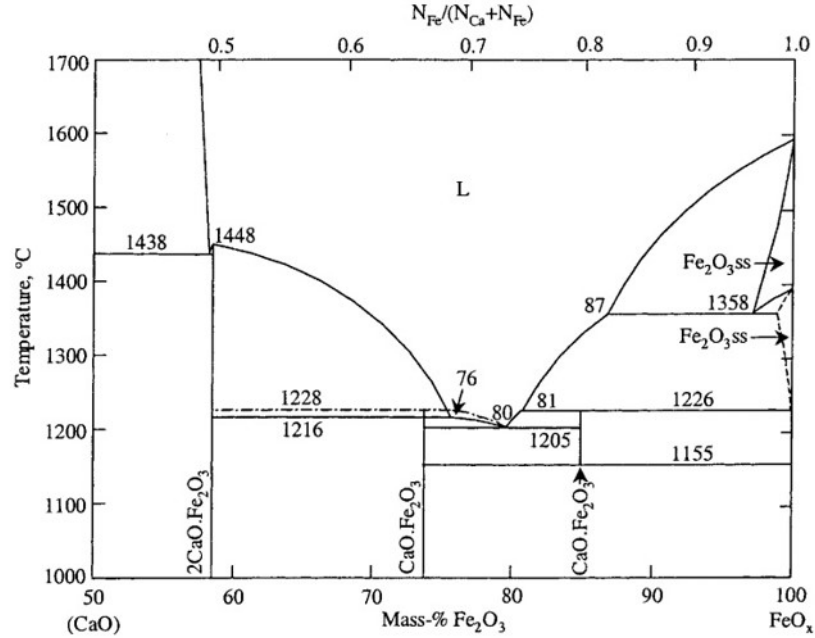
Figure 2-13: A phase diagram between CaO and Fe_2O_3 showing how the amount of CaO effects the phase transitions of Fe_2O_3 [61]

This phase diagram shows that introducing CaO to Fe_2O_3 reduces the temperature from around 1600 °C to melt pure Fe_2O_3 to 1205 °C of eutectic point. This is due to the fluxing effect of CaO on Fe_2O_3 [61]. The $CaO - Fe_2O_3$ interaction was studied in great depth by Phillips and Muan [62] with two aims. The first was to investigate the $CaO - FeO - Fe_2O_3$ system to build upon the literature of the system and fill any information missed in the previously. The first part of experiment gave similar phase diagrams to the one seen in the literature. The second aim was to study the equilibrium of the same system under two different constant O_2 pressures (0.21 atm and 1 atm). The second part of experiment did show slight changes. The first observation was that iron oxide melts at 1594 °C in air while at 1583 °C in 1 atm of O_2. However, when CaO is added to make around a 20 wt. % composition the temperatures did decrease for both the atmosphere in air (the melting temperature dropped from 1216 °C to 1205 °C) and in the higher level of O_2 atmosphere (the melting temperature dropped from 1218 °C to 1205 °C). The atmosphere change also affects the temperature of the decomposition of hematite to magnetite. In air the temperature of decomposition dropped from 1390 °C to a minimum of 1358 °C and in the 1 atm of O_2 the required temperature dropped from 1455 °C to 1430 °C

28

when CaO was added to both samples.

These tests at different atmosphere suggests that there is an effect of the change in O_2 pressure in the system on the phase transitions. It will be reducing atmosphere in the CCF of the HIsarna technology. Hence a need for investigation on how the atmosphere in CCF affects the dissolution of the CaO into the iron ore; this may affect the barrier for pre-reduction of haematite.

2.7 Shrinking Sphere Model

In the literature the rate of the reduction of iron ore is studied by using a single particle suspended in a flowing-gas stream with a known composition and constant temperature. This allows for continuous measurement of weight loss which allows inference of the reduction rate for kinetic study. [63] McKewan studied the magnetite (Fe_3O_4) reduction by hydrogen at temperatures below 570 °C. He investigated a single interface within an unreacted shrinking reduction model for iron ore experimentally. The unreacted shrinking core model is presented in Figure 2-14.
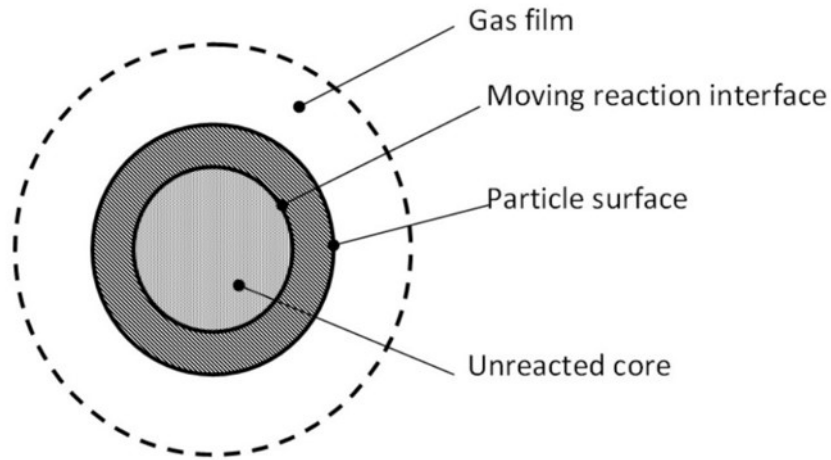
Figure 2-14: Schematic diagram of shrinking sphere model. In which the particle is mid reaction with a unreacted core and a moving reaction interface [64].

The model shows three phases: the gaseous phase, the product layer, and the unreacted core. For iron ore, the removal of oxygen from the unreacted core creates an interface between the product phase and the unreacted core; this is where the reaction takes place. The loss of oxygen can be measured by the change of weight during the reaction; the reaction process goes through the following steps:

1. The transport of gas reactants (CO/H_2) from bulk gas to the exterior surface of the iron ore particle at the gas solid boundary.

2. The diffusion of gaseous reactant through the product layer to the reactant surface to continue the reduction reaction.

3. Chemical reduction of the iron oxide by the reactant gas CO or H_2.

4. The product gases (CO_2 and H_2O) move outwards through the product layer.

5. The gas products then move from the exterior of the product surface and travels back into the bulk gas through the past.

Using the shrinking core model, a rate equation can be determined for the reduction of a particle. This is done by studying each of the steps outlined above and designing an equation around the steps.

This kinetic theory may have relevance in the study of the dissolution of CaO into the iron ore collided in the CCF of the HIsarna. The iron ore is not suspended in the gas but moving through the furnace at high velocity so this may affect the rate of reaction due to higher mass transfer. Not much study has been done on how a flux will affect the kinetics of the reduction of iron oxide, for example, lowering melting point may change the diffusion through the unreacted phase.

2.8 Literature Review Findings

This review outlines the challenges that the integrated steelmaking process is facing. The most pressing challenges are the amount of CO_2 emissions generated and lack of flexibility in energy and materials resources. The emissions of the integrated route are unsustainable for the industry as governments and the populous put more pressure on high CO_2 producing industries. The need for greener and more sustainable methods will alleviate this pressure. The flexibility of resources has arisen through new competitive producers becoming strong contenders in the market this has caused material process to rise. Along with the amounts of steel required by consumers increasing means resources are in more demand.

Consequently, alternative iron making technologies are needed as the current integrated route is struggling with these issues. HIsarna is one of these alternative technologies being developed to appease these challenges. Due to its potential to cut up to 40 % of CO_2 (80 % with CCS) and its flexibility in resources (energy and raw materials) will allow for use of the cheapest available materials without

any negative effects on productivity. The early tests on the pilot plant have shown promise to reach its potential.

However, due to the innovative nature of the HIsarna technology and being in early stage of its development there is a severe lack of fundamental knowledge to underpin development. Though there has been some research done on the reduction behaviour of the iron ore in HIsarna, nothing has been done on the interactions of fluxing agent and iron ore in the CCF.

Although the topic of fluxing has been highly researched in metallurgy the focus was usually on the dissolution of fluxes into steelmaking slag. There has been no research on the interactions between (pre-reduced) iron ore and CaO-based fluxes under HIsarna's CCF conditions. The study in this area will reveal the reaction mechanisms between flux and (pre-reduced) iron ore in the CCF with a unique atmosphere of high temperature, reducing atmosphere and high mass transfer.

Chapter 3

Approaching the Research

This chapter contains the hypothesis that drove the research for this thesis. Formed through the gaps found from the literature review and the industrial problems facing the development of the HIsarna process. The hypotheses are listed below along with a plan to explore and test the questions that arise from the statements.

3.1   Hypotheses

3.1.1   Hypothesis 1: The Structure of a HIsarna Accretion

"The structure of a HIsarna accretion gives information on position, growth and potential effect on the HIsarna process that the accretion may have."

Currently mechanism or causation of accretion growth is not clear. Advances in structural experimental methods such as XCT can reveal the internal structure of the accretion, which provides new insight into the materials agglomeration patterns.

3.1.2   Hypothesis 2: The Composition of a HIsarna Accretion

"The composition of an accretion from HIsarna has direct correlations to the agglomeration and growth of such material."

Compositions such as the levels of K_2O in a material have shown to play a role in the build-up of accretions in the BF. However, the materials found in the BF differs from those found in the HIsarna CCF. The BF stack contains layers of coal, slag, and iron ore while the CCF should only have iron ore present. As iron ore injected into the CCF is pre-reduced in CCF, which has a higher level of FeO. Does this high level of FeO or other components present in the accretion influence the formation and growth of accretion?

3.1.3 Hypothesis 3: Viscosity of an Accretion and the HIsarna Process

"A high viscosity of material within the CCF increases the agglomeration of accretions on the walls."

HIsarna's design means that molten material must move from the CCF to the SRV after the ore is pre-reduced. This with the advanced cooling system of the refractories means that a material with high viscosity will flow more slowly into the SRV. A longer time in the CCF may induce the growth and agglomeration of material in this zone.

3.1.4 Hypothesis 4: Alternative Sources of Fluxes for use in CCF

"Recycled BOF slag is an appropriate alternative to traditional fluxes (e.g., lime, limestone) for application in the CCF."

HIsarna claims to have flexibility with its use of raw materials in the process like the use of unsintered ore and non-coking coal. To extend the economic and environmental benefits that the HIsarna process can offer, the use of recycled BOF slag has potential as an alternative fluxing agent. It is viable as a fluxing agent due to its high CaO content and readily available to a modern integrated steelmaking plant with a basic oxygen furnace.

3.1.5 Hypothesis 5: Heterogeneous Iron ore particle in the HIsarna Process

"The heterogeneity of iron ore particles can have significant effects causing variable behaviour within CCF conditions."

Iron ore has multiple impurities (gangue minerals) such as other oxides like silica, alumina, and magnesia. All these complexes can alter the behaviour of the iron ore if the levels are different to those expected. With an addition of fluxing agent into the CCF, the interaction of the fluxing material with a more heterogeneous iron ore is expected to change.

3.1.6 Hypothesis 6: Particle Shape and Diffusion of CaO

"The size and shape of a particle determines the diffusion of CaO, and the time taken to melt."

CaO diffusion into a slag has been studied by combining experiment with post experiment analysis of the quenched samples. However, by developing a novel in situ visualisation method, reactions between CaO and slag can be studied at

high temperatures during the reaction. Measurement of the particle over a reaction period can give more fundamental knowledge of the interaction between fluxing materials and iron ore at high temperatures.

3.2   Hypothesis Approach

3.2.1   Hypothesis 1

Hypothesis 1 will be studied by taking an accretion sample from the HIsarna pilot plant IJmuiden (TATA Steel Europe) and examining the sample visually in two ways: First, to study the topography of the sample using microscopy (optical and SEM) to examine surface pore structure and structure of the material and how it bonds. Second, to study the internal structure with XCT technique for determining the distribution of the pores within the structure and how this effects the process.

3.2.2   Hypotheses 2 and 3

These two hypotheses will be explored by further analysing the accretion sample. This will include dissection and examination by SEM and composition gained from SEM-EDS. This will then be used as a reference to compare against iron ore compositions used to distinguish differences and investigation of literature to determine key factors in accretion growth. With the compositions' theoretical models (e.g., FactSage^{TM}) will be used to calculate how compositions effect the flow of materials in HIsarna between the CCF and SRV.

3.2.3   Hypothesis 4

To explore this hypothesis reactions of different Ca-based material with iron ore will be tested at high temperatures to understand the interactions they have with iron ore. From the in situ test in the HT-CSLM, the materials interaction can be observed visually. While further SEM analysis of quenched samples will reveal the progression of the reactions and how the reactions happen. The comparison between the materials will be used to examine the reaction between lime and CaO formed from calcination of limestone.

3.2.4   Hypothesis 5

To test this hypothesis, the composition of individual particles will be gained from SEM-EDS analysis. Then the HT-CSLM is used to determine the melting point

of fluxing material reacted with iron ore. This is compared to the theoretical calculations from FactSage$^{\text{TM}}$ for each particle to understand which impurities lower the eutectic with interaction with CaO. FactSage$^{\text{TM}}$ can also highlight which complexes are stable and how the eutectic point is reached.

3.2.5 Hypothesis 6

To test this hypothesis, the particles will be studied by using the novel method developed in this study, i.e., the combination of the HT-CSLM and sessile drop camera. This will allow the measurement of a particle (iron ore) over a set period to determine the progression of a melting particle. These measurements evaluate the diffusion of CaO into the particle (iron ore) and whether, the size of the particle is a determining factor in the rate of reaction.

Chapter 4

Experimental Material

To examine the research questions outlined by the hypothesis outlined in the previous chapter materials that would be used in the experimental research were sourced. These include lab grade reagents such as pure CaO and other chemicals needed for wet chemical analysis of samples. Industrial samples used in the HIsarna process were provided by Tata Steel Europe IJmuiden from the bulk supplies and commonly used in the HIsarna process which includes Iron ore, limestone and BOF slag. Finally, an accretion sample was taken directly from the HIsarna process after shutting down at the end of a campaign. All these samples are listed in this chapter along with the information provided with them.

4.1 Chemical reagents

All chemical reagents were sourced from reputable chemical companies and of high purity. The most significant of these is the pure CaO that had a purity of 99.99 % and was in a powder form.

4.2 Bulk samples of materials used in HIsarna

The materials in this section were provided by Tata Steel Europe IJmuiden. These were used by the HIsarna team and taken directly from the supply stores. The materials are used in the process meaning that the interactions researched in the experimentation can be expected in HIsarna. The materials are iron ore, limestone and BOF slag. The samples were dried before use and the compositions have been altered to remove H_2O in the materials. The compositions of these materials can be found in Table 4-1 and were provided by TATA steel Europe IJmuiden.

Table 4-1: Compositional information of the samples obtained by TATA steel Europe IJmuiden used in HIsarna.

Sample	$\%FeO$	$\%CaO$	$\%SiO_2$	$\%MgO$	$\%Al_2O_3$	$\%K_2O$	$\%TiO_2$	$\%MnO$	$\%CO_2$
Iron ore	66.26	1.67	6.75	0.68	1.83	0.21	0.59	0.64	1.17
Limestone	0.84	57.12	1.13	0.85	0.24	0.06	0.02	0.85	38.46
BOF slag	2.30	41.94	14.14	4.69	2.14	0.02	1.20	4.69	0.83

4.2.1 Single particle Iron ore compositions for Chapter 8

The bulk materials used in this experiment including iron ore, lime (CaO) and limestone can be found in Table 4-1. The particles used in this experiment are labelled with the compositions determined by SEM-EDS before experiment. Table 4-2 shows all iron ore particles used in experiments with CaO and Table 4-3 shows all the iron ore particles used in experiments with the limestone pellets.

Table 4-2: All particles placed on a CaO pellet with labels and their corresponding compositions.

Sample	Fe_2O_3	SiO_2	CaO	Al_2O_3	K_2O	MgO
C-1	45.8	29.4	4.6	17.2	0.3	2.8
C-2	97.4	1.1	0.3	0.9	0.1	0.3
C-3	96.3	1.3	0.4	1.7	0.2	0.2
C-4	93.4	5.2	0.1	1.0	0.1	0.2
C-5	99.2	0.2	0.1	0.5	0.0	0.1
C-6	98.0	0.6	0.2	0.8	0.1	0.2
C-7	75.8	7.6	1.8	8.3	2.4	4.1
C-8	50.8	28.4	2.1	13.1	3.7	2.0
C-9	71.3	8.7	4.4	10.6	1.3	3.7
C-10	46.0	29.4	0.1	15.0	1.2	8.3
C-11	82.0	6.0	0.1	6.6	2.6	2.7
C-12	47.8	48.4	0.4	1.9	0.6	0.9
C-13	6.8	90.7	0.5	1.3	0.4	0.3

Table 4-3: All particles placed on a limestone pellet with labels and their corresponding compositions.

Sample	Fe_2O_3	SiO_2	CaO	Al_2O_3	K_2O	MgO
L-1	97.2	0.8	0.1	1.7	0.1	0.2
L-2	96.9	1.1	0.1	1.2	0.2	0.4
L-3	75.1	7.5	6.9	6.3	1.5	2.8
L-4	97.1	0.8	0.5	1.1	0.2	0.2
L-5	95.1	1.8	0.5	1.9	0.4	0.2
L-6	76.7	9.5	0.6	8.9	0.7	3.5
L-7	92.3	2.6	0.7	3.4	0.4	0.7
L-8	48.4	20.3	16.5	2.6	0.4	11.9
L-9	50.5	31.9	2.2	12.7	1.0	1.6
L-10	23.3	31.8	3.3	32.2	7.3	2.1
L-11	23.2	74.6	0.4	1.2	0.2	0.4
L-12	28.1	70.4	0.2	0.8	0.2	0.2

4.2.2 Accretion

The accretion is a sample provided Tata Steel Europe IJmuiden, however it was taken directly from HIsarna's refractory wall. The accretion has been formed in the CCF and has caused issues such as blocking the pathways between the CCF to the SRV and potential increase of foaming. The sample did not come with any analysis and a full examination of the materials properties are found in Chapter 6. A picture of the whole sample is shown in Figure 4-1.
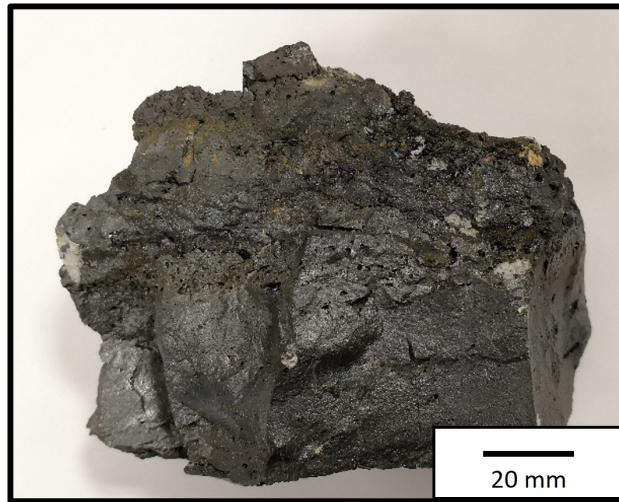
Figure 4-1: Image of the accretion sample sent from TATA Steel Europe for analysis.

Chapter 5

Experimental Equipment

5.1 Introduction

This section will list and outline the equipment used in the research in this thesis and the capabilities. A more in-depth description of the methods used with the equipment can be found in the chapter in which they are most relevant due to the novelty of some of the methods.

5.1.1 High Temperature Confocal Scanning Laser Microscope (HT-CSLM)

The HT-CSLM is an in situ observation tool consisting of a gold-coated elliptical chamber positioned bellow a UV imaging laser. The chamber can reach 1700 °C at the heating rate of up to 700 °C/min and cooling rates of up to 3000 °C/min (in the higher temperature range). Within the chamber, a halogen bulb is in one focal point, which emits IR radiation. The IR radiation is subsequently focused on to the sample which is positioned in the second focal point of the ellipse. The sample sits on an instrumented alumina stage, where an R-type thermocouple is threaded through and attached to the bottom of a platinum ring – the location the sample sits upon. The atmosphere in the chamber can be controlled through the rotary vacuum pump extraction and a high-purity gas feed. Images of the confocal are presented in Figure 5-1 [65].

   The furnace works in situ with a UV laser microscope, which avoids image interference from the IR radiation from the bulb and hot sample. The microscope sits above the chamber and can look at the sample through a quartz window at the top of the chamber. The optics within a confocal microscope are designed to give a very narrow depth field of view, allowing the equipment to image surface

roughness and texture in high detail.
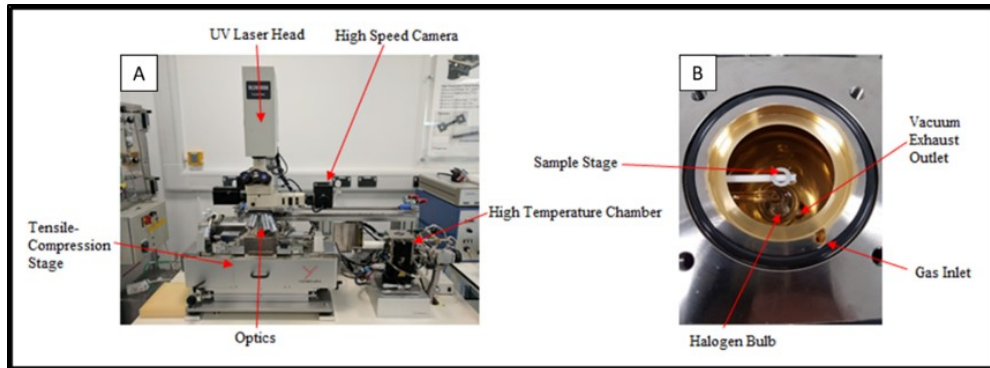
Figure 5-1: HT-CSLM a) shows an image of the entire HT-CSLM with the tensile compression stage, b) shows the interior of the high temperature chamber.

The HT-CSLM also has a rotary vacuum pump and high purity argon gas feed which has a purity of less than 2 parts per billion (confirmed using mass spectroscopy). This is achieved by passing the gas through a series of filters, getters drying chambers and a heated getter at 350 °C containing copper and magnesium turnings. The system also has potential for quenching with a helium gas connected, which increased the cooling rate to 2727 °C per minute.

5.1.1.1 Observations of Half-filled crucibles

An alumina crucible was half filled with iron ore and half filled with fluxing agent side by side (Figure 5-2). The material was compressed in the crucible so that there is a defined interface between the two materials. The sample was then heated to 1350 °C, 1400 °C and 1450 °C at 500 °C/min and held for 60s before being rapidly quenched. The experiments were recorded at 15 fps. The experiments were conducted in an air atmosphere at the appropriate partial pressure of oxygen ensuring no occurrence of passive diffusion-led reduction in the iron ore during the experiment.
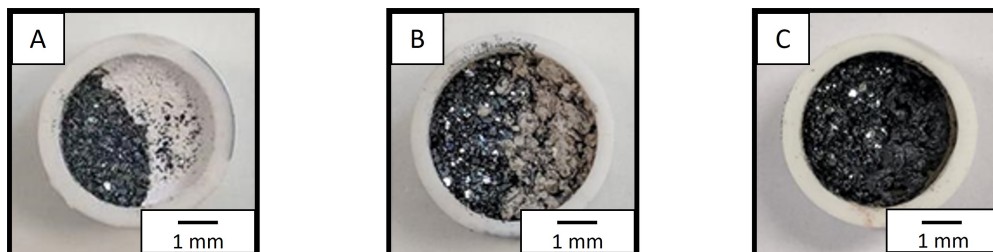
Figure 5-2: The crucible samples before use the experiments. A) Crucible of iron ore and lime. B) Crucible of iron ore and limestone. C) Crucible of iron ore and slag.

The quenched sample was mounted in epoxy resin and polished to a flat surface using SiC grinding pads incrementally increasing the grit from 800 p through to 1500 p. The sample was polished with oil-based diamond suspensions with particle sizes from 9 μm, 3 μm to 1 μm in turn. This routine was done without the use of water so as not to affect the anhydrous CaO in the samples. This polishing routine gave a clean and flat surface ready for SEM imaging and EDS elemental analysis.

5.1.1.2 Sessile drop HT-CSLM

To study a single particle reacting with fluxes in the HT-CSLM, a novel approach was used in conjunction with a sessile drop camera looking through a spare sample port to gain a new perspective of a reaction happened in the furnace. The sessile drop camera used was a FLIR® firefly MV USB 2.0 camera 1/3" with a Kowa optical 2/3" 75mm/F2.5 lens. A labelled schematic of the HT-CSLM and the sessile camera is shown in Figure 5-3. The software used with the sessile camera was FTA32 to capture the image and ImageJ was used to edit the images. Due to the open sample port for the sessile camera, this study can only be performed under an air atmosphere.
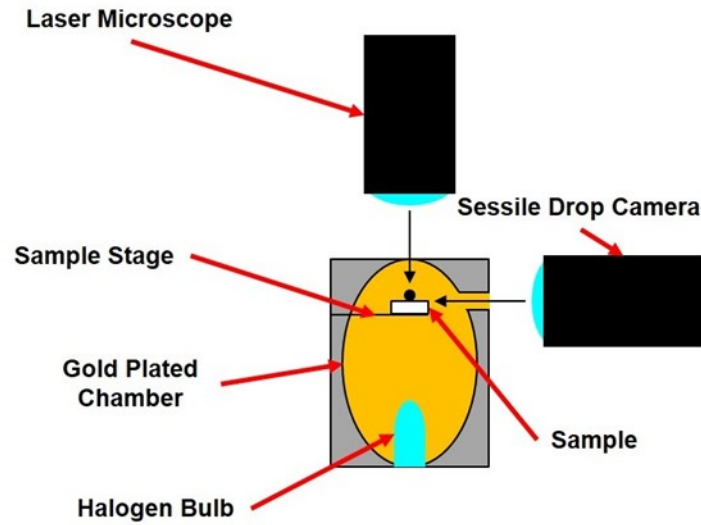
Figure 5-3: Simple labelled schematic of HT-CSLM and sessile drop camera experiment setup.

The experimental set combines deployment of a high temperature confocal scanning laser microscope (HT-CSLM) with sessile drop camera SDC in tandem. This offers a new angle to examine the particles and how they interact with the Ca-based materials, which in this experiment is lime (pure CaO) and industrial limestone form Tata Steel IJmuiden HIsarna pilot plant. In the experiment, an iron ore particle is placed on a 5 mm pellet of the Ca-based material, as schematically shown in Figure 5-4.
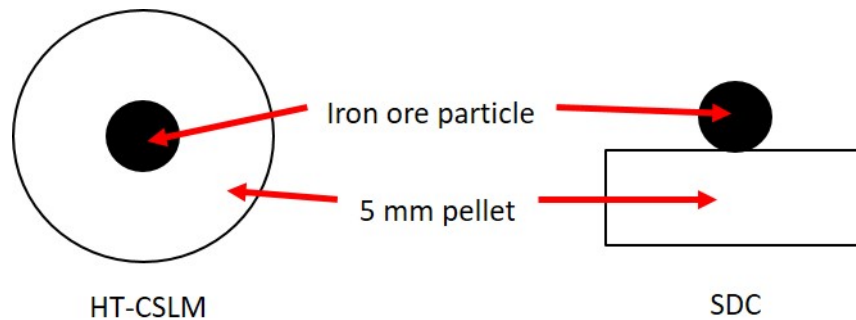
Figure 5-4: A schematic of a single particle of iron ore on a pellet of Ca based material labelled and shown from each imaging equipment.

For this experiment, the sample was heated to 1100 °C rapidly at 700 °C/min and then the rate of heating is reduced to 60 °C/min up to a maximum of 1500 °C. Once the particle starts to melt, determined by visual evidence from the microscope,

the temperature is held for at least 60 s or until molten, then the sample is cooled. An example nominal heating regime is show in Figure 5-5.
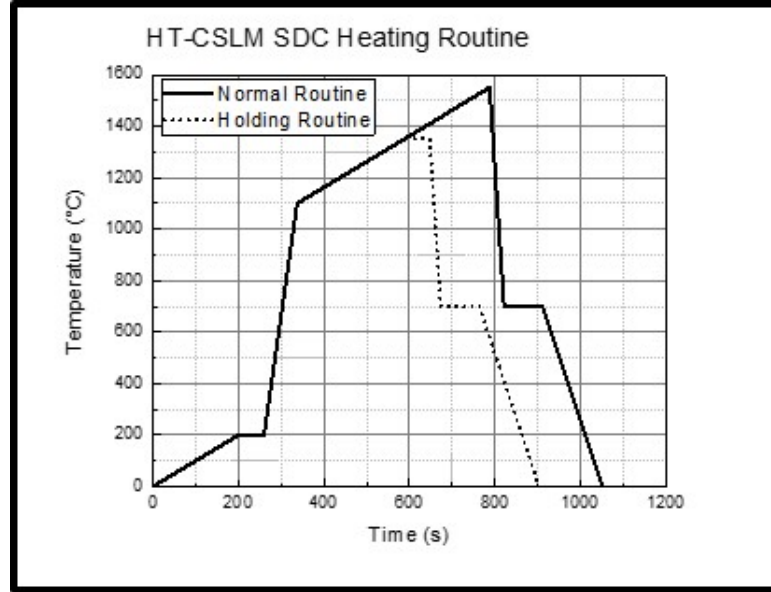
Figure 5-5: A graph to show the heating routine used in the single particle experiments. Showing the maximum heating routine ("Normal Routine") and one that has been held at 1350 °C ("Holding Routine").

The SDC is used in tandem with the HT-CSLM by utilising an open port in the HT-CSLM chamber to show the side profile of the particle melting. As this is seen in situ the melting of the particle can be viewed from different angles to further visualise the process of the interaction between the iron ore particle and the Ca-based pellet. Having the extra angle allows a better indication of the particle melting and when the particle is fully molten. A full schematic of the HT-CSLM with the implemented SDC is presented in Figure 5-3 and a photo of the experimental set up is in Figure 5-6.
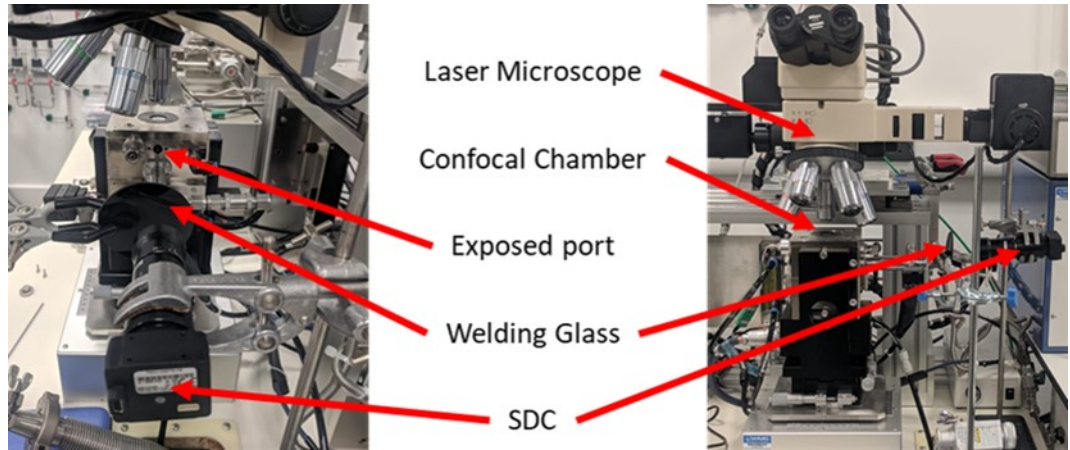
Figure 5-6: Labelled photos of the HT-CSLM and SDC experimental set up.

In both instances, the images and video were examined using image analysis software image-J [66] and measured in size for both the cameras. The cameras allowed the monitoring of a melting particle measuring its size. This is done at intervals of 10 s and changes with particle this is seen as growth in terms of the HT-CSLM and shrinkage from the SDC perspective as it interacts with the CaO material. This allows the comparison of the melting activity from particle to particle, with different compositions diverging from the same manufacture provided ore.

5.1.2 Image analysis methods

All images gained from the HT-CSLM and SDC were analysed using the imaging software ImageJ. The program uses the scale bars imbedded in the image to set a scale per pixel of the image which is then used to measure particles length, height, and area. For both the HT-CSLM and SDC a schematic of the measurements can be seen in 5-7.
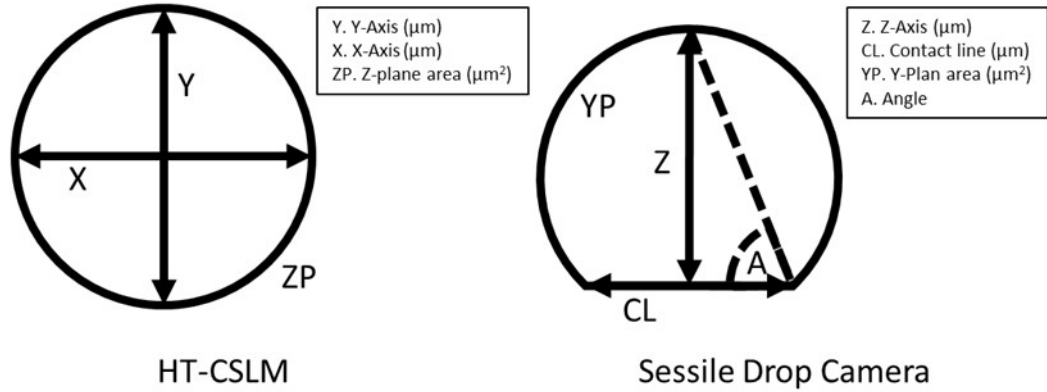
Figure 5-7: Schematic visualisation of the measurements of the particles from both the HT-CSLM and the SDC.

A similar technique was used in the determination of the liquid fraction in the 50/50 sample tests. At the end of the 60s hold the image was taken of the interface and the visual molten areas were measured to gain a percentage of liquid in the frame.

5.1.3 Horizontal Tube Furnace (HTF)

To produce pre-reduced ore, a horizontal tube furnace was used to partially reduce iron ore from Fe_2O_3 to FeO as outlined in Equations (2.4 - 2.6). The temperature can reach 1600 °C and is heated with an electrical heating source. The tube is made of 99.7 % alumina with the dimensions of 1100 mm in length, 85 mm in diameter and 1.5 mm in wall thickness.

The tube furnace can fill with an inert atmosphere to aid the reduction of the ore. The gas used was Argon with purity of 99.999 % and the gas is introduced into one end of the tube with an exhaust outlet on the other end of the tube. The sample size was of 50 mm in diameter with a sample weight of 40 g and placed in the centre of the tube to the optimal position for the heating elements

HTF tests have been conducted so that pre-reduced iron can be produced at different percentages of reduction. Both the effects of time and temperature have been investigated to deduce the effect of increasing each factor separately and simultaneously. All tests were completed in the furnace under an atmosphere of argon so that reduction occurs slowly via a purely diffusion driven mechanism (transfer of oxygen into the low oxygen potential gaseous atmosphere).

Samples of different iron ores were placed in an alumina crucible dried in a Muffle furnace for 2 hours at 200 °C. The two variables of temperature are tested in

slightly different methods. The dried samples are placed in a HTF in an atmosphere of argon and at differing temperatures and times. The sample is cooled and measured to see the amount of weight lost for a measurement of reduction.

5.1.4 Titration

To calculate the level of reduction of the ore, the Fe^{+2} content is measured with a redox titration to measuring the standard reduction degree. The method follows that outlined in the international standard (ISO 9035: 1989) [67]. The chemical reaction is given in reaction 5.1.

$$Cr_2O_7{}^{2-} + 14H^+6e^- \rightarrow 2Cr^{3+} + 7H_2O \tag{5.1}$$
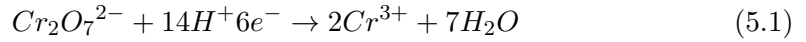
This process uses potassium dichromate instead of potassium permanganate because of the inherent benefits of the dichromate. These include availability in high purity and stability up to its melting point. Aqueous solution is not attacked by impurities like organic matter hence the solution is not affected by storage. The solution is also not affected by light like that of the permanganate. While the Fe ion were released into solution after dissolved in hydrochloric acid (40 %).

The stock iron ore received from Tata steel Europe was tested to gain the Fe^{2+} and the two sections gained from the accretion sample also from Tata steel Europe.

5.1.5 Differential Scanning Calorimeter

The Differential Scanning Calorimetry (DSC) study was done using a NETZSCH Thermal Analysis STA 449 and used to evaluate the accretions and reactions between the iron ore and flux material. The maximum temperature that the equipment can reach is 1500 °C. The DSC has a stage made from platinum where 2 samples can be placed, and this is where a sample and the reference can be placed. The system also has a sample magazine in which a multiple sample can be sit and an automatic sampler, which the system can be automated. An image of the equipment is presented in Figure 5-8.
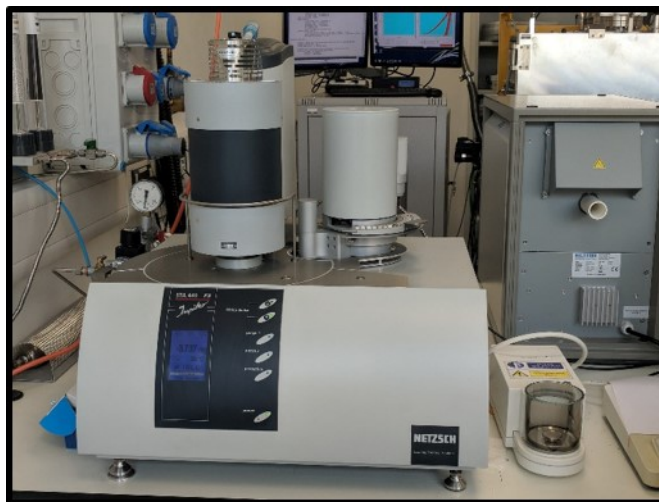
Figure 5-8: An image of the NETZSCH STA 449 DSC.

The system is operated by NETZSCH-Proteus-61 software, which controls the temperature program including heating rate. This also controls the gas flow into the equipment, which has potential for an inert atmosphere (argon in 99.999 %), synthetic air (80 % nitrogen and 20 % oxygen) and reactive gases (CO_2). The Scales used to measure sample is made by (Satorius) and has been accurate to 0.001 mg.

The samples used are incompatible with alumina due to the nature of the samples, so the crucibles used were platinum crucibles. However, the nature of high temperature of the experiment still causes issues of the platinum crucibles and the platinum stage. To fix this the samples have an alumina spacer to protect from this issue. This may cause some thermal lag, but this is easily fixed by calibrating the equipment to account for this. A labelled image of the sample stage and set up with platinum crucibles is presented in Figure 5-9. The samples were heated to 1550 °C at 10 °C/min and were cooled to 1000 °C 10 °C/min. This was repeated three times and on the final cooling the sample was cooled to 20 °C.
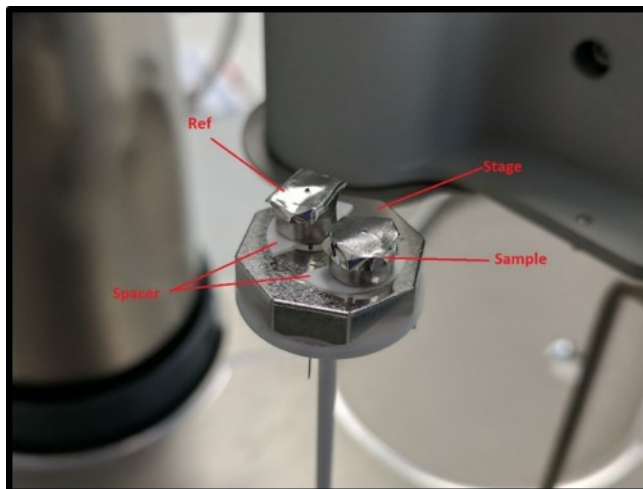
Figure 5-9: Image of the sample stage set up with platinum crucibles and alumina spacers with labels.

5.1.6 SEM

5.1.6.1 Material preparation

Samples were prepared for SEM analysis by mounting them in epoxy resin due to the porosity of the samples. The resin is made using EpoThin^{TM} 2 Epoxy Resin and EpoThin^{TM} 2 Hardener in a two to one ratio. Once mixed the resin was moved to a vacuum desiccator to remove trapped gas bubbles in the sample and left for 24 hours to cure at room temperature. The samples once cured are cut to show the interface between the two materials in the reactions both seen in section 3.4.1 and remounted in the same epoxy as before. The material is ground to a flat surface using $Si - C$ grinding pads incrementally increasing the grit from 800 p through to 1500 p. The sample is polished using Buehler AutoMet^{TM} 250 Pro-Grinder Polisher with oil-based diamond suspensions with particle sizes 9 μm, 3 μm to 1 μm in turn. This routine is done without the use of water so as not to affect the anhydrous CaO in the samples.

5.1.6.2 Scanning Electron microscope

The SEM used for this study was a mixture of a Zeiss Supra 55VP SEM and JEOL 7800F model. Both have an acceleration voltage between 1-20 kV, fitted with a FEG source and EDAX analysis system. As the material used is non-conducting, this causes charging disorders due to the discharging of electrons from the sample. To counter this the sample is gold-coated and use of sliver DAG applied to

the edge of the sample.

5.1.7 X-ray Computed tomography

X-ray computed tomography (XCT) was used to investigate the physical structure of the accretion. This method uses x-ray radiation to obtain 2-D image slices of the sample which when compiled together a 3-D image can be visualised. The technique is non-destructive which is keen for the correlative approach of investigation needed to understand macro-micro relationships of the material. The Scanner used was a Nikon X-TEK XTH 4.3.1 which has far greater resolution when compared to a medical CT machine and can detect small defects. XCT is already being used in industry and is used to detect voids and cracks in a material on both the surface and the internal surface. When applied to the accretion a map of pours cracks and other structural anomalies that can be seen.

The process works by pointing an X ray source at the sample on a rotating table, which is in line with a detector, creating a back projection on the detector. After the scanning is completed, the full projected images are reconstructed using Nikon's associated reconstruction software. Using analysis software (in this case Aviso^{TM}) the image can then undergo grayscale thresholding and segmentation allowing for the quantitative measurement of physical structures. A schematic of the scanning process is presented in Figure 5-10. [68].
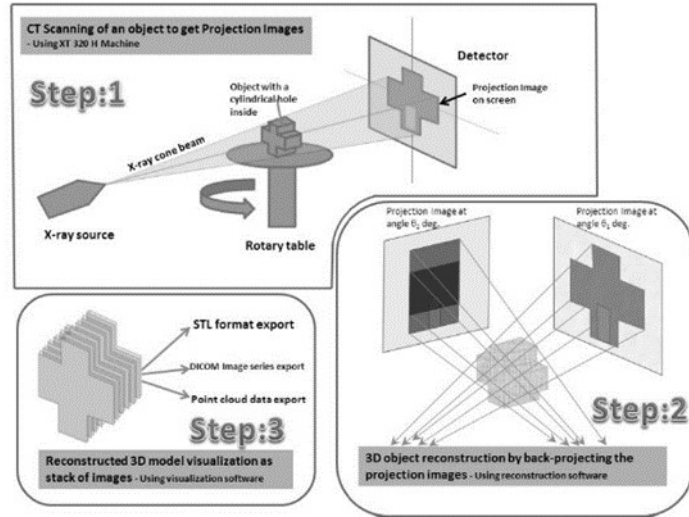
Figure 5-10: A schematic representing the imaging process of the scanning a sample in a XCT. [68]

5.1.8 FactSage^{TM} Calculations

FactSage^{TM} was used in this chapter to determine the theoretical melting point of particles taken from the bulk iron ore. Each of the particle's compositions Table 4-2 and Table 4-3) were imported to the program using and these were used in FactSage^{TM} equilibrium calculations to determine the theoretical melting point of the material. This was when the program showed the sample to be 100 % liquid slag. This was then further expanded by reacting different levels of CaO to the individual particles to test the effect of the addition of the CaO on the melting point. The samples were reacted with an addition 5 wt. %, 10 wt. %, 15 wt. %, and 20 wt. % of CaO. This allowed for the experimental result and theoretical result to be compared. For the limestone samples, CaO was used instead of $CaCO_3$ as the $CaCO_3$ data would complicate the system.

5.2 Evaluation of novel Experimentation

Throughout this work, different experimental methods have been used, ranging from well-known techniques such as SEM, chemical titration, and DSC to more novel and unique ways of using equipment and developing on existing techniques used in the steelmaking industry research including HT-CSLM, XCT and a HT-CSLM based sessile drop method.

This chapter evaluates the novel techniques used in terms of success and ways to improve. This will help in moving these techniques forward and progressing these techniques for use in the research relevant to the steel industry or for modification in other industries.

5.2.1 HT-CSLM

The HT-CSLM is a key piece of equipment used in this work, though the use of a HT-CSLM may not be novel in its use within high temperature experimentation. This study has used methods that open a new aspect of the equipment in both sample design and the addition of a second viewing angle. Below is an analysis of these novel methods showing the benefits, drawbacks and improvements that can be made for future use in other researchers.

5.2.1.1 50/50

During the investigation of iron ore and Ca-based materials reactions as seen in Chapter 7, the HT-CSLM was used to examine a crucible filled with the two ma-

terials with an interfacial boundary in between. This allowed the interface to be tracked in situ at high temperatures with the HT-CSLM and helped analyse three different flux materials (lime, limestone and BOF slag). This showed how they each react differently with the iron ore. The quenched samples were then analysed further with more common post experimental methods such as SEM and EDS, showing how the reactions progressed through different temperatures and the composition of the molten material between the two materials.

The main benefit of this method was the in situ visualisation of materials at temperatures above 1300 °C and gives new insight into how each material interacts with iron ore where furnaces that are more conventional would rely solely on post experiment analysis. The HT-CSLM gives a view of the whole reaction and though post experimental examination is valuable and used in this series of test it is a snapshot of the reactions. Another benefit is that the way the sample is set up is it can be expanded to other materials in terms of slags or other reactions at high temperatures. The interface between the materials can give kinetic information on diffusion of materials across an interface or even through a material.

The drawbacks of this process are firstly the sample is only viewed from a top-down plainer view. This means that the depth of the sample cannot be examined, and it relies on the top surface to be indicative of the entire sample. The second planer view can be gained from SEM analysis; however, the in situ nature is lost. The second is due to the nature of examining slags at high temperature raises the importance of selecting a correct crucible. Through the beginning of the experiments, the molten slag began to eat the alumina crucibles and had the potential to interfere with the chemistry of the reaction being studied.

5.2.1.2 Sessile drop camera (SDC)

The use of a second camera with the HT-CSLM allows a second planer view of a sample. The modification allowed for a second angle for the high temperature reactions between two materials. This was done through the removal of a side port directly in line with the sample stage. The samples in these experiments were a single particle (iron ore) on the pellet (flux). The reaction between two materials was tracked and measured using image analysis software such as ImageJ. The shrinking of the particle observed from the SDC, and the growth of the molten pool observed from the HT CSLM allowed for a kinetic study of the iron ore particle and the Ca-based material.

This method showed promise as a way of increasing the capabilities of the HT-CSLM. The addition of a second planer view allowed the side profile of reactions to occur. This can add another layer to kinetic studies. This second planer view could

also introduce the studies of slag wettability at high temperatures that could become an interesting topic slags or metals interacting with refractories. Using the current format of experiment, the kinetic studies at these high temperatures can be explored.

The results collected in Chapter 8 found some issues. The first issue was to get a side profile shot of the sample, as port was removed unveiling the sample; however, this means that the chamber did not have a controlled atmosphere. Any reactants that will have an adverse reaction to air or require an inert atmosphere needs to find a solution. An airtight seal with a quartz window can rectify this so an atmosphere can be controlled with the use of the SDC.

Another issue was the SDC was not integrated into HT CSLM controls meaning the cameras were controlled separately. The SDC needed to be studied to determine the same starting point of reactions and start the recording. To omit this problem the cameras can be connected by a system via code or use a visual cue to show the start of the reaction.

The samples used in the test also showed evidence of thermal expansion in the pellet and changed the position of the particle. The camera would then need moving to accommodate this change. The understanding of the materials used in the system so that the camera can be refocused on the sample or prepping the samples by sintering or heat-treating so the sample does not go through such expansion.

The final drawback of this method is the lack of crucible used in the experiment, as the walls of the crucible did not block the view of the camera. The sample sat on two different spacers one alumina and the other was platinum to give some protection to the gold-plated furnace. This overall meant that during the experiments BOF slag was not used, as this would have turned molten and damaged the confocal chamber. The two live feeds form the cameras allowed samples to be monitored so no molten material got near the edge of the pellet. However, to run this experiment in a safer fashion a low walled crucible could be made to add another layer of protection to the equipment.

Chapter 6

Characterisation of an Accretion Sample Taken from HIsarna Pilot Plant to Investigate the Agglomeration in the CCF

6.1   Introduction

Accretions also known as "scabs" and "scaffolds" are formed through the gradual accumulation of material by adhesion onto a growing mass and are an unavoidable part of the BF process due to the nature of the process. High temperatures, aggressive flow rates and the presence of volatile chemicals, all play their part in the formation of accretions. In most cases, a thin layer of accretion on the refractory is not only accepted but also desired in the BF and other furnace designs [69] even though this slightly decreases the furnace volume and obstruct the movement of material. The accretion lining is vital to keep a healthy refractory, protecting it from the corrosive effects of gas and liquids present in the process and thus extends the life of the refractory, reducing the cost of replacing them. This encouraged behaviour is called scabbing [70].

Controlling the accretion layer is vital as an unwanted growth can be disruptive and lead to shut down of the entire plant if it builds beyond reasonable levels. As such, this issue has an ongoing effect on the productivity of a plant and was historically a common problem for a BF [71],[72]. There were two way in which this was managed the first being to lower the flow of cooling water to melt off the accretion [73]. The other was to shut down the furnace for cleaning which most

commonly resulted in using explosives to dislodge the accretions [74]. Thankfully with modern process control, developments in modelling and increased use of in situ sensors in the BF [75], this issue is now uncommon.

6.1.1 Factors of accretions in a Blast Furnace

Though the definite mechanisms for the formation of accretions is not completely known, some factors are considered major contributors. These include alkali circulation, Zinc enrichment, quality of sinter and Coke, cooling and the burden distribution [76].

Alkalis are the metals that are found in group one of the periodic table. In the BF, this is predominantly K and Na. These elements react with materials found in the BF, forming different complexes, dependant on reactant and environment. The temperature of the different sections of a BF determines the complexes that form and changes as they circulate up and down the furnace's temperature zones. The different regions is presented in Figure 6-1 [77] along with the complexes that potassium forms including carbonates, silicates and cyanides [78].
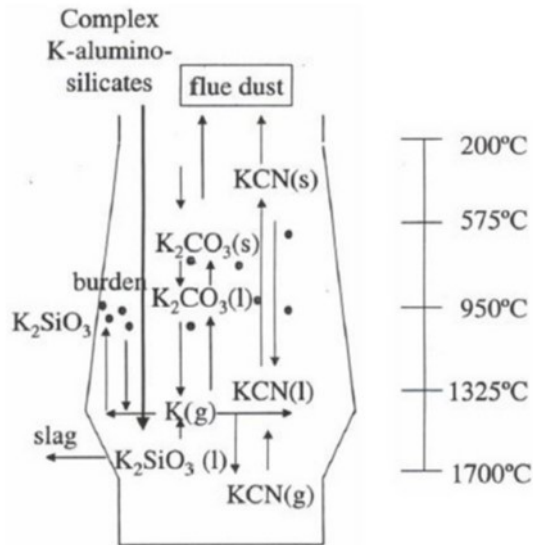
Figure 6-1: Schematic of the blast furnace and with the circulation of potassium in the BF. With the complexes it form, where they form in the furnace and the temperature [77]

Zinc enrichment is introduced in the furnace in two ways. The first is in impurities in the ores in the forms of zinc oxides and more complex forms such as $ZnO \cdot Fe_2O_3/2ZnO \cdot SiO_2$ and recently, it has been introduced by using recycled

steel in the process [79] [80], with zinc being a common coating material for steel products in use. The Zinc vaporises at temperatures higher than 1200 °C however in the higher stack of the BF, condenses on the colder walls, and descends back to the burden. For this reason, zinc accretions are found higher in the stack than alkali-based accretions.

The quality of the sinter and coke is also a factor in the formation of accretions. As the residuals in the ores such as alkalis, zinc and sulphur content can be found in the screening process. Also sinter morphology played a big role in the build-up of accretions due to the interactions of fines and coarser sinter [81]. This led to a worldwide shift towards skip screening on coke and sinter in the 1950s and onto double-deck screens excluding a large part of fines from the burden [82]. Allowing for the fines and coarser sinters being charged independently.

Burden distribution is controlling the material in the furnace. Meaning that the furnace maintains the right levels with the correct distribution of materials such as ores, coke, and fluxes. A poorly distributed burden will cause a slower decent down the furnace and lead to longer residence times of material within sticking zones of the BF. The best way to combat this is to keep the furnace stocked of all materials because if this is not sufficient the layers of the burden will be uneven.

The cooling method for the furnace is another factor in the formation of accretions as the development and use of refractories has changed over time. Cooling used to sustain the temperatures of the shell to prevent material fatigue as any buckling or failure would result in severe damage. More modern furnaces implement a self-lining refractory wall which is cooled to allow a thin layer of accretion to form, acting as a protective layer for the refractories during the process [83]. Both these allow thermal balance to increase the longevity of the process. However, if the cooling is too much then this accretion layer can be allowed to grow and thus a problematic scaffold can form.

Another way that cooling is introduced into the BF is through the addition of materials. The carrying gas (normally nitrogen) is not heated thus, accretions are most commonly found around tuyeres as material enters the process and are described as mushrooms due to their shape [84]. Like that of the accretion layer on the refractories the mushrooms are wanted to protect the tuyeres and is called a shrouded injection and a schematic is presented in Figure 6-2 [85].
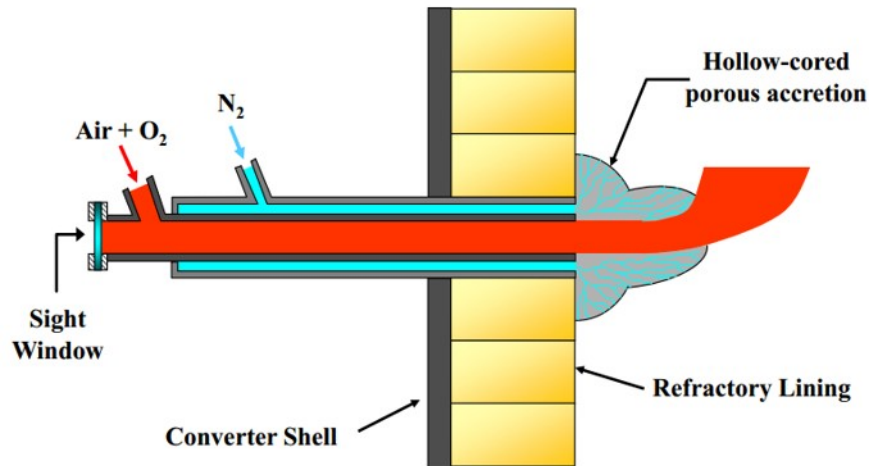
Figure 6-2: A Schematic of a shrouded injection system of a BF with the mushroom accretion forming around the injection site. [85]

6.2   DRI processes

In DRI, a reducing atmosphere is used to reduce the Iron ore partially through the reduction of the Fe_2O_3 to FeO. The gases used are normally H_2 or CO/CO_2 which is generated from coal or methane gas. The product from this process is sponge iron made from the iron ore being reduced but maintaining the form of the iron ore and usually occurs in the temperature range of 800-1200 °C [86]. The product produced from this method has the physical properties of the ore and contains significant porosity allowing gas flow through the material unlike pig iron produce from the BF [87]. This product is reported to also be used in the EAF instead of 100 % scrap steel as it helps create foaming which protects the furnace walls and extends refractory life [88]. However it is likely included from a more pragmatic point to ensure chemistry of produced steel is met, avoiding out of scope levels of residuals which are likely to occur from 100 % scrap usage [80].

As it has undergone partial reduction sponge iron has a higher FeO content than iron ore, however the sponge iron also has an increased weight percentage of SiO_2 due to the loss of weight from reduction [89] which means comparatively the product with have high acidity within the process. The higher FeO content in the slag will change the chemistry of a slag and understanding this may affect accretion formation.

6.2.1 HIsarna

HIsarna is an accumulation of a DRI method in the CCF and a smelting reduction vessel in the SRV. The CCF product is like that of DRI due to the reduction of the ore in this region by reducing gases from the hearth, except the CCF process is at a higher temperature and creates greater fluidity within the material. Accretions are causing issues in the development of the process, as passageway between the CCF and SRV is being blocked. This pathway is vital as it allows the movement between the two sections and complete reduction of the ore. Trial runs showed evidence of accretions building in the process that is presented in Figure 6-3. The image is taken from inside the SRV looking up into the CCF and the accretion growth is blocking the pathway. Previously discussed contributions to accretion formation are likely active in this part of the process including cooling, sinter, coke quality and the presence of residuals. In addition, other factors that are unique to HIsarna that may promote accretion build-up such as the refractory cooling system, turbulent mixing, and the flexibility of raw materials.

Figure 6-3: A labelled image looking up from the SRV to the CCF and showing the accretion that forms in HIsarna.

The cooling system implemented in HIsarna is more pronounced than a standards BF. This is due to the highly turbulent nature in the way it mixes material in both the CCF and the SRV [6] [42]. The refractories take the brunt of this and are used up at a faster rate and the cooling is used to help them last longer [39]. The utilisation of a more aggressive cooling and mixing means that the furnace will have cooler areas to which material can adhere and grow into an accretion.

HIsarna and other novel ironmaking processes focused on cutting CO_2 have the ability of using a more varied raw materials compared to the conventional iron-

making process [26]. Materials such as unsintered ore, Coal instead of coke and the ability of using scrap metal as an additional source of iron. This fulfils the goals of cutting CO_2 from the ironmaking method but also introduces residuals such as alkalis. The addition of scrap with iron ore in the process has caused issues with the increased levels of zinc in the process. Evidence of this is seen in HIsmelt where high levels of zinc dust was left in the furnace and FINEX® has found zinc accretions which have disturbed the process [90],[91].

For these reasons, it is beneficial to understand the accretions that are forming in HIsarna and learn how they are forming by looking at multiple aspects of a sample obtained from Tata Steels Europe HIsarna pilot plant in IJmuiden and studying its structure, composition and melting properties. The structure was interrogated at the external and internal structure including the pores in the sample. The composition provided information about the chemical make-up and compared to the ore used in the process and the quantity of zinc in the material. Finally, the melting and solidification of the material were tested to understand the conditions needed for the accretions forming.

6.3   Results

Looking at the accretion visually there were two distinct parts, which can be described as a dense area with smaller pores with less dispersion and a porous region with larger pores and more concentrated. Another feature in the sample is a crack down the middle, which acts as a soft border between the two defined regions. These sections are presented in Figure 6-4. With labelled areas under optical microscope, these two areas were examined further and is presented in Figure 6-5.
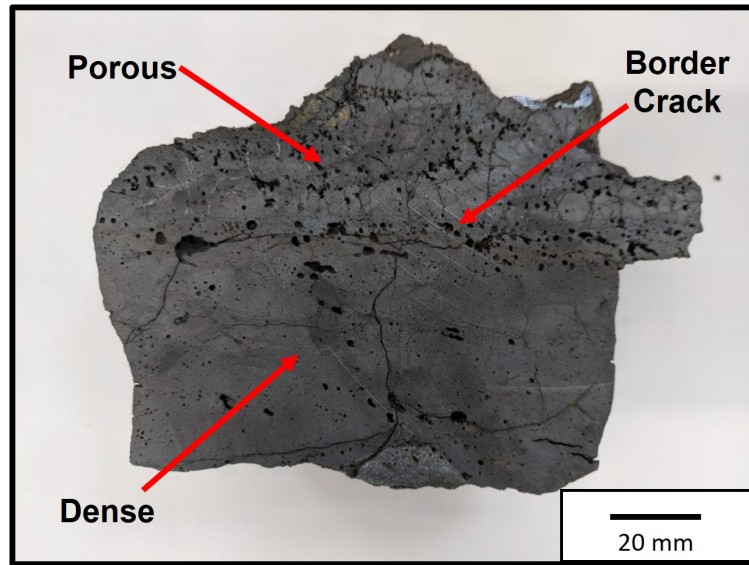
Figure 6-4: Image of the accretion bisected and labelled to distinguish between the dense and porous sections of the accretion.
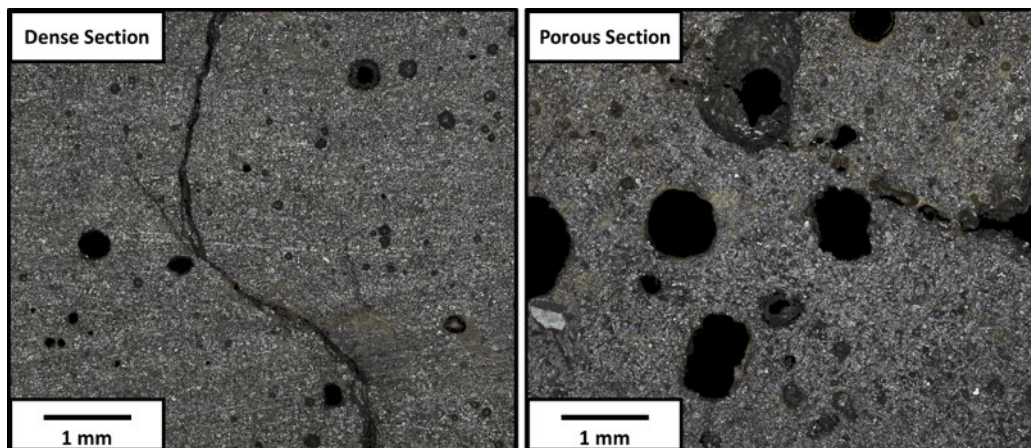
Figure 6-5: Images of the accretion sample under an optical microscope of both the dense and porous sections of the accretion.

The accretion was examined using SEM and section of both the dense and porous areas is presented in Figure 6-6. Both have a similar structure with larger iron particles suspended in a matrix of other oxides. In this slag matrix, there is faint dendritic crystal formation, which is more visible in the porous section than that of the dense section. The porous section shows large pores in the material clearly seen in the bottom corners of both optical and SEM images. The dense section does not show any large pores however there seems to be smaller imperfections on the

surface that are potential smaller pores.
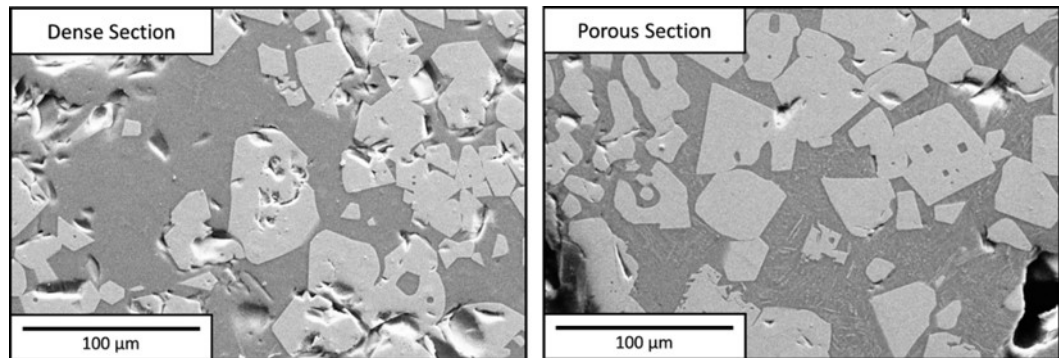
Figure 6-6: SEM image of the accretion with an image of the dense section and porous sections

Figure 6-7 shows SEM and EDS data of the dense section and the slag area showing the microstructural properties. In image A there is a dendritic crystal forming in the slag matrix between the larger particles. Image B shows that the particles are iron, and the slag matrix is composed of Si, Al, Ca, and other elements. Image C shows an EDS map of the detected iron and confirms that the dendritic formation in the slag is iron precipitating out of the slag.

In Figure 6-8, the microstructure of the porous region of the accretion is examined. In image A there is visible lines in the slag matrix of the sample. Image B show the EDS map of the elements discovered in the sample and the particles are still iron and the slag region is similar composition as the dense area. Image C is the EDS map of the sample of the calcium in the sample and the needle like structure becomes prominent showing its high calcium content, and the lack of calcium within the iron particles.
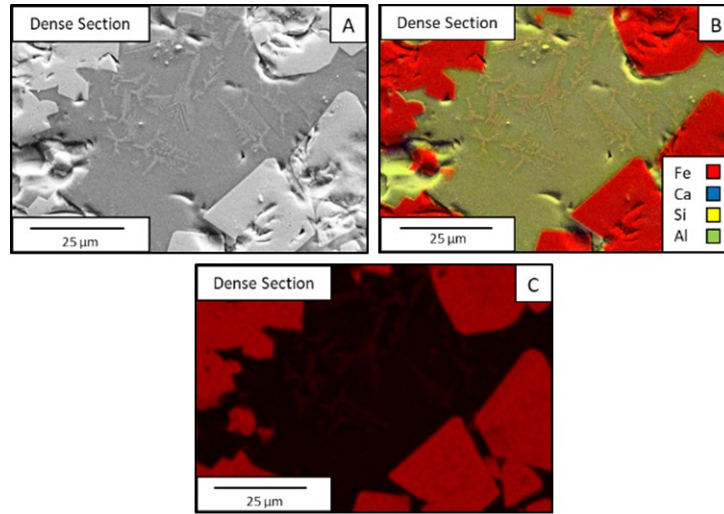
Figure 6-7: SEM and EDS images of the slag interface in the dense section of the accretion. A) SEM image of the slag interface showing the dendritic formation. B) EDS map of the area and the colour code of the elements found. C) The iron only overlay of the EDS map showing the structure to be iron precipitate.
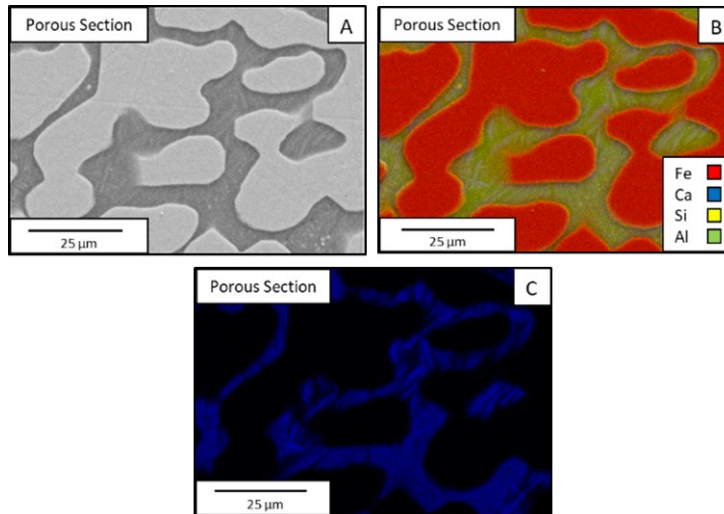
Figure 6-8: SEM and EDS images of the slag interface in the porous section of the accretion. A) SEM image of the slag interface showing a needle like structure. B) EDS map of the area and the colour code of the elements found. C) The iron only overlay of the EDS map showing the structure to be calcium needles.

6.3.1   XCT of the accretions

X-ray Computed Tomography was used to analyse half of the accretion detecting pores that are present in the sample and with each pore the coordinates and size

of the void was measured.

The Images in Figure 6-9 show grey scale XCT slices of the sample where the pores are black and the material present is in lighter colours depending on density. Image A shows a slice from the Y-plane and is a similar picture to that of the photo image in Figure 6-5 with the dense, porous and crack visible. Image B shows a slice from the X-plane as this is the axis where the change between the structures labeled as dense and porous . The images doesn't show the crack as the X-plane is parallel to the crack and therefore will only ever be in one of the regions. Image C show a slice of the Z-plane again the denser and porous section of the accretion are visible as the left side of the image shows the dense section and the porous on the right. The boarder between them is also clear and sits just right of the samples centre and seems to be layers of pores before transitioning into the porous section. where the pores are greater in number than the dense section with some larger pores dispersed through the sample. In image D the sample is shown in a 3 D form with the sample cut in the Z-plane with the whole sample visible in block at the bottom, and semi-transparent at the top.
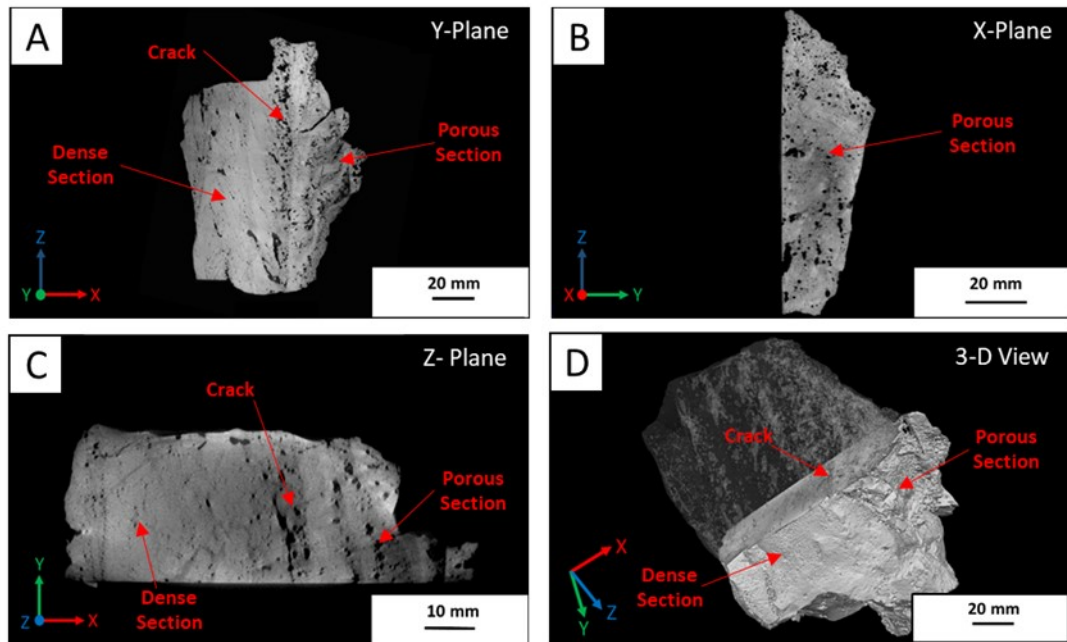
Figure 6-9: Four images taken from the XCT of the accretion sample. A) An image of a slice of the XCT taken from the Y-axis. B) An image of a slice of the XCT taken from the X-axis. C) An image of a slice of the XCT taken from the Z-axis. D) An image of the XCT with sample in 3D representation.

The pores of the accretion has are visualised in Figure 6-10. Image A shows

the sample and its orientation with some of the pores visible on the surface of the as seen in the multi colour spots while Image B shows every single pore detected by the test. The pores seem to be collected towards the left of the image and a cluster of small pores in the right side near the edge of the sample. From both images it is evident that the pores that allowed the labels of porous and dense are constant throughout the entire sample.
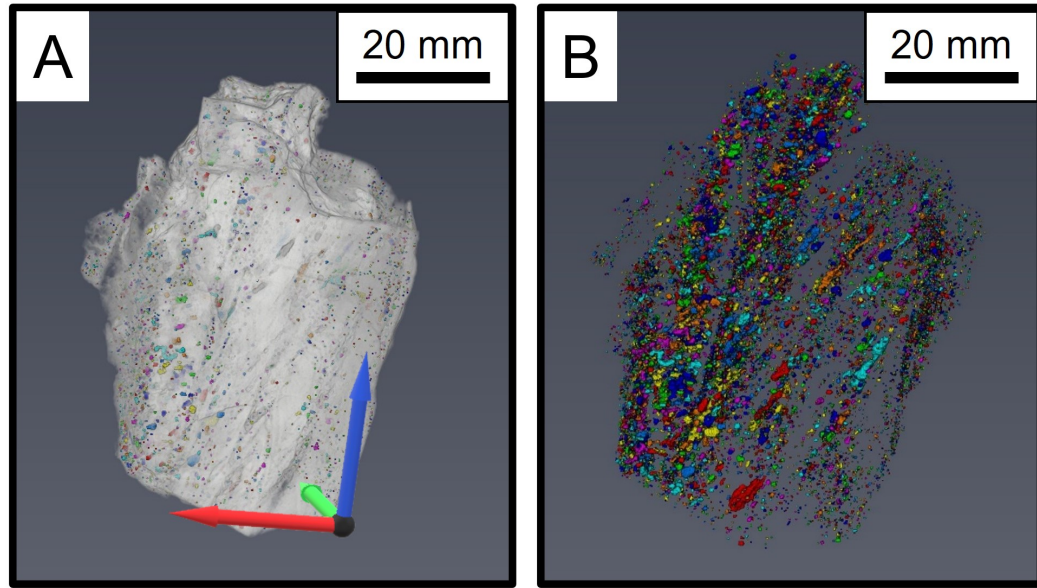
Figure 6-10: Two images gained from XCT showing the pores in the sample colour coded to denote size. A) Shows the outer samples in grey with some of the surface pores poking through and showing the orientation of the sample. B) Shows only the pores in the sample found throughout the sample.

Overall 19443 pores were detected in the sample and the coordinates of the central point and volume of each one was measured. The size of sample was calculated as the maximum X, Y and Z distance with the X-axis having maximum distance of 76.97 mm, Y has a maximum distance of 67.67 mm and the Z distance has a maximum of 12.78 mm. The data also says that the smallest pore had a volume of 4.19x10-4 mm^3, while the largest pore had a volume of 75.046 mm^3. The average pore size was calculated to be 0.126 mm^3. Using the number of pores and the size of the sample the porosity was calculated for the whole sample and each of the defined sections. The whole sample had a porosity of 4.02 % while the dense section had a porosity of 3.69 % and the porous section had a porosity of 4.41 %.

Using the coordinates of each pore is plotted showing the distribution of the pores throughout the sample along each axis. The pore data was taken from

63

Table 6-1: The XCT data given from the pores of the accretion samples sorted by their X coordinates and spilt into 0.5 mm sections. Showing the number of pores and the average volume of pores per section.

X-Axis

Start (mm)	Finished (mm)	Number of pores	Average volume of pores (mm^3)
0	0.5	222	0.006
0.5	1	1218	0.034
1	1.5	2053	0.040
1.5	2	1692	0.068
2	2.5	1634	0.094
2.5	3	2046	0.186
3	3.5	1629	0.242
3.5	4	1239	0.141
4	4.5	1050	0.304
4.5	5	1031	0.181
5	5.5	1217	0.140
5.5	6	1234	0.152
6	6.5	1477	0.118
6.5	7	1259	0.061
7	7.5	401	0.023
7.5	7.697	41	0.015

5 mm sections from each axis, the number of the pores in each and the average pore size. For each axis any pattern to the pore distribution throughout the sample can be extrapolated.

As shown in both Table 6-1 and Figure 6-11, the X-axis shows that the number of pores in between 1 mm to 3.5 mm along the X-axis is high in number, when compared to the rest of the sample. This is due to the number of pores dropping for the rest of the sample between 3.5 mm to 7 mm. There is a small increase in this region between 6 mm to 6.5 mm but there is no continuation of this trend and may be due to a crack running through this area. Also at the beginning and the end of the sample the number of particle drastically decreases however this is due to the shrinking Y and Z-axis. The volume of the pores shows that in the range there is a high concentration of pores with a small volume which corresponds with the idea of this being the porous section of the sample. In the middle of the sample the size of the pores increases and at the point where the number of pores is at its lowest. It was also found that the volume of the pores is highest with 0.304 mm^3 was found in the middle of the axis.
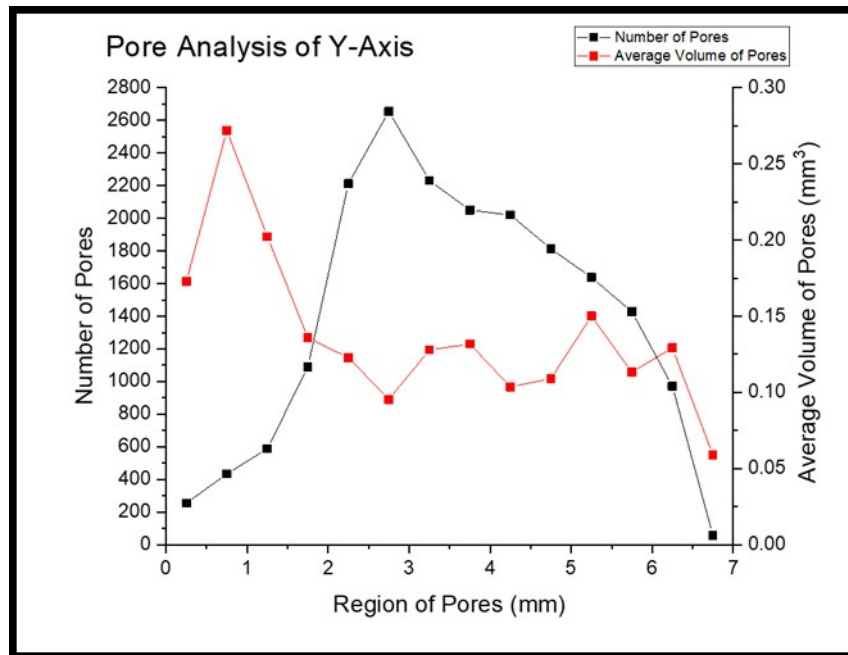
Figure 6-11: A graph showing the dispersal of pores along the X-axis with the number of pores and the average volume within 0.5 mm sections of the axis.

In Table 6-2 and Figure 6-12, the pores are along the Y-axis. The graph is equivalent to the shape of the sample as the volume of each section changes with the size of the X-axis and Z-axis. At the beginning of the sample (0 mm and 1.5 mm) the number of pores is low however the volume is relatively high. This could be due to surface imperfections being classed as pores leading to larger volumes. Between 1.5 mm and 3 mm the number of pores drastically increases while the volume drops to approximately 0.1 mm^3. From this point on the number of pores starts to slowly decrease from 3 mm to 6 mm before a sharp drop off to the samples end (6 mm to 6.767 mm). The volume is consistent until the 6.5 mm to 6.767 mm where it drops to 0.059 mm^3. The plane does not show any of the features (dense, porous or crack) due to this plane having all sections in each slice as it runs perpendicular to the boarders.

Table 6-2: The XCT data given from the pores of the accretion samples sorted by their Y coordinates and spilt into 0.5 mm sections. Showing the number of pores and the average volume of pores per section.

Y-Axis

Start (mm)	Finished (mm)	Number of pores	Average volume of pores (mm^3)
0	0.5	255	0.173
0.5	1	434	0.272
1	1.5	588	0.202
1.5	2	1089	0.136
2	2.5	2212	0.123
2.5	3	2655	0.095
3	3.5	2232	0.128
3.5	4	2050	0.132
4	4.5	2020	0.104
4.5	5	1813	0.109
5	5.5	1639	0.150
5.5	6	1427	0.113
6	6.5	971	0.129
6.5	6.767	58	0.059
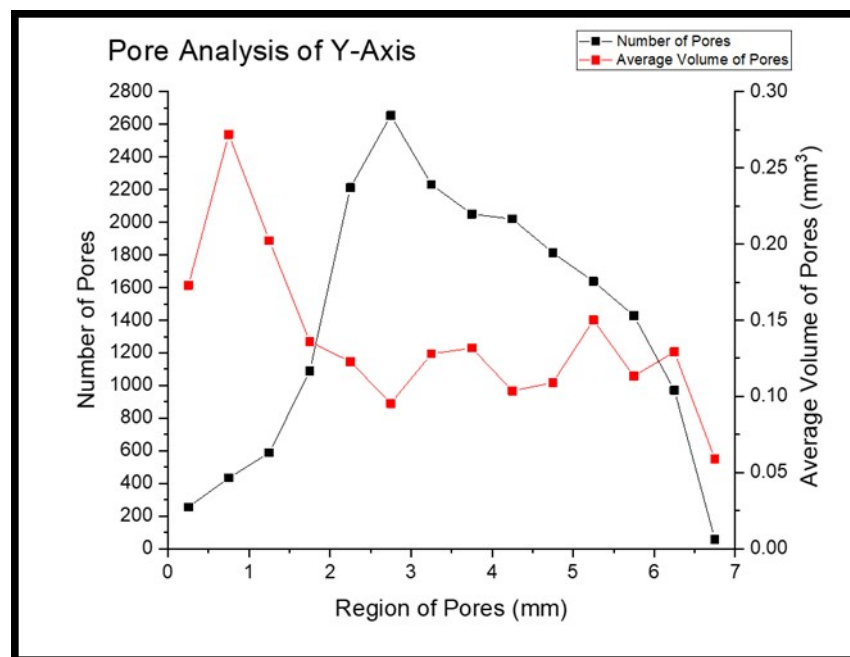
Figure 6-12: A graph showing the dispersal of pores along the Y-axis with the number of pores and the average volume within 0.5 mm sections of the axis.

Along the Z-axis as seen in Table 6-3 and Figure 6-13, the shape of the graph

Table 6-3: The XCT data given from the pores of the accretion samples sorted by their Z coordinates and spilt into 0.5 mm sections. Showing the number of pores and the average volume of pores per section.

Z-Axis

Start (mm)	Finished (mm)	Number of pores	Average volume of pores (mm^3)
0	0.5	50	0.069
0.5	1	163	0.154
1	1.5	280	0.216
1.5	2	432	0.105
2	2.5	464	0.062
2.5	3	542	0.133
3	3.5	768	0.175
3.5	4	892	0.140
4	4.5	950	0.078
4.5	5	1024	0.111
5	5.5	1169	0.173
5.5	6	1444	0.083
6	6.5	2151	0.160
6.5	7	1908	0.141
7	7.5	1399	0.120
7.5	8	1246	0.105
8	8.5	944	0.102
8.5	9	792	0.167
9	9.5	793	0.121
9.5	10	703	0.074
10	10.5	381	0.124
10.5	11	298	0.119
11	11.5	261	0.095
11.5	12	226	0.062
12	12.5	151	0.162

is linked to the the shape of the sample along the Z-axis. The number of pores increase at a stable rate up to 6 mm then there is a sharp increase in the middle of the sample. After the peak, the number of pores drop quickly then levels off around the 8 mm to 9.5 mm section before another large drop and a slow decline to the end of the sample. The area of the pores fluctuates around a middle point (0.125 mm3) however there is no visible trend in the changing of volume. Like that of the Y-axis the crack and sections are not visible due to the features running through the axis.
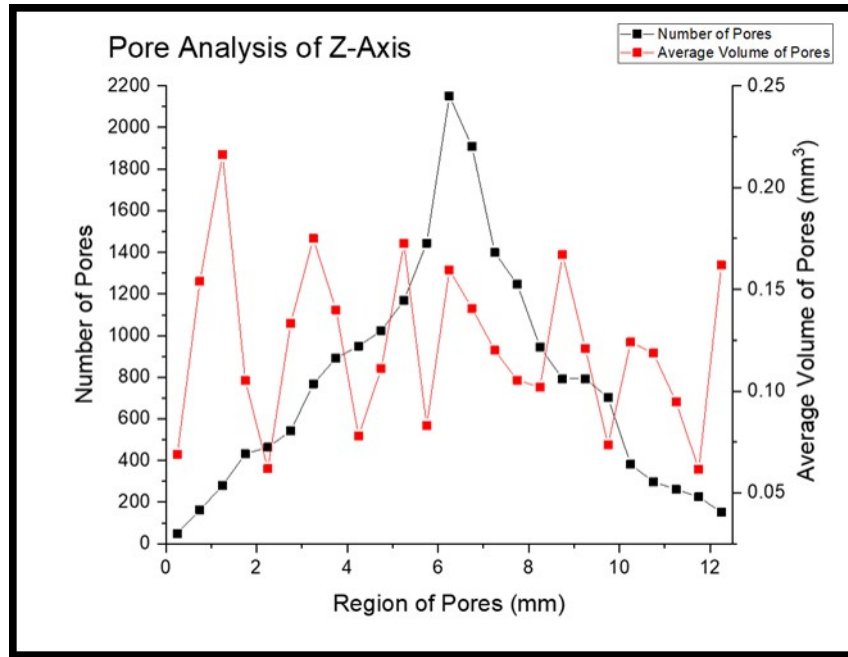
Figure 6-13: A graph showing the dispersal of pores along the Z-axis with the number of pores and the average volume within 0.5 mm sections of the axis.

6.3.2 Melting properties

Overall, the plains consistently follow the trend of more pores in the middle of the sample where the most mass is. Unless there was a significant structural anomaly that was sectioned out, such as the separation of the porous and dense section in the X-axis view. The volume of the pores showed little trend throughout the material but the areas on or close to the surfaces had evidence of a greater pore size.

The accretion melting point is examined to determine if there was a difference between the dense and porous section.

The dense section results in Figure 6-14 show the phase change temperature boundaries of solidification. The dense section shows that the material starts to melt between 1463.5 °C and 1473.5 °C. The peak temperature denotes the crystallisation temperature (T_c) is between 1500.6 °C and 1506.7 °C.
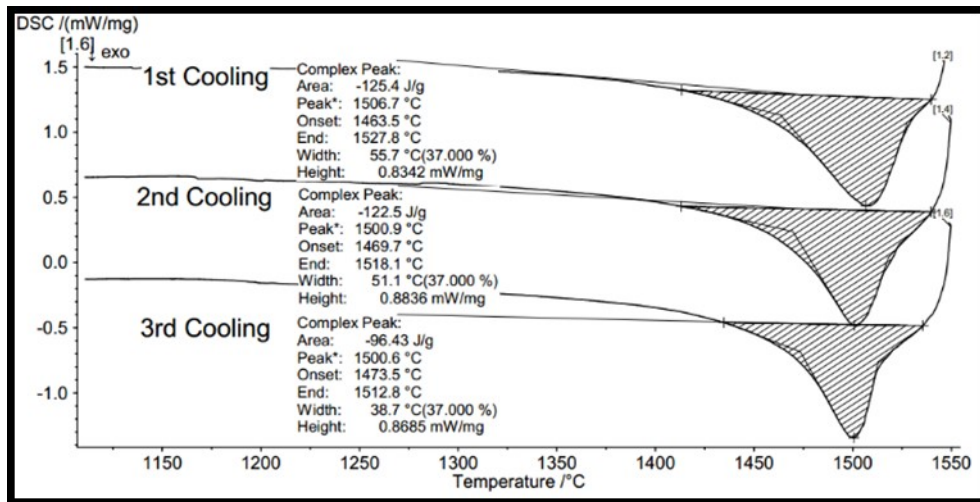
Figure 6-14: A graph showing the DSC results if the dense section of the accretion. This includes three of the cooling measurements of the sample and the temperature it solidifies.

The porous section results in Figure 6-15 show that the temperature at which solidification ends is between 1463.5 °C to 1473.5 °C. The peak of the crystallisation temperature (Tc) is between 1522.4 °C to 1525.1 °C.
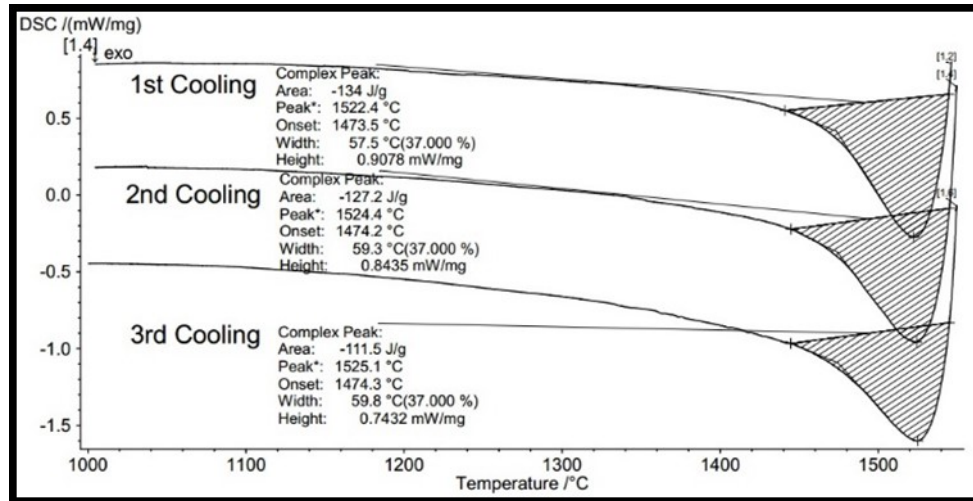
Figure 6-15: A graph showing the DSC results if the porous section of the accretion. This includes three of the cooling measurements of the sample and the temperature it solidifies.

6.3.3 Composition

The EDS analysis was used to gain the composition of the sample of both defined sections. The results in Table 6-4 show the composition of the iron ore from Tata Steel that was used in HIsarna's pilot plant. An increase in the impurities most significantly SiO_2, Al_2O_3 and CaO was detected in the accretion compared to the original ore. The potassium content also increases significantly from 0.2 wt. % to 4.4 wt. % for the dense region and 3.4 wt. % in the porous section. The Fe_2O_3 content is lower in the iron ore than in the accretion as the iron ore has 60.99 wt. % while the dense section has 65.8 wt. % and the porous section has 71.0 wt. %.

Table 6-4: Table showing the compositions gained from EDS of the accretion of both the Dense and Porous sections.

Accretion Section	Fe_2O_3	SiO_2	Al_2O_3	CaO	K_2O	MgO
Iron ore	60.99	6.31	1.71	1.57	0.2	0.64
Dense	65.8	15.1	9.1	5.1	4.4	0.5
Porous	71.0	14.1	7.5	3.6	3.4	0.4

When comparing the section, a lower Fe_2O_3 content in the dense section which is replaced by the detected impurities. The porous section conversely has a higher Fe_2O_3 with lower levels of impurity.

As it is difficult to determine the oxidation state of the iron complexes by EDS, titration was used to find the FeO content in the accretion samples. The results show (Table 6-5) that the dense section has a higher FeO content than the porous 18.16 % and 17.10 % respectively. The FeO value given for the iron ore was 0.95 % significantly lower than that of the accretion samples.

Table 6-5: The results from the titration of the accretion sample showing the FeO % in the samples from the Dense and Porous sections.

Accretion Section	Titration 1 (FeO %)	Titration 2 (FeO %)	Titration 3 (FeO %)	Average (FeO %)
Dense Section	18.09	18.27	18.14	18.16
Porous Section	16.94	17.22	17.13	17.10

6.4 Discussion

6.4.1 Orientation of the Sample in HIsarna

The structure of the accretion sample surface images Figure 6-4 show two distinct sections of the accretion defined as porous and dense. This structure can give information about the orientation of the accretion on to the refractory walls. The pre-reduced ore created from DRI processes produces a more porous structure hence the name sponge iron and can assume a similar product would be made the CCF of HIsarna [92]. The process should continue to form a molten material when moving to the SRV. However, with the presence of the accretion this is clearly being inhibited by processes conditions.

The pores come from the reduction of the iron from its haematite (Fe_2O_3) state to its magnetite (Fe_3O_4) form [78]. This would suggest that the more porous section would be more reduced than that of the dense section of the accretion. From the results gained from the titration of the accretion sample, there is not a significant difference between the sections with regards to reduction progress. The results showed a 1 wt. % difference. The dense section of the material showed a higher FeO content at 18.16 wt. % with the porous section giving 17.10 wt. %. These results suggest that the structure of the sections should be the opposite way around if purely dictated by reduction progress.

Other factors that could influence this miss match of expectation include the time in the CCF and the cooling rate of the accretion. Linking this back to the results, it is reasonable to suggest the dense section of the accretion formed first and has been present in the process longer due to its higher reduction level.

The cooling rate of slags influences the solidified structure. A quick quench gives a more "vitreous solidification" while a slower cool allows for more growth of the crystals and thus more time for crystal growth [93]. This idea is promoted by the results in the microstructure between the iron-based particles where, the formation of dendritic FeO_x in the area is seen. The porous section had a vast amount of unordered Ca needles forming in the region that suggest a quicker cooling of the area. The dense structure shows dendritic precipitation of iron in the slag matrix between the iron particles suggesting a slow cool rate for the structure to grow. Cooling of the dense section next to the furnace wall is likely to be driven by heat loss during the process, whereas the porous section may have been formed only when the process was shut down and thus a more rapid reduction of temperature would have dictated solidification features.

6.4.2 Pores, Structure and Foaming

The XCT of an accretion has not been done and allowed examination of the internal structure of the sample with a focus on the pores present in the structure. The method is non-destructive and allowed further test to be conducted on the sample with the information gained from the scans. It also provided quantitative data to back up the visual clues form an external examination. It also allowed us to theorise how these structural properties effect foaming and further build-up of these accretions in HIsarna.

As this is from the solidified sample taken after the furnace had cooled, the structure may not be like its structure in during the process. However, without in situ testing of the accretion, the structure studied can offer important findings on how this material can cause process failure. In Figure 6-4, the cross section of the accretion is shown. The visible crack seen in the top part of the material suggests that the structural integrity of the accretion is not secure. Though breakages of the accretion will help stop the blocking of the passage between the CCF and the SRV this can cause other issues in terms of process.

An accretion break off into the SRV can contribute to increase foaming due to sudden additions of reactive iron oxides that reduce rapidly increasing the CO/CO_2 production of the process. In addition, the breakdown of the accretion and the release of the trapped gases within could contribute further to process instability.

Increasing the FeO in a slag will increase the possible reactions with carbon in the process, which increases the amount off CO, and CO_2 produced. The additional gas formed by the reaction will aerate the slag [93]. As the foaming levels can be tracked during the process, steps to decease this can be taken within normal process. However, this rapid addition of accretion material could cause uncontrollable levels of foaming leading to the need to shut down the process.

The Second idea of introduction of the reducing atmosphere in the bath is due to trapped gas in the accretion. As the CCF uses CO and CO_2 to pre-reduce the iron ore in the cyclone, this gas can be trapped in the pores in the accretion. From the XCT scan of the sample the presence of 19443 pores and a total volume of space detected was 2453.29 mm^3. This was from a relativity small sample that was approximately 609375 mm^3 in total volume. The sudden release of the trapped gas in the slag will contribute to more foaming.

6.4.3 Composition of the accretion

The composition of accretions in CCF is not like those that will be found in a BF or any other ironmaking process. Though the materials used in the process are the same such as iron ore and Ca-based materials they are not mixing with other materials like in a BF. It is important to look at the information from how these build up happen in these processes and compare to the HIsarna sample to see where they differ.

Alkali content is a key factor in BF accretion formation and as such, it is a key issue to analyse to see if similar phenomena occur in the HIsarna process. In Table 6-4, the compositions of the ore used as well as the accretion in the form of the subsections outlined as dense and porous is presented. These results captured the wt. % of K_2O in each of the materials which was 0.2 wt. % in the bulk Iron ore, 4.4 wt. % in the dense section of the accretion and 3.4 wt. % in the porous section of the accretion. This is evidence of a significant enrichment of potassium in the process being deposited in the region of the accretion.

As seen in the circulation of the potassium in Figure 6-1 there are several of complexes that K_2O favours at different regions in the BF. However, the BF has a temperature in the hot region of 900 °C to 2000 °C with the top exhaust cooler at 250 °C. While in HIsarna, the temperature in the CCF is 1450 °C while the SRV holds a temperature of 1450 °C to 1500 °C. [94]

The lower temperature variation in the process means that the potassium has a narrower set of complexes to form. The main complexes that potassium forms in the BF all are in the liquid phase at temperatures over 1100 °C and at this temperature, the most common is K_2SiO_3. However, other complexes are K_2CO_3 and K_2O (which is unstable above 770 °C) [95]. This means that for the alkali to have a role in the accretion build up in the HIsarna process the refractory cooling will have to reduce the temperature to lower than 1100 °C.

The levels of zinc in HIsarna could be high due to the flexibility in raw materials use as HIsarna has the option to dope the charge material with scrap metal adding a high level of Zn to the process. In the analysis of the accretions' compositions, there was no detected zinc. As the boiling point of zinc is 907 °C, this is substantially lower than that of the operating temperature of HIsarna leading to the assumption that Zn plays no role in the build-up of the accretion during operation. However, this may cause issues in any off-gas capture system and may lead to dust in the furnace after shutdown.

6.4.4 Viscosity on Build up

There is evidence that the turbulence of both the CCF and the SRV is the cause of the build-up of material around the joining of the two sections. With the CCF the cyclone created in this zone pushes molten material to the wall where it flows into the SRV. As seen in Figure 6-3 the accretion is building up in the transition area where the molten slag flows into the SRV. The build-up in this location could be down to the flow of the material slowing and building at the precipice due to the surface tension of the slags as well as the viscosity of the material. Figure 6-16 is a schematic on how the viscosity affects the flow of a liquid in HIsarna.
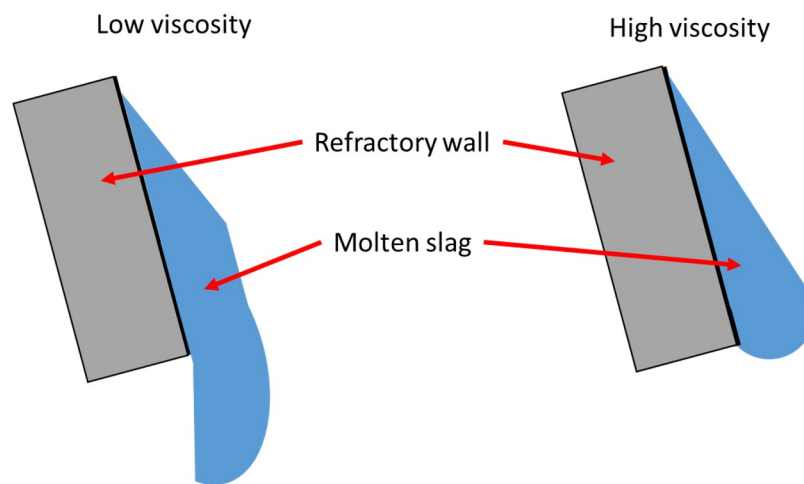
Figure 6-16: A schematical look at how a low viscosity material and high viscosity liquids would flow off the refractory walls of HIsarna. A low viscosity can be seen to flow off the lip easily while a high viscosity would be slower and hold on the lip to surface tension.

The slowing of the dripping material means that the material is against the cooled wall of the furnace and means there is a longer time for the material to cool in this area. If the material solidifies at this region, it will form an area for which the accretion can agglomerate. In addition, as the solidified mass grows the angle for the liquid to flow over will be increasing and result in a longer time in this region of the furnace. Figure 6-17 is a schematic of this phenomena and how the accretion will increase the distance and physics of a liquid flowing on the refractory walls.

No Accretion

Accretion forming

Refractory wall

Molten slag
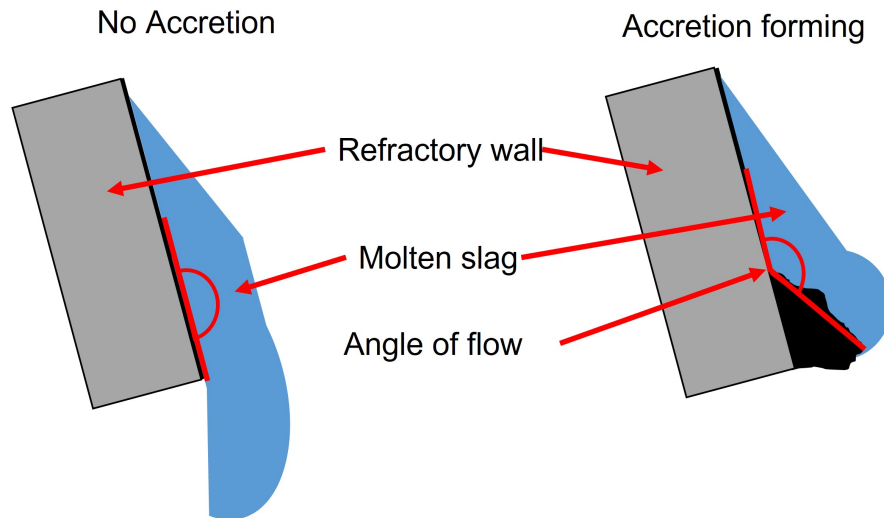
Angle of flow

Figure 6-17: A schematic of how a growing accretion can affect the angle of flow of the refractory wall due to the increased distance and time on the refractories.

The chemical composition of the any slag effects the materials viscosity. Hence using the compositions, the theoretical viscosity of a slag can be calculated using the computational program FactSage$^{\text{TM}}$ [96]. This program uses a modified Quasichemical Model from thermodynamic principles and experimental data for the model.

Using FactSage$^{\text{TM}}$ and the three main compositions from the dense and porous sections of the accretion as well as the bulk iron ore used in the process, viscosities have been calculated. As well as this, the compositions have been calculated with a pre-reduction of 20 wt. %, meaning the Fe_2O_3 in the ore has been converted to 20 wt. % of FeO and how the addition of CaO will affect the viscosity by the addition of 20 wt. % CaO. All these calculations were done at three temperatures 1300 °C, 1400 °C and 1500 °C and is presented in Table 6-6.

Table 6-6: Table of calculated viscosities of the accretion and ore with no additions (standard) with an addition of 20 % CaO and pre-reduction of iron oxide where the iron had been reduces to give 20 % transformation of Fe_2O_3 to FeO (20 % FeO).

Sample		Viscosity (Pa·s)		
		1300 °C	1400 °C	1500 °C
Iron ore	Standard	0.018	0.013	0.01
	20 % CaO	0.051	0.034	0.023
	20 % FeO	0.016	0.012	0.009
Dense	Standard	0.092	0.056	0.037
	20 % CaO	0.103	0.063	0.041
	20 % FeO	0.061	0.04	0.027
Porous	Standard	0.058	0.037	0.026
	20 % CaO	0.084	0.053	0.035
	20 % FeO	0.043	0.029	0.021

The calculations show that the accretion samples have a higher viscosity than the composition of the ore obtained from the bulk sample, meaning the accretion material would flow slower in the furnace than the original ore. This would increase the time on the cooled refractories and lead to potential solidification that could act as agglomeration sites for the growth of the accretion. When comparing the two different accretion regions dense/porous, there is a further difference in the viscosity of the samples. The dense region has a viscosity of 0.092 Pa·s at 1300 °C while the porous section had a viscosity of 0.058 Pa·s. As previously evidenced, the dense section is the first part of the accretion to form due to its structure and composition and the higher viscosity adds further evidence to this theory. The slow flowing nature of the material is likely to spend more time on the walls and thus be more likely to be affected the cooled refractories.

The numbers calculated by FactSage^{TM} give indication on how these compositions will theoretically flow in HIsarna. However, when compared to figures with the viscosities of industrial BF slags the viscosity are between 0.3 and 0.5 Pa·s at 1500 °C [97]. However, these slags are not found in HIsarna and SRV slags have been reported at 0.05 Pa·s [98]. This is like the results gained for the accretion samples calculated without any additions. This means that the slag found in the SRV of HIsarna will be a similar of these materials. As this does not need to flow inside the process this is not as much of a factor until tapping the slag. In the SRV there is a high level of slag movement in a way that is described as a "splash" and is throw in the vessel [99]. This volatile behaviour could throw material into the CCF, and the viscosities do show evidence of this occurrence. However, the

composition does not show evidence for this being a common occurrence to affect the formation of the accretions.

HIsarna is partly a DRI method of iron making, especially in the terms of the CCF and the iron ore is reduced in the CCF meaning that that the accretion sample will have more FeO than the injected ore, EDS measured the sample to have 20 % conversion of the Fe_2O_3 into FeO. This is potentially higher than the pre-reduction found in HIsarna's trials; however, it is within the region of little effect on the calculated viscosity. These results show that the viscosity decreases with the increase of FeO in the system in all of the samples calculated and has been shown by other sources [100]. The increased fluidity should help in the transfer of material from the CCF to the SRV. Meaning the higher the reduction made in the CCF the more of a benefit in terms of viscosity.

However, the higher level of FeO does come with other issues in terms of the increased amount of Fe in these accretion samples. High silica content along with high iron oxide content in the form of wüstite (FeO) can be a chemical pathway for slag accretions to form. These oxides form more complex compounds with a higher melting point and intern reduce the fusing temperatures on the refractories and increase the potential of material to grow into an accretion [92]. Another problem with the increased FeO is that when a chunk of accretion drops into the SRV bath it can cause foaming. This is because as the FeO is introduced to the hot bath it reduces to Fe releasing CO increasing the volume of the slag from foaming [101].

The viscosities were also calculated with an addition of 20 wt. % of CaO to the bulk ore, dense section and porous section of the accretion examining the effect of the addition of this as a fluxing agent on the viscosity. The results from FactSage^{TM} shows that the addition of CaO increases the viscosity suggesting that this will not aid the flow of material. As the slower flow rate will take longer to flow through the CCF to the SRV increasing the possibility of accretions.

However The benefit of the CaO addition is the reduced melting point of the iron ore and reduce the possibility of accretions [62]. This is not considered for the FactSage^{TM} calculations as it takes temperature as a constant in the calculation to give a value regardless of state hence theoretical. Experimentally the addition of CaO would decreases the melting point of the system and mean the viscosity at lower temperatures are lower and possible. Z. Ge, et al, shows this as the viscosity of a slag is measured at 1454 °C at different CaO/Fe_2O_3 ratios. The sample with 0:10 ratio has a viscosity of 1.8 Pa·s but the 2:8 ratio has a 1.1 Pa·s. At higher temperatures (>1500 °C) the 0:10 ratio has a lower viscosity then the 2:8 ratio [102]. As the removal of the accretion in the CCF is important to the process the

lower viscosities at these lower temperatures are required.

6.5   Conclusion

The structure, composition and physical properties gained from the analysis of the accretion sample from HIsarna provided information and evidence for the growth of such material.

The structural differences inside the sample categorised as dense and porous allowed a clear distinction of possible orientation in the process. As the dense section would most likely have solidified slowly as the structure is uniform and allowed the gas to release from the material. In addition, the microstructural crystal formation with the precipitating iron oxide in the slag matrix supports the theory of slower cooling in this part of the sample. Contrasting with the high pore count and high needle like Ca crystals found in the porous section. The dense section is the bases of the accretion formation and points to a slower solidification of the sample and subsequent growth of the accretion. The external porous structure (porous section) could also be contributed to post process shutdown allowing for relatively faster cooling.

The composition of the materials also suggests this orientation as the dense section had a higher quantity of FeO in the sample as found through titration and means the sample had more time to reduce. Along with the orientation information found, the composition of the accretions showed it had higher levels of alkali elements, in this case K_2O. These are historically known to cause accretion in the BF however, the higher temperatures of the CCF means these are unlikely to cause solidification. The content of SiO_2 in the accretion is considerably higher than the bulk iron ore and may influence the melting point of the sample and react with other compounds such as FeO to make complex oxides. These oxides have higher melting points and thus can form agglomeration points for the growth of the accretion.

Finally, the review of the physical properties showed that the solidification point of the accretion sample was between 1463 °C and 1506 °C. Though this is under the reported temperature of the CCF the higher level of cooling of the refractories in the process may lead to solidification if these areas have lower temperatures. This also means that a lower contact time would be beneficial leading to the theoretical properties of the compositions being calculated. The viscosities were found to be lower than slag in a BF but as the material is known to form an accretion this suggests a lack of flow.

The ore found in the CCF is likely to have a higher FeO content. The

increase of FeO has been calculated to show a lower viscosity that should aid in the flow of material from the CCF to the SRV. However, the high FeO content of such accretions can cause issues such as break off and can cause release of CO from the reduction of the oxide causing foaming. The high porosity shown in the XCT of the sample will mean that a large surface area is present on dropping into the SRV, greatly speeding up any likely reactions.

The most likely reason for the formation of these accretions is the solidification of the material in the CCF due to lower temperatures in this region. A suggestion to fix this is to add a Ca based flux material to lower the melting point of the ore to maintain the liquid state on the refractories. The viscosity calculations have shown this will increase the viscosity however as shown the addition allows for lower melting points. These allow that at lower temperatures the viscosity can flow better and decrease the formation of any agglomeration points in the material.

Chapter 7

Observation of the Reactions between Iron Ore and Metallurgical Fluxes for the Alternative Ironmaking HIsarna Process

7.1 Introduction

Technological advancement and greater understanding of the steel production process have contributed greatly to the improvement in raw material use efficiency in the modern steel industry. However, the nature of the integrated steel plant is still reliant heavily on the use of coal, coke, and electricity. The steel industry contributes to 6.7 % of anthropogenic CO_2 emissions globally [26], which means that CO_2 reduction in the steel industry cannot be ignored as a key step in meeting international climate control agreements. The European Union (EU) has made efforts with the aim of cutting the CO_2 emissions of industry by 80 to 95 % by 2050 [3], however, the steel industry as a whole is estimated to be only 25 to 30 % higher than the theoretical limit of energy consumption possible [26]. Hence, to reach the EU CO_2 emission reduction target, the European steel industry (and morally the wider community) must develop novel ironmaking processes to transform the industry.

HIsarna [36], [103], [43], FINEX® [17] and COREX® [25] are all alternate ironmaking processes being developed to reduce CO_2 emissions, replacing the currently main CO_2 contributing step in production, the blast furnace (BF) ironmaking

process. All the three processes rely on direct reduction or partial reduction of the iron ore. In addition, direct reduced iron (DRI) is a key feedstock for electric arc furnace (EAF) practice in countries such as the USA and Turkey where there is an abundance of natural gas. Direct reduction requires a reductive gas atmosphere, usually CO from coal or natural gas to reduce the ore to iron. Pre-reduction partially reduces the ore before complete reduction of the ore in a hearth or smelting vessel. Reduction of the ore consists of multi-steps shown in Equations 7.1-7.3.

$$3Fe_2O_3 + CO \rightarrow 2Fe_3O_4 + CO_2 \tag{7.1}$$

$$Fe_3O_4 + CO \rightarrow 3FeO + CO_2 \tag{7.2}$$

$$FeO + CO \rightarrow Fe + CO_2 \tag{7.3}$$
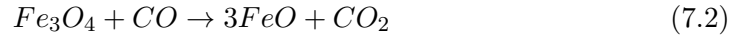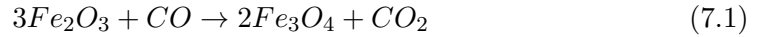
The reduction reactions in these novel ironmaking processes are conducted in solid-state. As in most cases, solid-state reactions are kinetically slower than liquid state reactions and are therefore potentially limiting to the iron production rate if these technologies are to be widely adopted. The rate of this reaction can either be increased through optimising conditions such as temperature, pressure, and variant in iron source or through creating intermediate active species to encourage a fundamental step change in the rate-limiting step of the reaction.

Flux from a metallurgical standing is a chemical cleaning agent or purifying agent, which is used in both extraction and joining of metals. A flux material added during smelting is bound to unwanted minerals to help remove them, forming slags [8]. As this is an important part of the iron making and steelmaking processes, it has seen a large level of interest from the research community. Specifically, on the capability of CaO fluxes as this is an effective flux and already implemented in steelmaking processes due to its price, availability and effectiveness at removing key impurities such as silica and phosphorus [104].

Adding flux in HIsarna in the cyclone converter furnace (CCF – the location of solid state pre-reduction in the process) with the addition of iron ore offers the normal production advantages such as removal of SiO_2 from the ore, but also offers early fluxing opportunity. Due the mixing mechanics, the iron may form an early liquid slag inside the CCF, which should aid the reduction of potential accretions in the furnace, as the lower melting point will stop solidification of the material at cool spots of the furnace. These can cause significant processing problems as pathways can be blocked, for instance the most vital being that between the CCF

and the smelting reduction vessel (SRV – the location of carbon fuel injection and full conversion to liquid hot metal).

This paper will investigate interactions between CaO-bearing fluxes and iron oxide in iron ore. Lime, limestone and readily available BOF slag present a well-established set of CaO containing derivatives due to their current use and availability on a steel plant and the cross comparisons of cleaner and heavily mixed substances. The focus of this study is on each materials ability to encourage the presence of a liquid state within the ore at short interaction times. The phase diagram for CaO and FeO_x which can be found in slag atlas based on the work from Phillips and Muan.[61], [105] Shows that between 0 – 40 % CaO has a strong influence on reducing the melting point of the iron species from around 1600 °C to 1205 °C at the eutectic.[61] The presence of a liquid species as discussed above has the potential to unlock the rate of reduction, with mass transfer of species such as oxygen, phosphorus, and sulphur being orders of magnitude higher in liquid phase compared to solid diffusion.

7.2 Experimental method

Samples of iron ore were placed in contact with the chosen fluxing agent and heated to the designed temperature (1350 to 1450 °C) to begin reaction between the materials. During heating, the reaction between iron ore and fluxing agent is viewed in situ using a High-Temperature Confocal Scanning Laser Microscope (HT-CSLM), and subsequently interrogated using post analysis techniques such as Scanning Electron Microscopy (SEM) and Energy dispersive spectroscopy (EDS). The performance of each flux will be compared by looking at the liquid phase of the composition of the melt and the effects of liquid fraction and reaction mechanism discussed as to their potential of effect on reduction rates.

7.3 Results

A high-grade iron ore (62 % Fe) has been placed into alumina crucible along with three chosen fluxing agents. The two materials have been observed in situ while heated to 1400 °C and held for 60 s. The quenched samples have then been cut, polished, and investigated via SEM and EDS. Each material pair is presented bellow with brief comments on key observations on how the materials have interacted.

7.3.1 Lime – Iron Ore

Figure 7-1 shows the images from the HT-CSLM of the lime (CaO) - iron ore samples. Image A shows the sample before the heating and image B shows the sample after holding at 1400 °C for 60 seconds. At 200 °C the two materials have a distinct interface between the lime on the right and the ore on the left. At 1400 °C the two materials appear significantly changed, with the ore on the left showing evidence of melting – depicted by the bright section near the centre of the image (at the original sample interface). This section was seen to be fluid and appears brighter due to the flat nature of the liquid surface allowing for a larger section of the field of view to be in focus at a single time point.
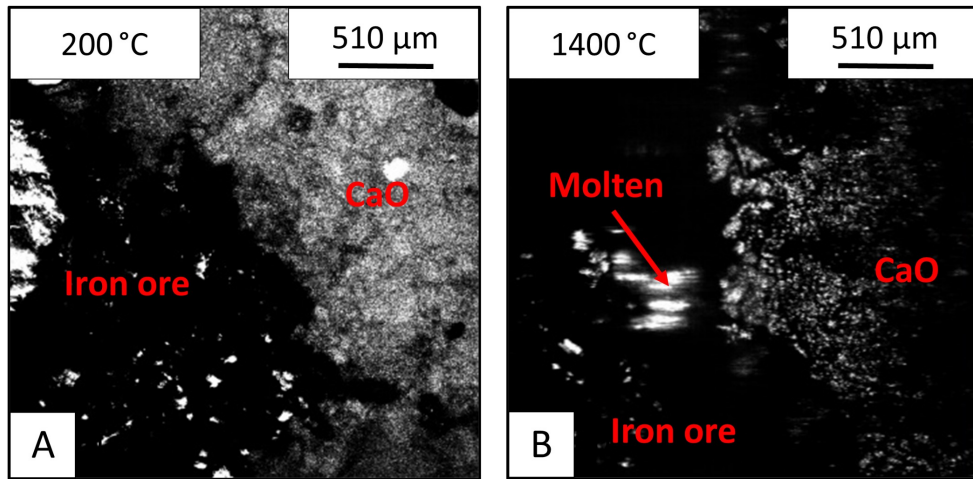
Figure 7-1: HT-CSLM images of lime-iron ore reaction before (A) and after (B) heating.

Figure 7-2A displays SEM images of the sample with the lime on the left and ore on the right. The lime is seen to be unaffected by the heat and seems almost homogeneous. The bulk of ore is also like that before the heat treatment, with the particles appearing angular and discrete showing no signs of fully melting. The images also show that there is an interface region between the two materials, which has undergone significant mixing. The interface is clearer in the EDS mapping (Figure 7-2B) where the purple region shows the elemental mixing of the two main species (Ca and Fe). The liquidus interface which has formed during the experiment appears to strongly adhere/wet the bulk lime phase preferentially.
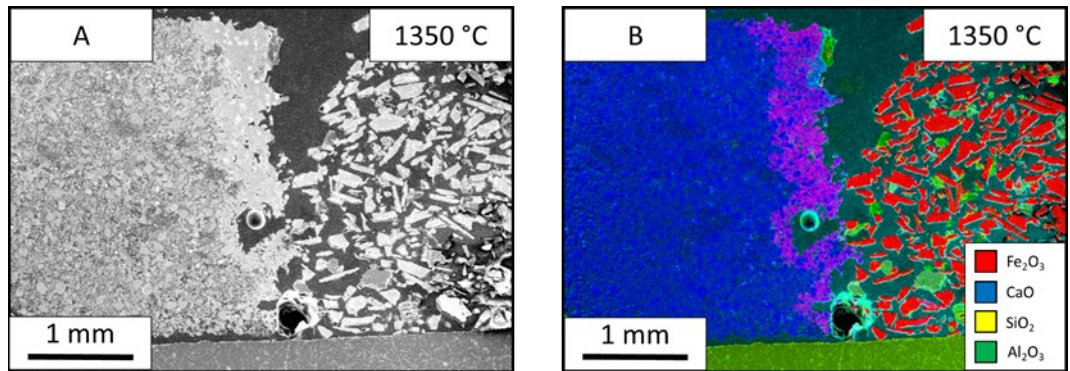
Figure 7-2: Images from the 1350 °C lime sample. A) Electron image of the lime sample. B) EDS map of the lime electron image.
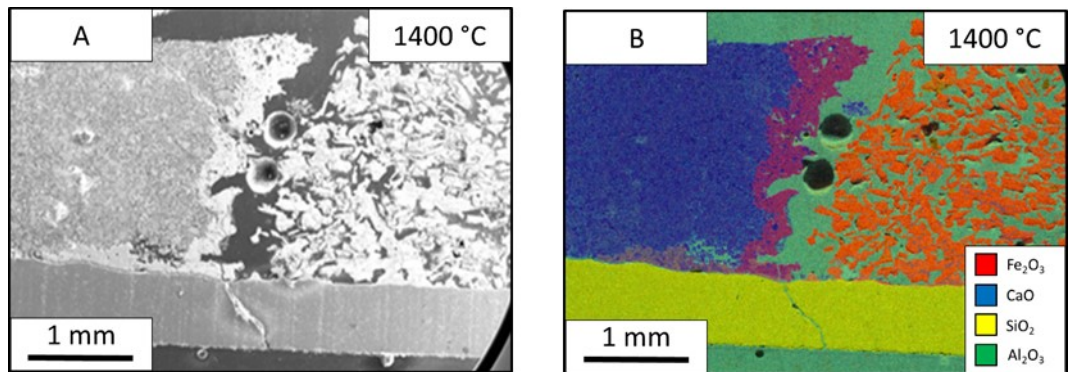
Figure 7-3: Images from the 1400 °C lime sample. A) Electron image of the lime sample. B) EDS map of the lime electron image.
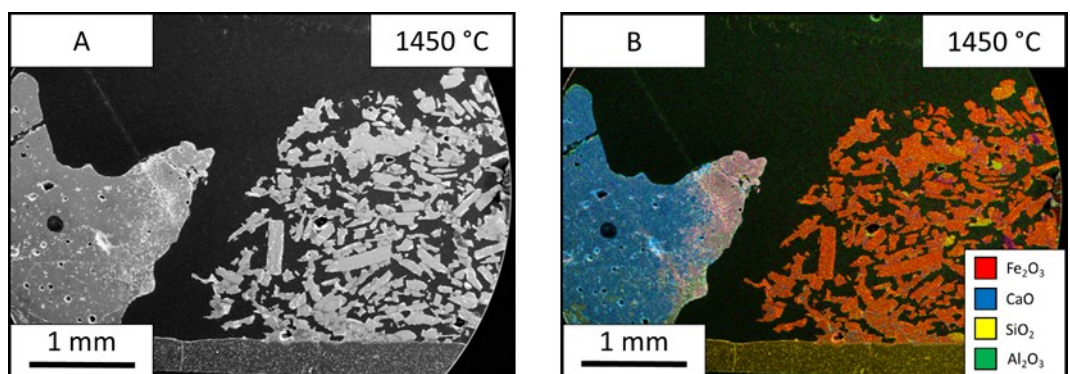
Figure 7-4: Images from the 1450 °C lime sample. A) Electron image of the lime sample. B) EDS map of the lime electron image.

The reaction of lime and iron ore was studied further by holding the reaction at different temperatures of 1350 °C (Figure 7-2), 1400 °C (Figure 7-3) and 1450 °C (Figure 7-4). The SEM images allowed for the measurement of liquid fraction over the three temperatures. These were measured at 16 %, 32 % and 41 % respectively. The increased temperature sped up the reaction and shows the progression of the reaction seen through the holding times. The molten area interface between the two materials is more defined and consistent at the higher temperatures. At 1350 °C, the interface is thin, and the blue calcium is dispersed throughout the molten phase. While the sample after holding at 1400 °C for 60 seconds is thicker in width and shows less dispersion of the pure CaO flux solution interface. The progression of the reaction pathway can be viewed between these three samples with the higher temperatures showing further progression of mixing.

7.3.2   Limestone – Iron Ore

The HT-CSLM images in Figure 7-5 shows that at 200 °C the limestone (right) - iron ore (left) sample (Due to the larger particle size of the limestone, the image is rougher on the surface and is not as clear as the finer particle size lime sample (Figure 7-1). The image after heating to 1400 °C the image shows evidence of liquid in the sample seen in the white areas in the iron ore side of the interface.
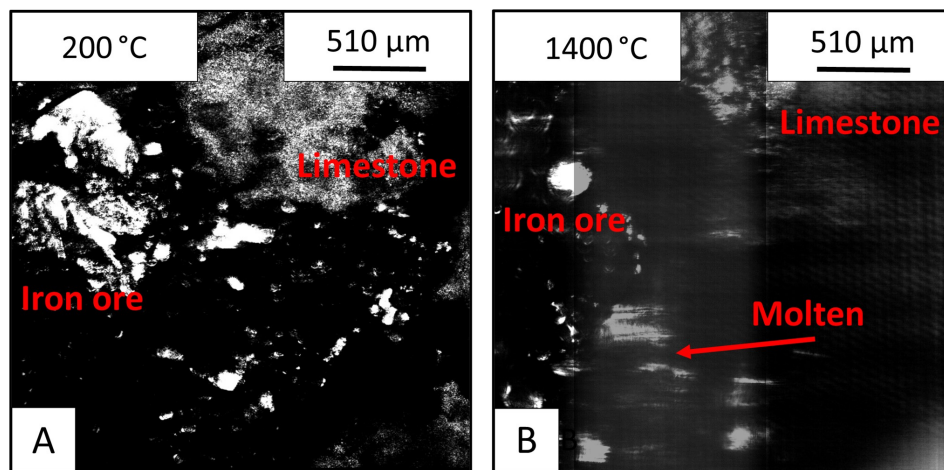
Figure 7-5: Images from the HT-CSLM of the limestone - iron ore sample of (A) before and (B) after heating.
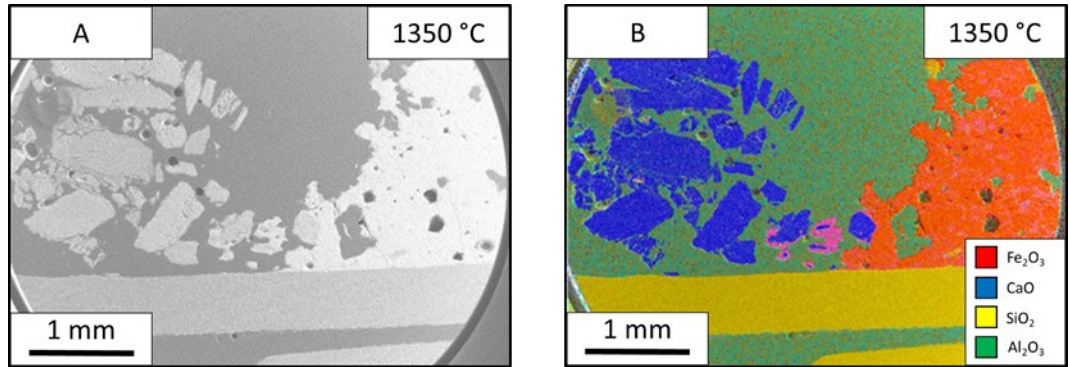
Figure 7-6: Images from the limestone (left) - iron ore (right) sample after holding 1350 °C for 60 seconds: (A) SEM image and EDS mapping of the limestone-iron ore sample.
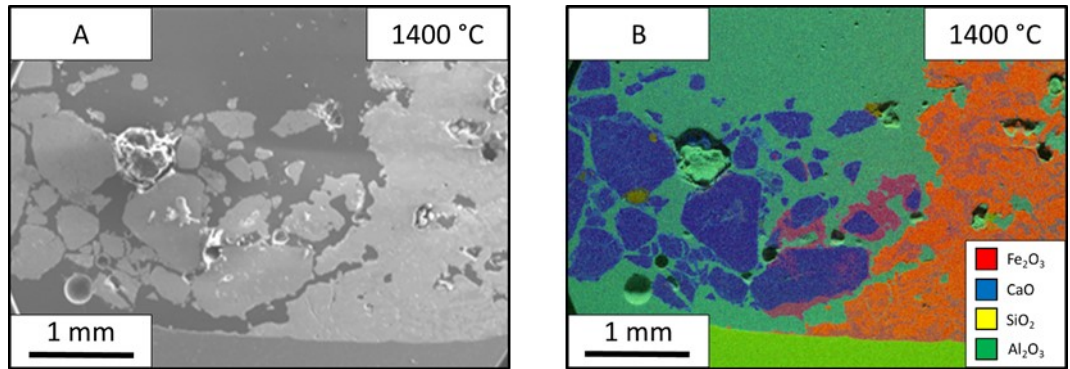
Figure 7-7: Images from the limestone (left) – iron ore (right) sample after holding at 1400 °C for 60 seconds: (A) SEM image, and (B) EDS mapping of the sample.
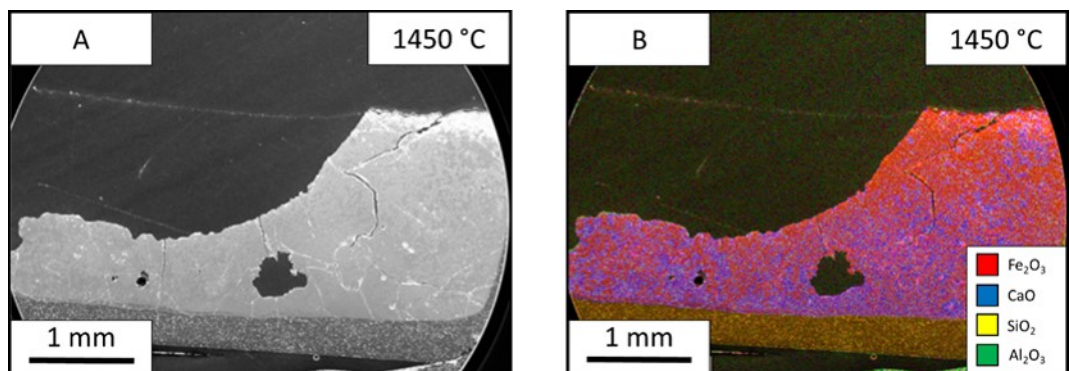
Figure 7-8: Images from the limestone-iron ore sample after holding at 1450 °C for 60 seconds: (A) SEM image and (B) EDS mapping of the sample.

The SEM images of this sample (Figure 7-6A) show that the limestone had a substantial effect on the ore's appearance after heating. Unlike the ore in the lime samples, the ore is more homogeneous with less distinct particles and more connected mass. The bulk limestone in the left of the image seems to look like the material before the experiment. The limestone particles near the ore interface; shown clearly in Figure 7-6B, have an external reaction layer. These particles surrounded by reacting material are the closest this sample came to forming a continuous/defined reaction interface between the two materials.

The test was carried out at three temperatures of 1350 °C (Figure 7-6), 1400 °C (Figure 7-7) and 1450 °C (Figure 7-8), and the liquid fraction was measured to be 26 %, 64 % and 99 % respectively. In the 1350 °C image, the ore is one homogeneous phase; however, there is a dispersion of iron and calcium throughout. Between the two interfaces the limestone particles can be seen mid reaction as the particles have a coating of CaO-FeO solution. The 1450 °C sample shoes a single phase.

7.3.3   BOF Slag – Iron Ore

Figure 7-9 shows the samples of iron ore and BOF slag as observed via HT-CSLM. The slag (right) is less bright than the fluxing phase in the previous samples, but the interface is still clearly visible before the experiment. The Images taken after the heating show that unlike the previous samples, molten material is present throughout the crucible, not only in the ore side or at the interface.
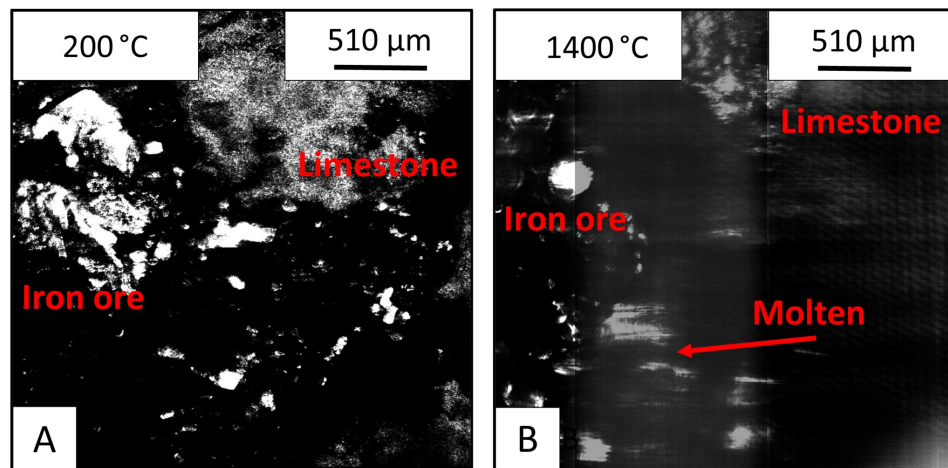
Figure 7-9: Images from the BOF slag-iron ore sample after holding at 1350 °C for 60 seconds: (A) SEM image and (B) EDS mapping of the BOF slag – iron ore sample.
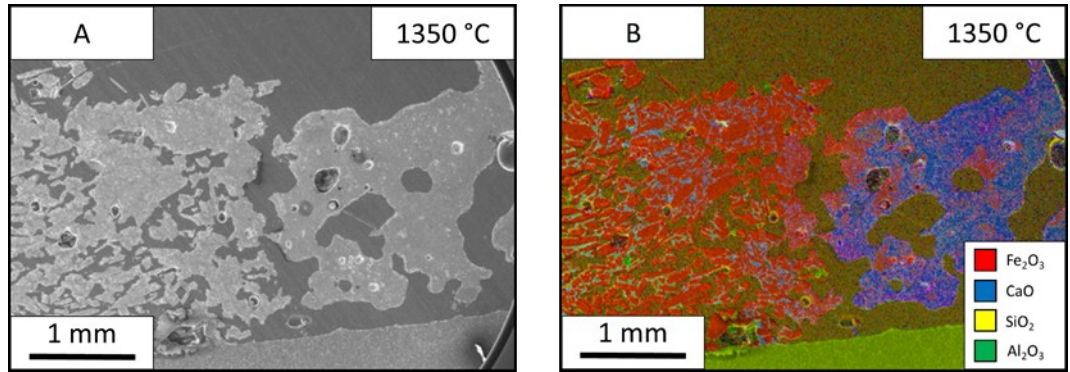
Figure 7-10: Images from the HT-CSLM of the BOF slag - iron ore sample: (A) before and (B) after heating.
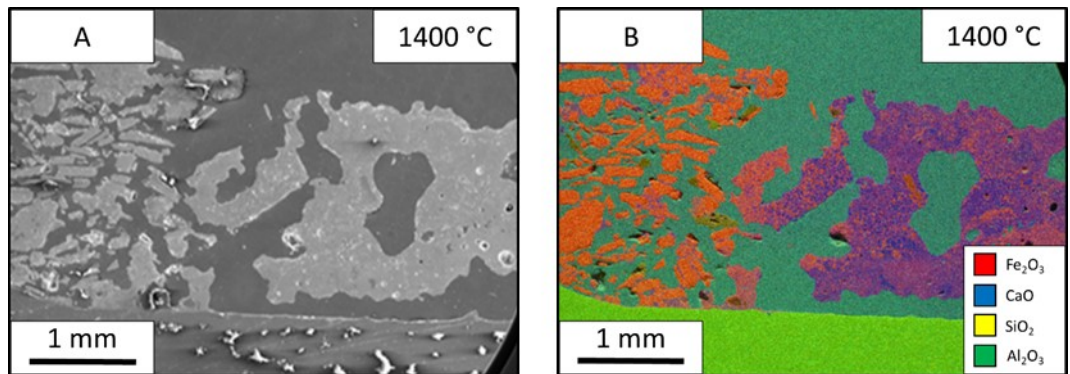
Figure 7-11: Images from the 1400 °C slag samples. A) electron image of the BOF slag sample, B) EDS map of the BOF slag electron image.
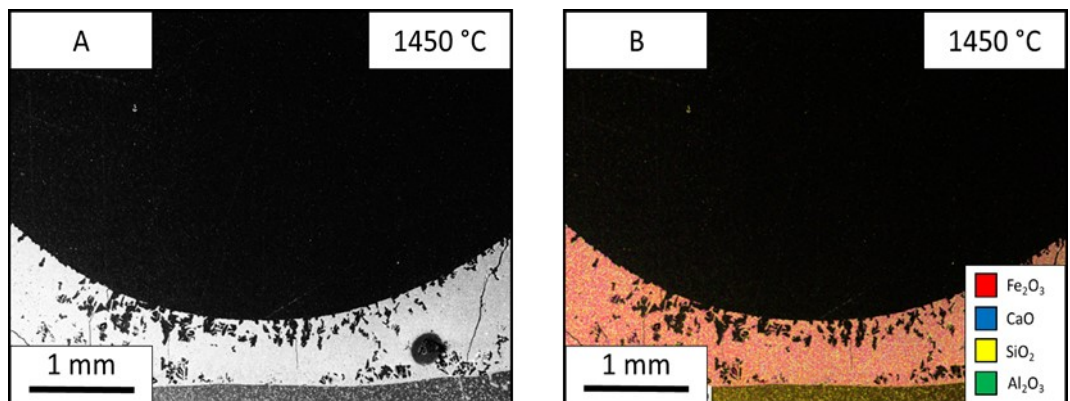
Figure 7-12: Images from the 1450 °C slag samples. A) electron image of the BOF slag sample, B) EDS map of the BOF slag electron image.

The SEM results from the slag sample are show in Figure 7-10A. The electron image shows that the iron ore (left) still displays similar properties to an unmolten sample, as there are small separated particles like that found in the lime sample. However, there is no linear reaction interface between the two phases as seen in the lime sample. At the interface, the sample appears as an exaggerated form of the limestone sample, with particles surrounded by reacting material (Figure 7-10B). In addition, the slag seems to be fully molten, which is to be expected due to its theoretical melting point, displaying a greater increase of iron content throughout the bulk phase compared to the other two fluxing materials.

The test was done at three different temperatures of 1350 °C (Figure 7-10), 1400 °C (Figure 7-11) and 1450 °C (Figure 7-12) and have a liquid fraction of 23 %, 34 % and 100 % respectively. In the 1350 °C slag, the sample shows that the iron ore can still be seen as individual particles however, they are suspended in a matrix of the slag. The slag itself is molten, however it seems to have no reaction with the iron ore despite flowing through the material. The 1450 °C sample shows that there is one homogeneous structure. The sample has been fully molten due to the meniscus shape of the sample.

7.4   Discussion

7.4.1   Fluxing material difference

By segmenting molten material from the SEM images and measuring the surface area fraction with image analysis software, the percentage of iron ore in molten state has been calculated for each material pairing. The lime and BOF slag have similar levels of molten iron ore at 1400 °C with results of 32 % and 34 % respectively, while limestone had a significantly higher result of 64 % liquid material.

Lime and BOF slag gained very similar liquid percentage however, the nature of the liquid fraction and its dispersion throughout the samples differ greatly. The lime-ore sample has a thick molten area at the interface connected to the lime. The BOF slag-ore sample shows no defined molten interface, as compared to that which was observed, in the lime-ore sample, and the molten section is spread throughout the iron ore in the sample. Furthermore, the lime in the sample is still solid and tightly packed whereas the BOF slag has fully melted into a continuous medium.

Due to the solid phase reaction between the lime and iron ore, the reaction has a defined reaction zone, which is limited by the size of the contact interface. The reaction can only progress through this liner interface and perpetuate through the dissolution of the materials into either side of this experimentally size determined

reaction interface. This reaction interface width would continue to grow in depth if the experiment was conducted for longer period, but the reaction area would remain approximately the same.

The BOF-iron ore slag sample has a different reaction path due to the lower melting of the fluxing agent. Being molten at experimental temperatures the material appears to have permeated through the iron ore matrix, resulting in an exponential growth of the liquid reaction interfacial area. Although at the time point these experiments were predetermined to stop at, the liquid fraction is similar between lime-ore and BOF slag-ore samples, the extensive mixing and more complex nature of the interface topology developed by the BOF slag-iron ore reaction preludes a higher interfacial area and faster interface development through the bulk phase.

The limestone sample outperformed both lime and BOF slag for liquid fraction development. The limestone follows similar conditions to the lime; however, it benefits from two key differences. The first is that limestone undergoes calcination at 900 °C to form the CaO actually utilised in the reaction, the calcination reaction is shown in equation (7.4) [47]. The literature has previously stated that limestone calcination results in newly formed CaO which has a higher reaction activity than aged lime in processes such as lime dissolution in slag [106]. Secondly the limestone used is of larger particle size than the lime, as such when a particle begins to flux the connectivity of the fluxing agent is effectively larger, allowing for wetting phenomena to surround or "drag" the material into the molten pool.

$$CaCO_3 + Heat \rightarrow CaO + CO_2 \tag{7.4}$$

Because of the sample size usable in the HT-CSLM, the actual effect of these materials on reduction kinetics is beyond the scope of this paper as there is not enough material for any quantitative analyses to be conducted. However, the mechanisms and influencing physical factors of three key metallurgical fluxing agents have been observed and discussed as to their expected effect on reduction. This work will be combined with larger bulk furnace trials and reductive environments in the near future, enabling a direct assessment on reduction performance under fluxing effects. From the above, limestone and BOF slag could both be considered potentially useful materials to add into gas reduction processes of iron ore. The higher order fluxing rate of limestone presents a key case for increasing liquid fraction. However, the permeation of liquid BOF slag through the bulk ore at the reaction temperatures presents a potentially exploitable fluxing pathway which will only be exacerbated by the large volume/bulk production facilities used in ironmaking (as opposed to the lime and limestone which develop a liquid reaction interface

purely on a pre-determined engineered interfacial area). Based on the shrinking core model the reduction mechanism of iron ore [63], [64] can be broken down into several stages including:

1. Mass transfer of reductive species in the gas phase

2. Diffusion of reaction species and products across the gas boundary layer

3. Diffusion of CO through the partially reduced ore particle

4. Reaction at the reduction frontier

5. Diffusion of CO_2 away from the reaction interface

To begin with, due to the ultra-high temperature of the system and the high Gibbs free energy, it is fair to assume that the reaction at the reduction frontier is unlikely to be reduction rate limiting. In addition the ultrasonic gas turbulence and abundant supply of reductive gas species leads the assumption that mass transfer in the gas phase is also non-rate limiting. This leaves diffusion through the gas boundary layer and transport of reduction reactants/products through the reduced layer of the ore particle as possible rate limiting steps.

Boundary layer diffusion can be qualitatively interrogated through calculation of the dimensionless Sherwood number expressed in equation 7.5. Using the same form as the Ranz-Marshall Correlation for heat transfer to a sphere, substitution of the Prandtl number for the Schmitt number (defined as the ratio of momentum diffusivity and mass diffusivity) (equation 7.6) gives an analogous form to appreciate the controlling factors on this variable with relation to other transport phenomena:

$$Sh = \frac{\text{Convective mass transfer rate}}{\text{Diffusion rate}} \tag{7.5}$$

$$Sh = 2 + 0.6Re^{\frac{1}{2}}Sc^{\frac{1}{3}}, 0 \leq Re < 200, 0 \leq Sc < 250 \tag{7.6}$$

Both the Reynolds and Schmitt numbers are calculated from variables including matter viscosity, density, diffusivity, distance, and velocity. The controlling factor for most of these variables is temperature, a process parameter that is more technologically defined/restricted in industrial reduction processes rather than scientifically targetable.

As a result, this leaves diffusion of reactants and products through the iron ore particles as the main way of influencing reduction kinetics. Fluxing/formation of a liquid phase within the process is likely to have two opposing contributions to this:

Formations of liquid/a continuous medium reduces surface area of the iron ore and thus increases the physical reaction pathway from the bulk gas to the unreacted material inside ore particles

Diffusion/transport kinetics are much faster in liquid phase than in solid, not only due to high diffusion coefficients but also convection stirring within the liquid medium.

7.4.2   Temperature

The temperature of the test has shown an increase of the liquid fraction in all three of the fluxing agents but to differing degrees of influence. The temperature has the effect of speeding up reactions and giving more energy to the reactants. This determined that the interaction is governed by the diffusion rates of the ore into the flux. If the reaction rate was controlled solely the size of the interface than there would be no difference as the temperature changes.

The lime samples show this by the sharp increase of fluid fraction between 1350 °C and 1400 °C from 16 % to 32 % and another increase at 1450 °C to 41 %. This is due to the diffusion rate increasing in line with the greater thermal energy within the system.

The limestone samples reacted more at the higher temperature with the highest temperature samples becoming molten. At the temperatures, 1350 °C and 1400 °C when compared to the CaO samples this can be explained by the higher liquid fraction created around the core of the shrinking core. This liquidus fraction material increases and intern speeds up the rate of interaction between the materials due to the diffusion transforming from solid to solid to liquid to solid thus generating a runaway effect on the rate of interaction.

The BOF slag sample suffers in terms of reaction rate due to the melting point of the slag being lower than the product of the iron ore and flux. This means that the liquid to solid interaction is reached at lower temperatures. In the highest temperature sample, the crucible shows a full meniscus showing a full homogeneous matrix of the ore and the slag combined. The lower temperatures have a molten slag and the solid matrix of iron ore. The temperature is important in this reaction to reach a critical phase reaction barrier to enable the process to take place. Once these boundaries are met the slag can be seen as a valid option as a fluxing reagent.

7.5 Conclusion

The mechanistic interactions between iron ore and three common metallurgical fluxing agents (CaO, CaCO$_3$ and BOF slag) have been observed in situ at temperatures of 1350, 1400 and 1450 °C and through ex-situ electron microscopy. The aim of the experiments was to begin to uncover the potential benefit that the co-injection of the reactants could provide to the reduction or pre-reduction of iron ore within the low carbon ironmaking technology HIsarna. In addition, the specific use of BOF slag offers a recycling and metallic content reclamation potential within an integrated steelworks improving overall yield.

Experimentally the fluxes can be ranked on liquid fraction formed over the same defined reaction period as limestone $>>$ slag $>$ lime. The limestone results show that newly formed CaO reactant species offer increased fluxing reaction kinetics.

Despite this, the use of a fluxing agent which is operating above its melting point (BOF slag) presents a technological advantage when scale up is considered for industrial application. Liquid fluxes will mix faster and more consistently with the ore, allowing for the formation of an overall larger reaction interface with greater growth potential throughout the bulk process.

Chapter 8

Investigation into the effect of Iron Ore Particle Composition on the Melting and Fluxing Behaviour with Calcium Oxide and Limestone

8.1 Motivation from the Work in Previous Chapters

The previous chapters investigated how iron ore and Ca based materials interact in bulk form. This was done at different temperatures and with three different Ca based materials: lime (CaO), limestone and Basic Oxygen Steelmaking slag (BOF slag). The results showed the progression of the interaction as a function of temperature. The outcomes help identify and instruct HIsarna in the potential benefits of using each ca-based material. The findings showed that the limestone as a Ca-based material worked better than both lime (CaO) and BOF slag.

During the experimentation, there was evidence of impurities in the ore causing issues in the interactions between the iron ore and Ca-based materials. As seen in Figure 6-3, a particle in the top of the image did not interact with the other materials. This image brings into question the effect of impurities in the ore, and how they can affect the interactions between iron ore and Ca based materials. As one of HIsarna's key features is its flexibility or materials used in the process, it is important to consider the influence of impurities on the process.

8.2   Introduction

Ironmaking as a process is massive in scale with 1869.9 million tonnes of crude steel being made in 2019 an increase of 3.4 % on 2018 [107]. When working to improve a process of this magnitude, small gains can affect efficiency or energy saving exponentially. The influences of impurities in the iron ore on the ironmaking process is thus an important aspect to understand for process efficiency.

HIsarna as a novel alternative ironmaking process needs to prove to the industry that it offers more benefits over that of the BF currently being used. This comes in many ways, and the most prevalent one is of course the environmental benefits it offers. However, there are additional advantages producers may be interested in from a production aspect. The key aspect of HIsarna for this study is its flexibility in materials which can be used, including non-sintered ore and different Ca-based materials. The fundamentals of material interaction and how different materials will change the way that the process works are key to enabling the deployment of claimed advantages. By studying the effects of impurities in iron ore, the interaction of material can be studied and if there needs to be additional consideration with regards to the use of the materials.

Iron ore is added to HIsarna differently to in the BF. In the BF, ore is added to the system at the top of the furnace straight into the shaft and makes its way down to the hearth [108]. This leads to the ore reacting in a bulk state with the other materials and gases in the process. In HIsarna the ore is injected into the CCF at high speed, into a turbulent environment [102]. This method of injecting or will cause a greater volume of micro/particle-to-particle reaction sites, compared to the bulk reaction usually found in the BF.

One drawback discovered from the pilot plant is the formation of accretions between the CCF and SRV, which is presented in Figure 6-3. In the image, it is clearly seen that the pathway is partially blocked between the SRV and CCF that obviously causes issues in operation. However, this pathway blockage has been reduced by the injection of Ca based material into the CCF. This accretion may be a product of the impurities in the ores causing issues with common occurrences such as a slag foaming and controlling the basicity of the slag.

Chapter 6 thoroughly examined the accretion sample taken from the HIsarna pilot plant trials and investigated various factors which may affect the formation of accretions. However, how accretions formed in the process is still not fully understood. There are theories and factors that have the potential to cause such material to build up to a problematic accretion. These include slag foaming, changes to slag

basicity and large amounts of stirring in SRV causing slag to splash into the CCF. All these can be affected by the addition of impurities added by the slag and ore hence the importance of understanding how impurities such as SiO_2, Al_2O_3 interact with iron oxide is key to deployment of the technology at scale in the future.

8.3 Results

8.3.1 HT-CSLM and Sessile drop In situ test

Figure 8-1 and Figure 8-2 show the interaction between an iron ore particle C-13 and CaO. At 1538.0 °C the particle begins to melt this is presented in the sessile image (Figure 8-2A) as a bulge at the contact point of the pellet is formed. Meanwhile, the confocal image (Figure 8-1A) no visible signs of melting. After 10 seconds at the temperature, the particle has continued to melt, and the bulge of the particle seen in the sessile image (Figure 8-2B) has increased. The confocal image (Figure 8-1B) now shows evidence of the melting with a bright bulge in the top right of the particle.

The particle continues to interact with another white spot appearing on the left of the particle and continuing the top left as seen in the 20s confocal picture (Figure 8-1C). The sessile image (Figure 8-2C) shows the particle increase the molten area at the bottom while the left-hand side had yet to come into contact with the pellet.

The phenomenon continues with and after 30s, the particle is now in full contact with the pellet seen in the sessile image (Figure 8-2D). This is evident with reference to the confocal image (Figure 8-1D) as now the entire circumference is in contact with the pellet, and the white patches that indicate molten material are more distinct around most of the particle.

After another 10s the sessile image (Figure 8-2E) shows the particle has become more droplet like, however the top surface is not smooth and still has evidence of some of the particle has yet to melt. Now with full contact with the pellet the confocal image (Figure 8-1E) the shape of the particle becomes more rounded at 40s.

At 50s, the particle has continued the trends already being observed. The sessile drop image (Figure 8-2F) shows that the particle now has full contact with the pellet and the height of the particle has decreased which indicates the continuation of the process. As already stated, the progression of the pellet in the confocal image (Figure 8-1F) is the smoothing of the boarders to a spherical shape which is seen it at the 50s point.

At the completion of the experiment seen in the 60s images the particle has shrunk in height further (Figure 8-2G) than that of the 50s sessile image (Figure

8-2F) and has a smoother top showing the particle is molten. As seen the confocal image (Figure 8-1G) show the particle is even more spherical in shape with smoother boarder denoting a more molten particle.

Figure 8-1: A Series of images taken from the HT-CSLM of particle C-13 and show an example of the particles process while interacting with the CaO. A) Particle at 0 s. B) particle at 10 s. C) Particle at 20 s. D) particle at 30 s. E) particle at 40 s. F) Particle at 50 s. G) Particle at 60 s.
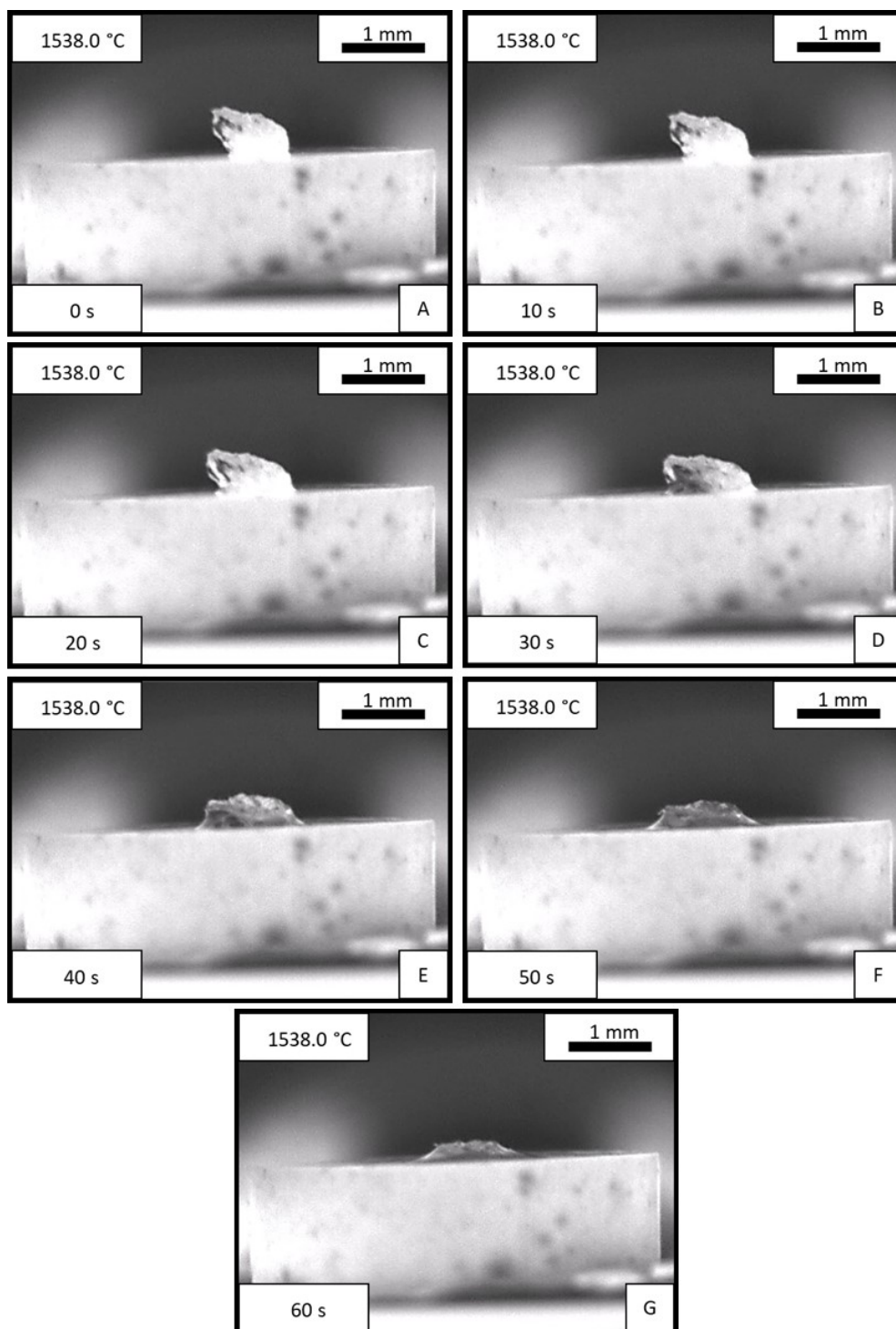
Figure 8-2: A Series of images taken from the SDC of particle C-13 and show an example of the particles process while interacting with the CaO. A) Particle at 0 s. B) particle at 10 s. C) Particle at 20 s. D) particle at 30 s. E) particle at 40 s. F) Particle at 50 s. G) Particle at 60 s.

Figure 8-3 and Figure 8-4 shows the progression of the reaction between an iron ore particle and the limestone pellet. The sequence of images shows the reaction in 10 seconds intervals to give full visual example of the reaction between the iron ore particle and the limestone pellet. The temperature that these images are taken is 1249.0 °C and the sample shown is labelled L-10.

At 0 seconds of 1249.0 °C, the confocal image (Figure 8-3A) of iron ore particle has a roof outline with white speckles in the centre of the particle. These white speckles are the rough surface of the solid particle that the laser microscope has focused on. In the sessile drop image (Figure 8-4A), the particle seen would be at room temperature with a similar rough exterior and no signs of any molten phase.

After 10 seconds of the reaction, the confocal image (Figure 8-3B) that the particle has become more spherical than that at 0 seconds, the white speckles scene at 0 seconds have also moved suggesting the particle has moved. Both occurrences suggest that a molten interface between the particle and the pellet has formed causing the movement of the particle and growth in this confocal image. The sessile image (Figure 8-4B) shows that the particle seems to have rotated anticlockwise slightly and at the contact area of pellet and particle shows evidence of a molten phase by evidence of wetting.

At 20 seconds into the reaction, the confocal image (Figure 8-3C) that the particle has grown, and the white spots have now moved to the centre of the particle, suggesting this is the highest point of the particle. The more rounded outline of the particle and subsequent growth suggest the molten area is spreading. The sessile drop image (Figure 8-4C) shows the particle looking like a mountain in shape with a peak at the centre where the white spots would be present in the confocal image and the lower section of the particle it is starting to take the shape of a droplet on a substrate.

After 30 seconds into the reaction, the confocal image (Figure 8-3D) shows the white spots to be gathering in the centre of the particle in greater numbers and the outline of the particle has grown again and is beginning to take a smoother shape. The sessile drop photo (Figure 8-4D) is like the 20 second image (Figure 8-4C), however, the left-hand side of the droplet described is smoother than in the previous image and the peak is slightly more prevalent.

After 40 seconds into the reaction and now at the centre of the confocal image (Figure 8-3E) the small white spots have coalesced into a larger white spot. This is due to the confocal focusing on the top of the droplet and the molten phase is seen. The small white spots around the centre spot show that there are still a solid phase floating on the molten one. The outer area of the particle has grown

again but still does not have a smooth circumference as evidenced in the bottom right of the image. In the sessile image (Figure 8-4E), the particle is now like a droplet on a substrate, however, at the top of the droplet that seems to be a small circular area floating on top that is solid.

After 50 seconds into the reaction, the circumference of the particle has now become more circular as seen in the confocal image (Figure 8-3F) but is a similar size of the last image at 40 seconds (Figure 8-3E). Large white circle, which shows the top of the droplet, has grown; however, there is a dark spot in the centre that suggests a small amount of solid material still present in the particle. The sessile drop image (Figure 8-4F) now shows what seems to be a molten droplet on top of the pellet with no evidence of any solid material.

In the final image taken at 60 seconds, a similar image in the confocal (Figure 8-3G) as the 50-second image with the white spot having some solid material floating on top. The circumference is a similar size and shape to the last image. The sessile image (Figure 8-4G) is also as the previous 50 seconds image (Figure 8-4F) with a fully molten, drops are visible on top of the pellet.
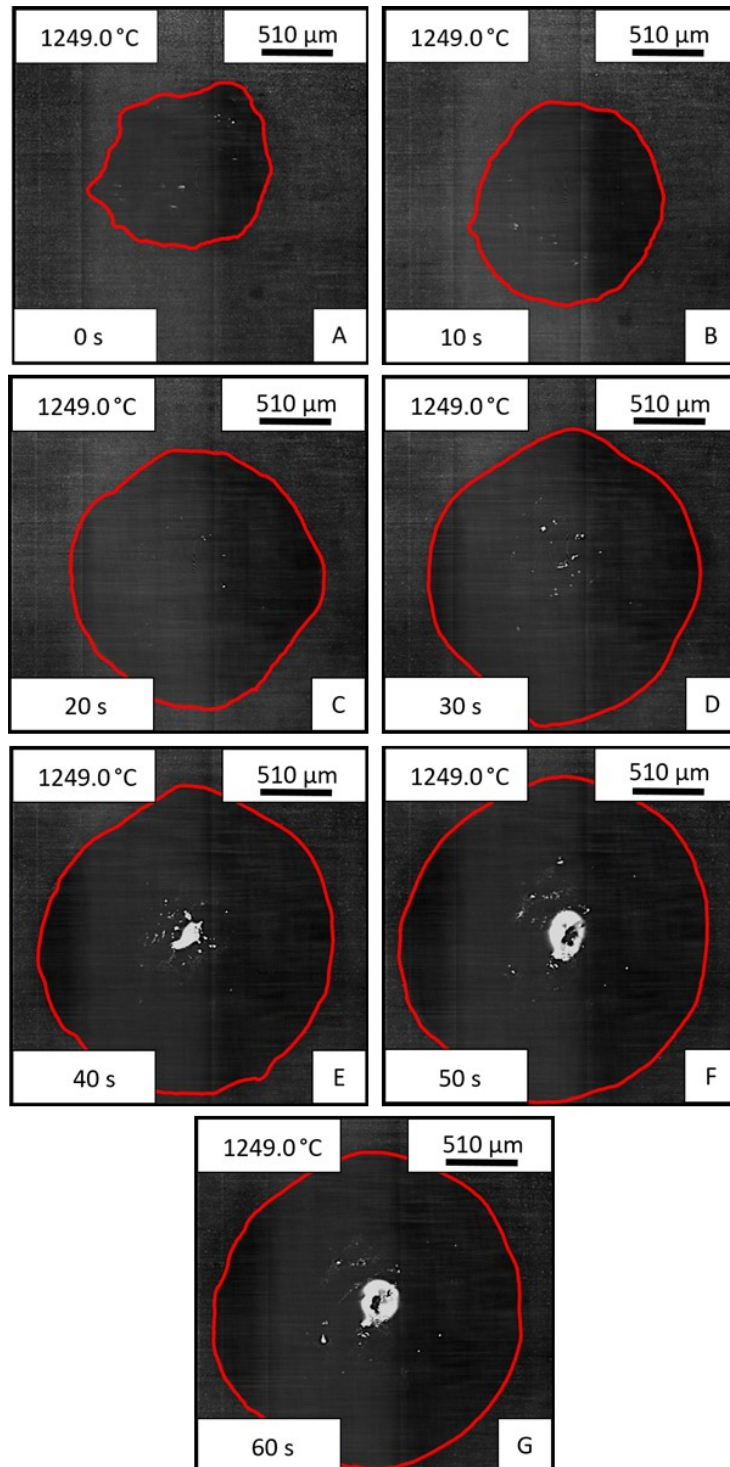
Figure 8-3: A Series of images taken from the HT-CSLM of particle L-10 and show an example of the particles process while interacting with the limestone. A) Particle at 0 s. B) particle at 10 s. C) Particle at 20 s. D) particle at 30 s. E) particle at 40 s. F) Particle at 50 s. G) Particle at 60 s.
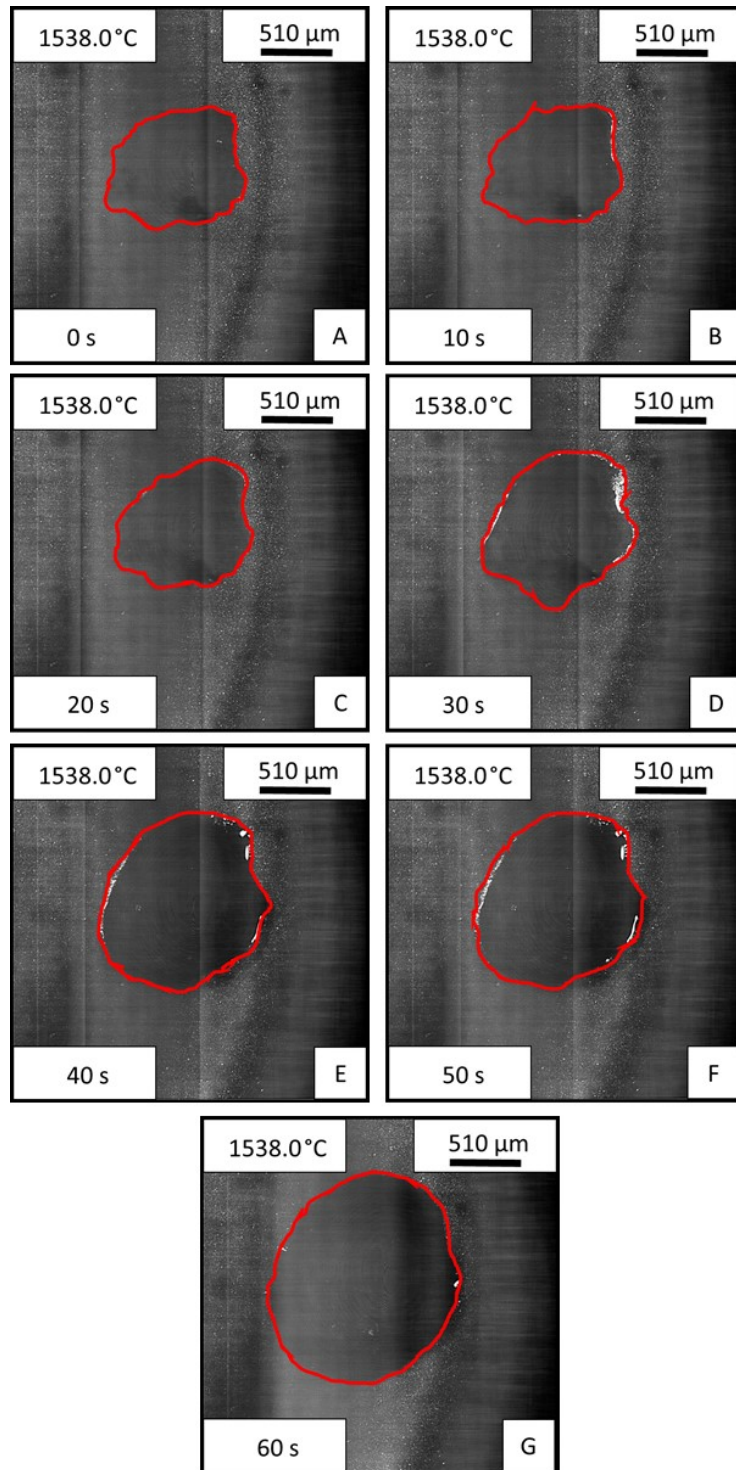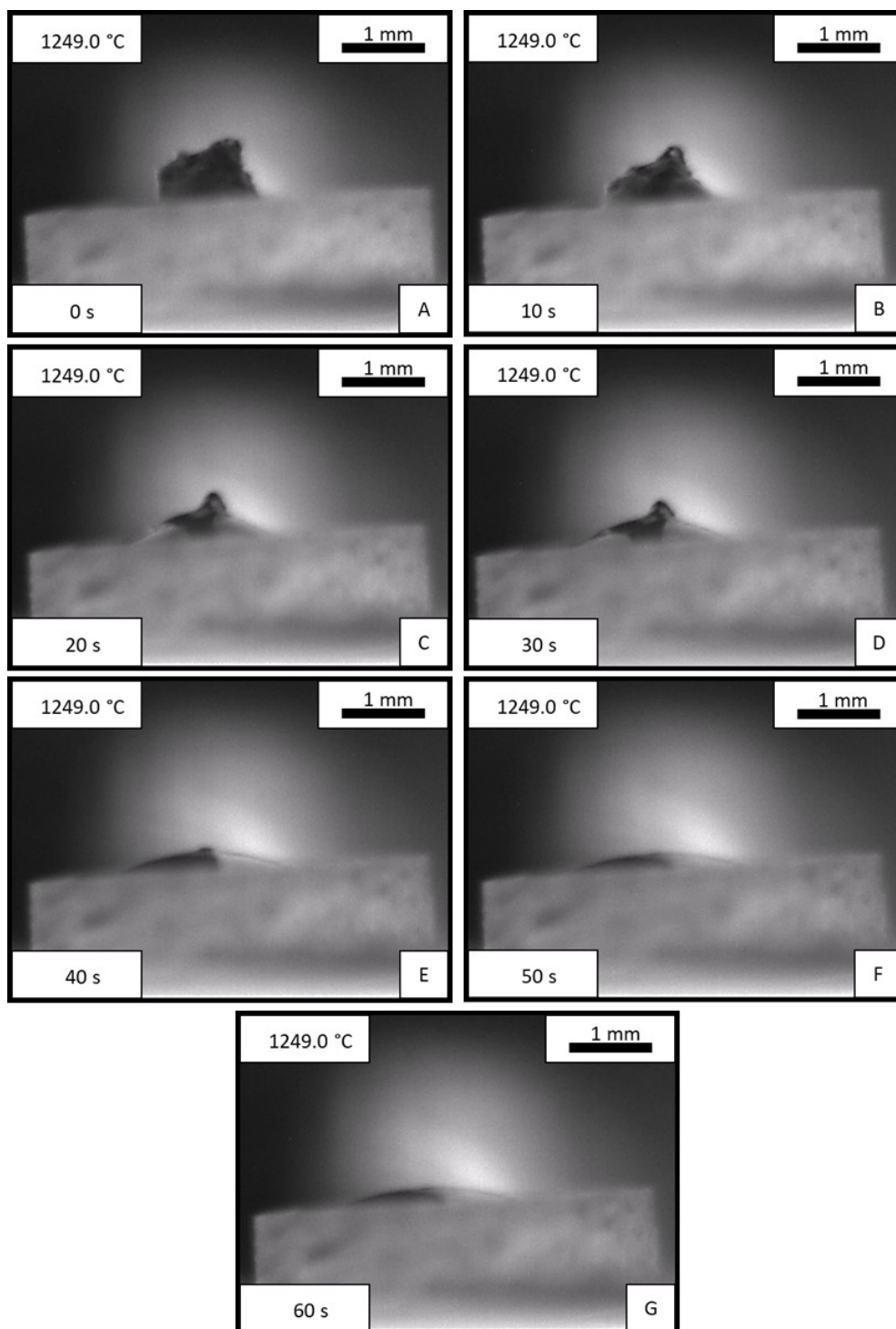
Figure 8-4: A Series of images taken from the SDC of particle L 10 and show an example of the particles process while interacting with the limestone. A) Particle at 0 s. B) particle at 10 s. C) Particle at 20 s. D) particle at 30 s. E) particle at 40 s. F) Particle at 50 s. G) Particle at 60 s.

8.3.2 Experimental melting points

The HT-CSLM can determine the melting point of the particle with visualisation as seen in Figure 8-1 to Figure 8-4. The results of the iron ore particles used with lime (CaO) pellets is presented in Table 8-1 and the results of the iron ore particles used in reaction with limestone pellets can be found in Table 8-2.

Table 8-1: The melting points of the experimental melting points obtained through the HT-CSLM for all samples reacted with CaO.

Sample	Fe_2O_3	SiO_2	CaO	Al_2O_3	K_2O	MgO	Experimental m.p (°C)
C-1	45.8	29.4	4.6	17.2	0.3	2.8	1172 °C
C-2	97.4	1.1	0.3	0.9	0.1	0.3	1239 °C
C-3	96.3	1.3	0.4	1.7	0.2	0.2	1253 °C
C-4	93.4	5.2	0.1	1.0	0.1	0.2	1257 °C
C-5	99.2	0.2	0.1	0.5	0.0	0.1	1262 °C
C-6	98.0	0.6	0.2	0.8	0.1	0.2	1263 °C
C-7	75.8	7.6	1.8	8.3	2.4	4.1	1269 °C
C-8	50.8	28.4	2.1	13.1	3.7	2.0	1272 °C
C-9	71.3	8.7	4.4	10.6	1.3	3.7	1288 °C
C-10	46.0	29.4	0.1	15.0	1.2	8.3	1309 °C
C-11	82.0	6.0	0.1	6.6	2.6	2.7	1355 °C
C-12	47.8	48.4	0.4	1.9	0.6	0.9	1443 °C
C-13	6.8	90.7	0.5	1.3	0.4	0.3	1538 °C

Table 8-2: The melting points of the experimental melting points obtained through the HT-CSLM for all samples reacted with limestone.

Sample	Fe_2O_3	SiO_2	CaO	Al_2O_3	K_2O	MgO	Experimental m.p (°C)
L-1	97.2	0.8	0.1	1.7	0.1	0.2	1164 °C
L-2	96.9	1.1	0.1	1.2	0.2	0.4	1170 °C
L-3	75.1	7.5	6.9	6.3	1.5	2.8	1172 °C
L-4	97.1	0.8	0.5	1.1	0.2	0.2	1173 °C
L-5	95.1	1.8	0.5	1.9	0.4	0.2	1184 °C
L-6	76.7	9.5	0.6	8.9	0.7	3.5	1193 °C
L-7	92.3	2.6	0.7	3.4	0.4	0.7	1205 °C
L-8	48.4	20.3	16.5	2.6	0.4	11.9	1207 °C
L-9	50.5	31.9	2.2	12.7	1.0	1.6	1228 °C
L-10	23.3	31.8	3.3	32.2	7.3	2.1	1249 °C
L-11	23.2	74.6	0.4	1.2	0.2	0.4	1379 °C
L-12	28.1	70.4	0.2	0.8	0.2	0.2	1409 °C

The results of the particles reacted with CaO in the experiment with the corresponding compositions found in Table 8-1. The results show that the sample with the lowest experimental melting point was C-1 with a melting point of 1172 °C, while sample C-13 had the highest melting point of 1538 °C.

Table 8-2 and the corresponding compositions of the iron ore particles used. The experimental result shows that the lowest melting point observed was L-1 with a melting point of 1164 °C and the highest melting point was sample L-12 with a melting point of 1409 °C.

8.3.3   Comparison of Particles

Each particle has different compositions even though all the particles come from the same iron ore. The average temperature gives a good indication of the improved activation of limestone. However, with the compositions of each particle assessed before the experimentation, the composition of the particles can be compared and scrutinised, by looking at particles with similar chemistries.

In the experiment, there were three pairs of particles with similar compositions. Each pair had one sample reacted with a CaO pellet and one sample reacted with a limestone pellet. These pairs are C-6 and L-4, C-3 and L-5, and C-2 and L-2, and their compositions can be found in Table 8-3.

Table 8-3: The three pairs of samples with their compositions and experimental melting point of each.

Sample	Fe_2O_3	SiO_2	CaO	Al_2O_3	K_2O	MgO	Experimental m.p (°C)
C-6	98.0	0.6	0.2	0.8	0.1	0.2	1263 °C
L-4	97.1	0.8	0.5	1.1	0.2	0.2	1173 °C
C-3	96.3	1.3	0.4	1.7	0.2	0.2	1253 °C
L-5	95.1	1.8	0.5	1.9	0.4	0.2	1184 °C
C-2	97.4	1.1	0.3	0.9	0.1	0.3	1239 °C
L-2	96.9	1.1	0.1	1.2	0.2	0.4	1170 °C

In the first, pair of particles, C-6, and L-4 all the compounds apart from Fe_2O_3 are within 0.3 % of each other while the iron is 0.9 % difference. The second pair C-3 and L-5 are within 0.5 % concerning each compound; however, the Fe_2O_3 has a larger difference of 1.2 % between the two samples. The Third pair C-2 and L-2 have most the compounds within 0.3 % with the Fe_2O_3 compound having a 0.5 % difference. All the samples have a high Fe_2O_3 content over 95 %.

The temperatures of melting for these pairs all show that the limestone sam-

ples had a lower melting point than that of the CaO samples. With the difference in temperature being 90 °C between C-6 and L-4, 69 °C between C-3 and L-5 and 69 °C between C-2 and L-2.

8.3.4 Measurement of the Particles

From the in situ visualisation of how the particles react with the CaO and limestone as shown in Figure 8-1 to Figure 8-4, and the progression of the reaction between iron ore particles and Ca-based materials. Using these images from both the HT-CSLM and the SDR, the particle size can be measured as it melts to determine the reaction rate of a particle. From the HT-CSLM, the Y-axis, X-axis and Z-axis area of the particle can be measured and the SDC the Z-axis, contact size, Y-plane area and droplet angle. A schematic of the measurements in Figure 5-7.

From the matrix of experiments, eight particles were measured using the video clips from the HT-CSLM and SDC recordings. Four of the selected particles reacted with a CaO pellet and the other four selected particles reacted with limestone. These particles are found in Table 8-4 with the particle size before the reaction with the pellets.

Table 8-4: Table of the particles measured in the kinetic study with the experimental melting point and the size of the particles measure at t_0.

Sample	Temperature (°C)	HT-CSLM			SDC			
		Y-axis (μm)	X-axis (μm)	Z-plane (μm^2)	Contact (μm)	Z-axis (μm)	Y-plane (μm^2)	Angle
C-2	1239	1013.4	1039.4	859535.7	722.8	471.5	341070.3	52.0
C-8	1272	1180.9	1039.4	1032787.7	1092.7	646.2	852682.6	48.9
C-11	1355	1493.0	1024.6	1504792.6	1287.0	682.4	910856.9	46.3
C-13	1538	829.3	946.5	703180.4	677.9	499.0	378036.7	51.1
L-2	1170	939.3	969.0	711685.1	922.4	162.7	144104.7	20.6
L-5	1184	1129.3	1153.9	907315.5	855.3	902.1	727928.4	53.8
L-8	1208	1342.8	654.2	742243.2	1010.4	669.1	754658.5	47.4
L-10	1249	1160.5	1199.8	1180509.6	1146.8	560.6	651906.4	42.4

8.4 Discussion

8.4.1 Limestone increased performance

As found in the previous chapter, limestone out preformed both pure CaO and BOF slag by looking at small-scale bulk on bulk materials in the HT-CSLM. Performance was discerned by looking at how the interactions changed the morphology after the high temperature interaction and the melting of the interface from the in situ visualisation.

The HT-CSLM and SDC method added more evidence of the performance of limestone against the pure CaO as the same interactions would happen but on a single iron ore particle. This suggestion builds on the work from Chapter 7 with reactions with limestone and the ideas from Glasson [106] and Valverde et al [109] put forward in limestones reactivity. The method was unable to compare these against the BOF slag as the BOF slag (or part of the BOF slag) has a lower melting point than that of the iron ore. Hence, a pellet would not maintain solid phase at the temperatures required for this experiment. This would make the SDC image not suitable for analysis and be inconclusive meaning that only limestone and pure CaO can be compared. In addition, there would be a high chance of damaging the equipment with falling molten material.

From the 25 samples of particles of iron ore tested against the two Ca based materials it was found that on average the limestone samples melted at lower temperatures than that of the CaO samples. This is seen as the average melting point of the CaO particle samples was measured at 1301.53 °C while the limestone samples had an average of 1227.75 °C.

Although the compositions of the particles used in each experiment are not the same, by comparing the particles with similar compositions like the three pairs found in Table 8-3. Each pair showed that the limestone particle lowered the melting point of the particle more than the pure CaO samples. The highest change is 90 °C between the C 6 and L-4 and the other two particle pairs are both 69 °C. As the material in the pellet is the only difference, the limestone influences the melting point.

These findings further support those found in the previous chapter and that the formation of newly formed CaO through calcination is more reactive than that of pure CaO.

8.4.2 The effect Fe_2O_3, SiO_2 and CaO on the melting behaviour of the particles

The bulk iron ore used in this experiment, as seen in Table 4-1, has the two main components Fe_2O_3 and SiO_2 with compositions of 66.26 wt. % and 6.75 wt. %, respectively. This is also seen in the particle compositions found in Table 8-1 and Table 8-2, where Fe_2O_3 and SiO_2 had the two highest wt. % of most particles taken from the bulk material. The Fe_2O_3 wt. % ranges from 6.8 wt. % to 99.2 wt. % while the SiO_2 wt. % ranged from 0.2 wt. % to 90.7 wt. %. The other main components are CaO, which is the reactant in the form of lime (pure CaO), and limestone, which forms CaO via $CaCO_3$ calcination. The two other complexes (Al_2O_3 and MgO) also play important roles in the interaction. Their amount in the bulk material and most particles is on the scale of being an included residual than a significant impurity. However, they play an important role and will be discussed later in this chapter.

To understand the basic interactions, the system can be simplified from the six components to the three most common ones. This simplified interaction means the tertiary phase diagram between Fe_2O_3, SiO_2 and CaO can be studied to see how a system containing these three compound will react [110]. The phase diagrams presented in Figure 8-5 and shows the thermodynamic properties of these materials at different compositions studied to understand the melting behaviour and how each changes the melting properties of the system.
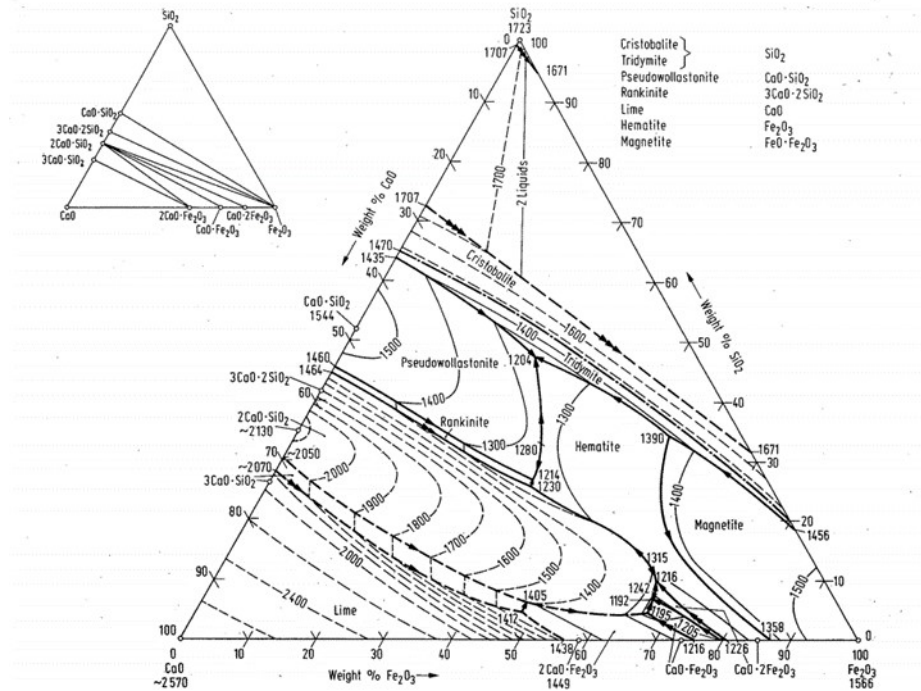
Figure 8-5: Phase diagram of Fe_2O_3, CaO and SiO_2. [110]

8.4.2.1 Fe_2O_3 Content

Fe_2O_3 is the highest composition in the iron ore and on its own has a melting point of 1596 °C; however, with mixing with either CaO or SiO_2 the melting point can be lowered. The two binary phase diagrams of FeO_x – SiO_2 and FeO_x – CaO show that a similar amount of either CaO or SiO_2 can causes a eutectic point in both systems this being 20 wt. % of CaO and 18 wt. % of SiO_2. The temperature of these two eutectic points are significantly different where in the FeO_x - CaO system the eutectic temperature is 1205 °C [61]. While the eutectic temperature of the FeO_x - SiO_2 system is 1455 °C [111]. This means that CaO effects the melting temperature of iron more than SiO_2. In the tertiary phase diagram (Figure 8-5) the lowest melting point is at 1192 °C with a composition of 68 wt. % Fe_2O_3, 6 wt. % SiO_2 and 26 wt. % CaO. This also shows that the increasing iron in the system decreases the melting point of a high CaO – SiO_2 system as the boundaries lower with increasing Fe_2O_3. This is shown in Figure 8-6 and Figure 8-7 the result of the experimentation with the particles with both materials showing the melting point and its Fe_2O_3 wt. %. The experiment shows the particles with the higher Fe_2O_3 content have a lower melting point however the temperature does not increase until the Fe_2O_3 decreases below 30 wt. %.

110
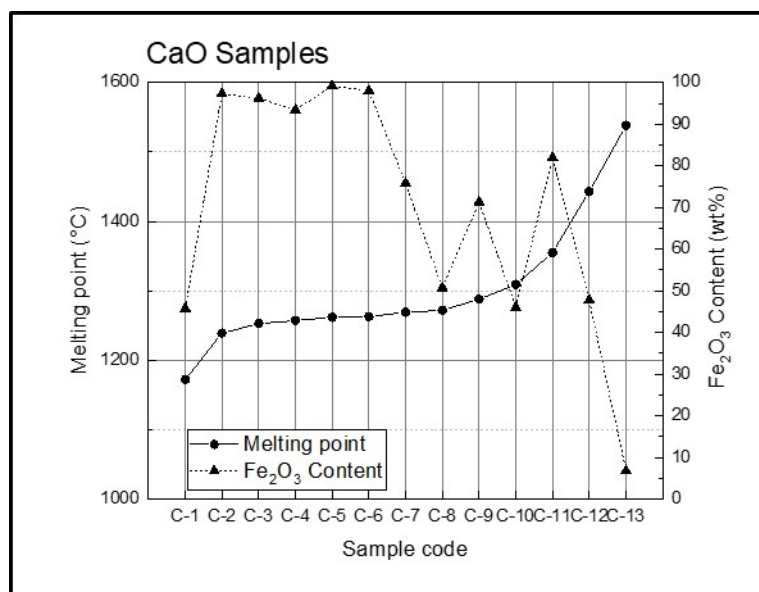
Figure 8-6: Fe$_2$O$_3$ content of samples and its measured experimental melting point of all CaO samples.
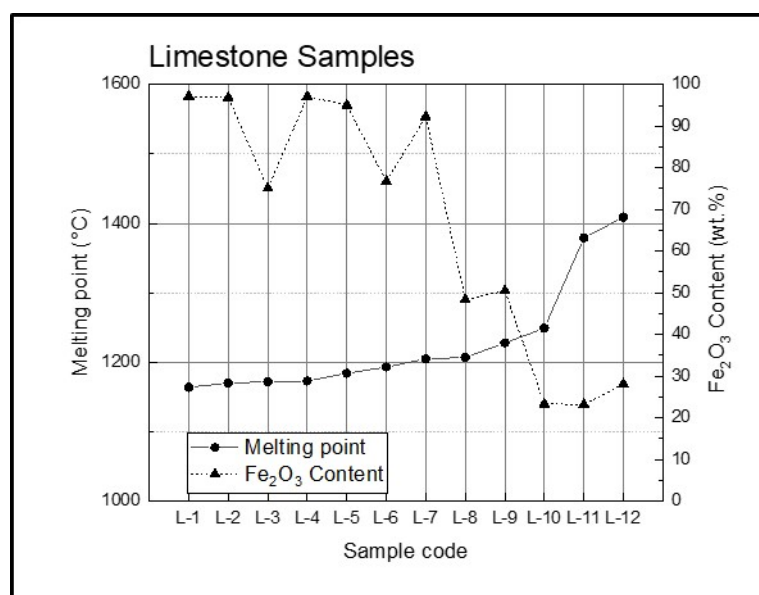
Figure 8-7: Fe$_2$O$_3$ content of samples and its measured experimental melting point of all limestone samples.

8.4.2.2 SiO$_2$ Content

In the iron ore used in the experiment, one of the biggest impurities found was silica with 6.75 wt. % of the bulk iron ores composition. However, comparing the com-

position of the bulk ore and the individual particles the silica content varied from each composition gained. The SiO_2 content ranged from 0.2 wt. % to 90.7 wt. % and this variation from particle to particle means that some feeds may have a higher SiO_2 content than expected. Understanding the role SiO_2 has on the reaction between CaO and iron ore in terms of the melting of the ore. Understanding the phenomenon will help control the material in the process better and control the properties beneficial for the process.

In Figure 8-8 and Figure 8-9, the results of the experiment are shown and the SiO_2 content of the particles and its measured melting point. They show that when reacted with the CaO based material the content of SiO_2 in the particle has little effect on the melting point until the SiO_2 value is higher than 40 %. Once this threshold is reached, the melting point of the particle in the reaction drastically increases.
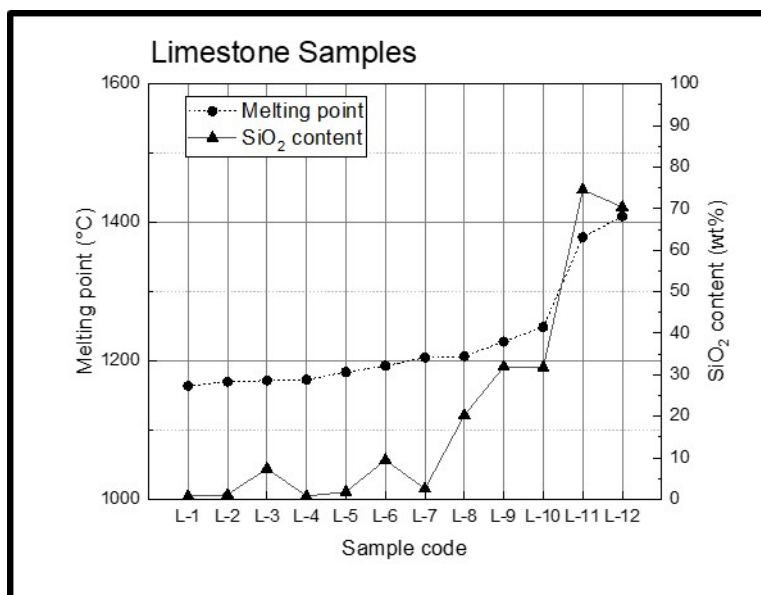
Figure 8-8: SiO_2 content of samples and its measured experimental melting point of all CaO samples.
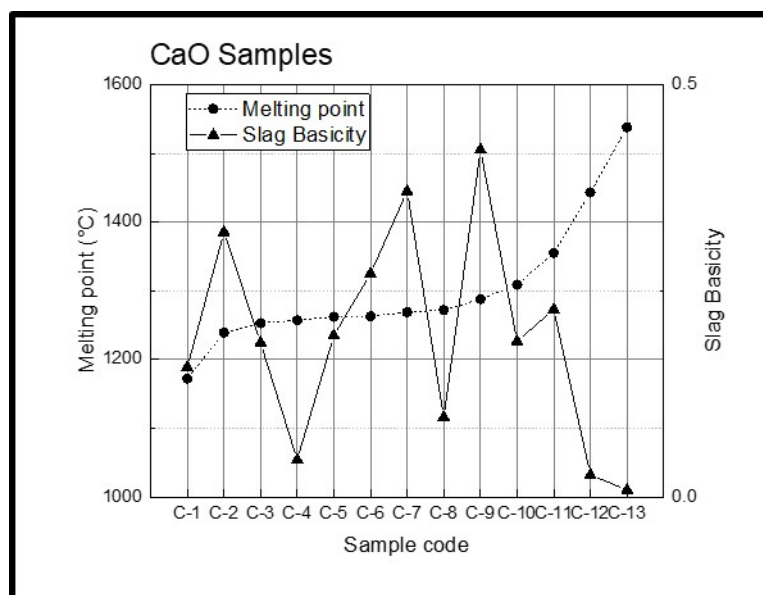
Figure 8-9: SiO$_2$ content of samples and its measured experimental melting point of all limestone samples.

The ternary phase diagram as seen in Figure 8-5 shows that with the increased amount of SiO$_2$ in the system the melting point becomes as high as 1700 °C. The first line from the top of the diagram runs from 28 wt. % CaO to 32 wt. % SiO$_2$ with temperatures running from 1671 °C to 1707 °C. This shows that particles with the higher SiO$_2$ content have a higher temperature. Also, by considering the two-complex system of SiO$_2$ and CaO the eutectic point is with 63 wt. % SiO$_2$ at 1436 °C. There is another point with a similar eutectic point at 1460 °C this is with 55 wt. % SiO$_2$ [112]. This shows that more CaO is needed in the system to melt pure SiO$_2$ than that needed with the Fe$_2$O$_3$.

8.4.2.3 CaO Content

CaO is the reactant in both the above experiments in its "pure" form as lime or formed from the calcination of limestone (CaCO$_3$). The amount of the CaO needed to melt the system will change depending on the other materials in the particle. To show the effect of the addition of the CaO, the melting point of each particle was calculated using FactSage^{TM}. This shows how the different levels of CaO affecting melting; hence, the calculations were done with additions of 5 wt. %, 10 wt. %, 15 wt. % and 20 wt. % of CaO this is due to the how 20 wt. % CaO corresponds to the phase diagram in Figure 2-13. The results in Table 8-5 give the melting points for the iron ore particles reacted with CaO and Table 8-6 for the particles

reacted with limestone.

Table 8-5: All particles reacted with CaO with experimental melting point and theoretical melting point calculated from FactSage^{TM} of different levels of CaO reacted with each particle

Sample	Exp m.p (°C)	Theoretical Calculated melting point (°C)				
		0 % CaO	5 % CaO	10 % CaO	15 % CaO	20 % CaO
C-1	1172	1528	1519	1492	1449	1390
C-2	1239	1665	1500	1405	1325	1216
C-3	1253	1664	1596	1500	1375	1230
C-4	1257	1646	1608	1537	1436	1308
C-5	1262	1682	1610	1515	1394	1254
C-6	1263	1673	1604	1507	1387	1244
C-7	1269	1595	1570	1539	1494	1434
C-8	1272	1573	1542	1504	1447	1381
C-9	1288	1555	1552	1501	1459	1400
C-10	1309	1555	1545	1525	1523	1512
C-11	1355	1616	1537	1486	1441	1383
C-12	1443	1542	1538	1497	1447	1396
C-13	1538	1641	1655	1657	1662	1666

Table 8-6: All particles reacted with Limestone and there experimental melting point and theoretical melting point calculated in FactSage^{TM} of different levels of CaO reacted with each particle.

Sample	Exp mp (°C)	Theoretical Calculated melting point (°C)				
		0 % CaO	5 % CaO	10 % CaO	15 % CaO	20 % CaO
L-1	1164	1673	1602	1503	1376	1231
L-2	1170	1663	1597	1405	1381	1212
L-3	1172	1520	1489	1451	1402	1337
L-4	1173	1665	1594	1497	1372	1228
L-5	1184	1656	1589	1464	1369	1222
L-6	1193	1585	1531	1507	1476	1431
L-7	1205	1645	1576	1475	1343	1259
L-8	1207	1622	1606	1580	1537	1501
L-9	1228	1538	1530	1507	1469	1420
L-10	1249	1550	1498	1465	1427	1389
L-11	1379	1650	1646	1640	1581	1448
L-12	1409	1654	1699	1628	1523	1371

The theoretically calculated melting point of the particle at 0 wt. % added CaO and the experimental melting point observed are drastically different. This difference continues as when the wt. % of CaO is increased in the system, the melting

temperature drops for most particles. However, the theoretical melting points of the particles with 20 % CaO does not match the ones observed experimentally. This suggest that the experiment continued past these values to reach a CaO % that met the eutectic point of the experiment. Particle C-13 is the best example of this as the addition of CaO increased the melting point from 1641 °C to 1666 °C while the experimental melting point was determined to be 1538 °C.

To determine the amount of CaO needed to reach the observed melting points from the experiment the Fe_2O_3-SiO_2-CaO phase diagram was used. The particles needed to be changed to a pure Fe_2O_3/SiO_2 meaning the other components were removed to get a percentage of Fe_2O_3 and SiO_2. Using the phase diagram, a line is drawn that corresponds to the addition of CaO with a constant ratio of Fe_2O_3 and SiO_2. The line was used to find the eutectic point and its corresponding CaO %. This CaO % was then used against the particles to see how this compared to the experimental melting point and the results is presented in Table 8-7 and Table 8-8.

Table 8-7: All particles reacted with CaO with the eutectic point gained from the phase diagram and the calculated amount of CaO needed to reach lowest eutectic temperature from FactSage^{TM}.

Sample	Binary Phase Particle			Phase Diagram Eutectic		Calculation of Particle with CaO % (°C)	Exp m.p (°C)
	Sum of Fe_2O_3 and SiO_2 (%)	Fe_2O_3 (%)	SiO_2 (%)	Eutectic CaO (%)	Eutectic Temperature (°C)		
C-1	75.2	61	39	35	1291	1423	1172
C-2	98.4	99	1	21	1247	1221	1239
C-3	97.5	99	1	21	1247	1211	1253
C-4	98.6	95	5	28	1339	1349	1257
C-5	99.4	100	0	20	1205	1254	1262
C-6	98.7	99	1	21	1247	1223	1263
C-7	83.4	91	9	27	1314	1352	1269
C-8	79.1	64	36	34	1310	1360	1272
C-9	80.0	89	11	27	1289	1387	1288
C-10	75.4	61	39	35	1291	1429	1309
C-11	88.0	93	7	24	1261	1341	1355
C-12	96.2	50	50	40	1304	1287	1443
C-13	97.5	7	93	34	1428	1435	1538

Table 8-8: All particles reacted with limestone with the eutectic point gained from the phase diagram and the calculated amount of CaO needed to reach lowest eutectic temperature from FactSage$^{\text{TM}}$.

Sample	Binary Phase Particle			Phase Diagram Eutectic		Calculation of Particle with CaO % (°C)	Exp m.p (°C)
	Sum of Fe$_2$O$_3$ and SiO$_2$ (%)	Fe$_2$O$_3$ (%)	SiO$_2$ (%)	Eutectic CaO (%)	Eutectic Temperature (°C)		
L-1	97.9	99 %	1 %	21	1247	1214	1164
L-2	98.0	99 %	1 %	21	1247	1216	1170
L-3	82.5	91 %	9 %	27	1314	1417	1172
L-4	97.9	99 %	1 %	21	1247	1216	1173
L-5	96.9	98 %	2 %	21	1264	1213	1184
L-6	86.2	89 %	11 %	27	1289	1431	1193
L-7	94.9	97 %	3 %	22	1272	1275	1205
L-8	68.7	70 %	30 %	30	1340	1701	1207
L-9	82.5	61 %	39 %	35	1291	1394	1228
L-10	55.1	42 %	58 %	44	1345	1419	1249
L-11	97.7	24 %	76 %	49	1413	1407	1379
L-12	98.5	29 %	71 %	47	1389	1387	1409

For most of the particles with a combined Fe$_2$O$_3$ and SiO$_2$ over 90 % the theoretical melting point is within 50 °C of the experimentally measured temperature. However, two particles do not fit this trend, C-12, and C-13. These have the highest melting point and the highest SiO$_2$ content of the samples reacted with the lime. These factors mean that a high percentage of CaO is needed to reach this eutectic point, which are 40 wt. % and 34 wt. % respectively. The high amount of CaO needed for the eutectic to be met means more diffusion into the particle. As the heating in the confocal was set to a steady rate, the required CaO could be reached after the temperature boundary has been met. This would lead to a higher melting point being recorded, as the kinetics of the reaction could not match the heating rate. The limestone samples have similar high CaO needed to meet the eutectic point; however, limestone has been shown to increase the reaction speed of the system [106].

Sample L-8 also shows a very high-calculated melting point from FactSage$^{\text{TM}}$ of 1701 °C while the experimental was 1207 °C. The sum of the Fe$_2$O$_3$ and the SiO$_2$ was 68.7 wt. % of the particle. This means the other 37.3 % are the other materials in the particle (CaO, Al$_2$O$_3$ and MgO). In this particle, the amount of CaO was high as the particle already contains 16.5 wt. % CaO. Therefore, in the calculation with all the compositions of the particle with extra CaO gained from the three-phase system the calculation had 46.5 wt. % CaO which would increase the temperature away from any eutectic.

8.4.2.4   Al$_2$O$_3$ and MgO

The Fe$_2$O$_3$, SiO$_2$ and CaO system has been studied in detail because the particles used in the study have a composition of mostly Fe$_2$O$_3$ and SiO$_2$ which is being

reacted with Ca based fluxes. The other particles that do not follow these trends must be affected by the other components in the particle such as Al_2O_3 and MgO. These components are known for changing slag chemistry in different ways. Al_2O_3 is known to increases the slag viscosity making it less fluid and MgO can be added to control the effect of the Al_2O_3 to decrease the viscosity of the slag and increase the fluidity [113], [114]. These are important factors in determining the interactions occurring in the experiment.

As a slag acts as a non-Newtonian fluid, it is affected by shear rate which can be either shear thinning or shear thickening. At high temperature where the material is liquid the structural is more disordered with $[AlO_4]^{5-}$ making the Al-O bonds unconstrained to a direction. The implementation of shear stress on the material will align these bonds along the direction of the force lowering the viscosity. However, at lower temperatures are some solid crystal precipitating in the melt and grow on cooling. With significant precipitation of crystals the viscosity can drastically increase with shear stress due to the shear thinning effect on a non-Newtonian fluid [115]. These are important factors in determining the interactions occurring in the experiment by looking at how Al_2O_3 and MgO effect the melt to see how these factors affect the viscosity of the iron ore in the CCF.

The experiment showed these compounds effect the melting point of the systems being studied but their influence is dependent on the ratio of the two. From FactSage^{TM} the complexes that are being formed can be determined and thus determine which are hindering the low melting points that can be achieved in simpler systems. Al_2O_3 and MgO are in the form of corundum [116] and an Al/Mg spinel [117].

In particle C-8, the Al_2O_3/MgO ratio favours the Al_2O_3 significantly at 13.1 wt. % while MgO is 2.0 wt. %. The FactSage^{TM} calculations with 20 wt. % CaO showed a melting point of 1381 °C, however from 1312 °C there are two corundum (M_2O_3) left in the solid form, and the rest of the system is liquid slag. The Al_2O_3 corundum only accounts for 2 wt. % of these, the other is Fe_2O_3 as the temperature increases the iron complex melts into the slag. A particle with much lower Al_2O_3 content such as C-2 sees its corundum phase dissolve as early as 1180 °C degrees.

In particle C-10, the Al_2O_3/MgO ratio is more even with 15.0 wt. % Al_2O_3 and 8.3 wt. % MgO. The system follows a similar trend to that with the high Al_2O_3 content where at 1361 °C the corundum dissolves into the slag phase. However, a spinel ($\sim$44 % $Fe_3O_4^{[1-]}$) is still solid in the system and requires higher temperatures to melt. This turns full molten at 1512 °C. This high temperature diffusion into the slag phase is its reason for the high overall melting point.

In particle L-8, the Al_2O_3/MgO ratio is more in favour of the MgO with

Al_2O_3 at 2.6 wt. % and MgO at 11.9 wt. %. The progression of species in the system changes as the corundum does not interfere with the material becoming liquid. The spinel $(Fe_3O_4{}^{[1\text{-}]})$ follows the same trend as when the ratio of Al_2O_3/MgO is even. However, there is a third species, an MgO monoxide at less than 1 % that stays in the solid phase with the spinel. The spinel becomes molten at 1469 °C but the MgO requires the temperature to reach 1501 °C before the system is fully molten.

The addition of these materials will cause higher melting temperatures. However, the amount of this was less than 1 % of the particle, so most of the ore will be molten. In addition, the temperatures to reach a molten state is still lower than the iron ores melting point alone. These small particles of unmelted particles materials could be nucleation and agglomeration sites for the formation of accretions.

8.4.3 Basicity

As shown above, all the components in the iron ore particle have some effect on the reaction/melting behaviour of the particle. One way in which this can be represented is the basicity of the particle components. Hence a simple slag basicity calculation of the four impurities SiO_2, CaO, Al_2O_3 and MgO using equation 8.1 [118] is used. This gives all these materials a value to test against the melting point of these samples. For the calculation, the Fe_2O_3 content in the sample was disregarded, as it does not feature in the slag basicity calculations. The results can be seen graphically in Figures 8-10 and 8-11.

$$\frac{wt(CaO) + wt(MgO)}{wt(Al_2O_3) + wt(SiO_2)} = Basicity \tag{8.1}$$

The results show that a basicity calculation below 0.04 increases the melting temperature to the highest in this experimental matrix. This suggests that particles with very acidic slag require a higher temperature to melt in the reaction. This can suggest that the addition of CaO to the system this raises the basicity of the particle and thus helps to aid the melting once the threshold has been met.
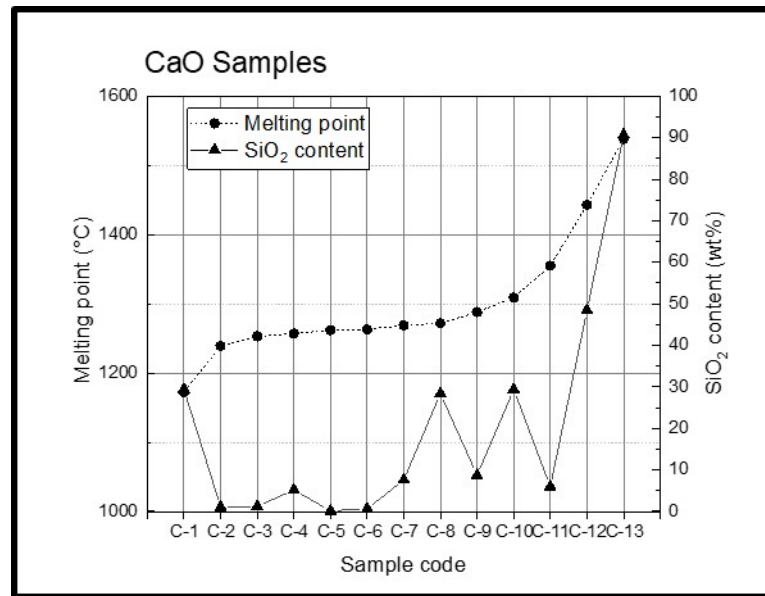
Figure 8-10: All CaO samples with the experimental melting point and the slag basicity.
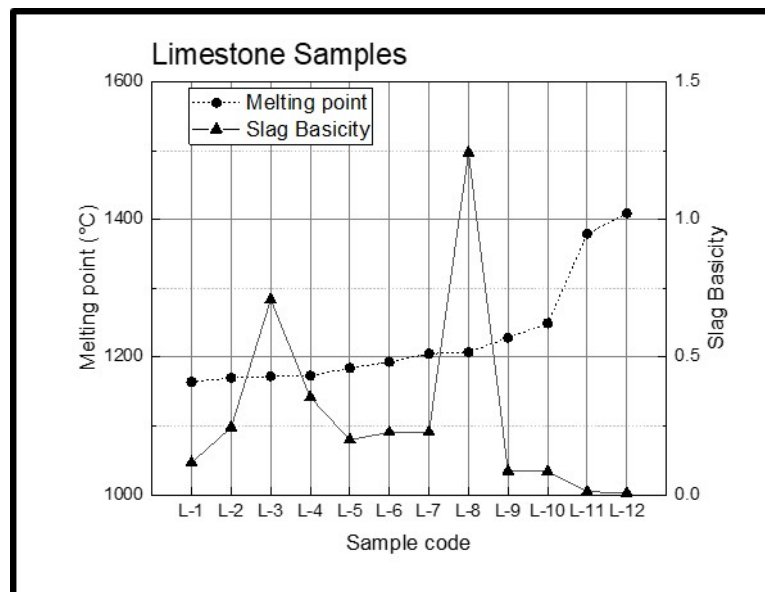
Figure 8-11: All limestone samples with the experimental melting point and the slag basicity.

This does not work as a rule, as the particles with higher basicity does not have the effect of lowering the temperature of the particles. The high acidity may just be showing the role that high SiO_2 has on the reaction.

8.4.4   Kinetic information gained from the particle measuring

From basic kinetics, the size of a material can affect the rate and the time of a reaction to reach completion. The overall size of a particle can determine the overall time that a particle takes to react. This is due to a larger particle having more to react with; hence, a larger particle will take longer to react. In the experiment, the sessile camera measured the contact size of the particle with the pellet. The experiment can also measure the size of a particle from two planes and observe the particles planer area as it reacts. The reaction progression of the particles with Ca-based materials is given in Figure 8-12 for CaO and Figure 8-13 for limestone.

The contact size of the particles does not seem to have any significant change in the rate of reaction. The results show that no matter the size of the particle the rate of growth is consistent between the starting size of contact and the rate of reaction. If this was the case the particles C-11 and L-10 should have had the steepest growth, however they followed a similar trend to all other particles. The size of the particles has no effect on the rate of the reaction and the period of time shows that 60 s was not sufficient time for the particle to complete the reaction with the pellet.
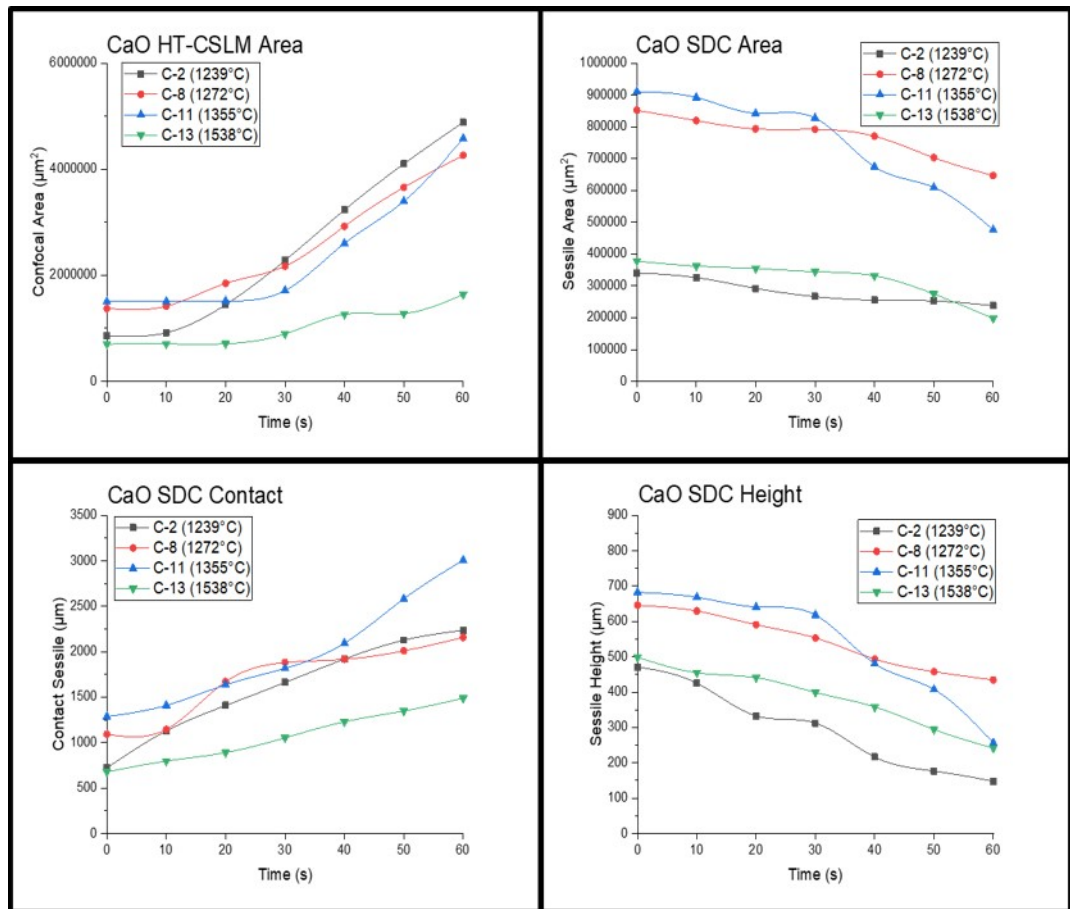
Figure 8-12: Graphs of how the particles that reacted with CaO changed over 60s by measurements of HT-CSLM planer area, SDC planer area, SDC contact and SDC height.
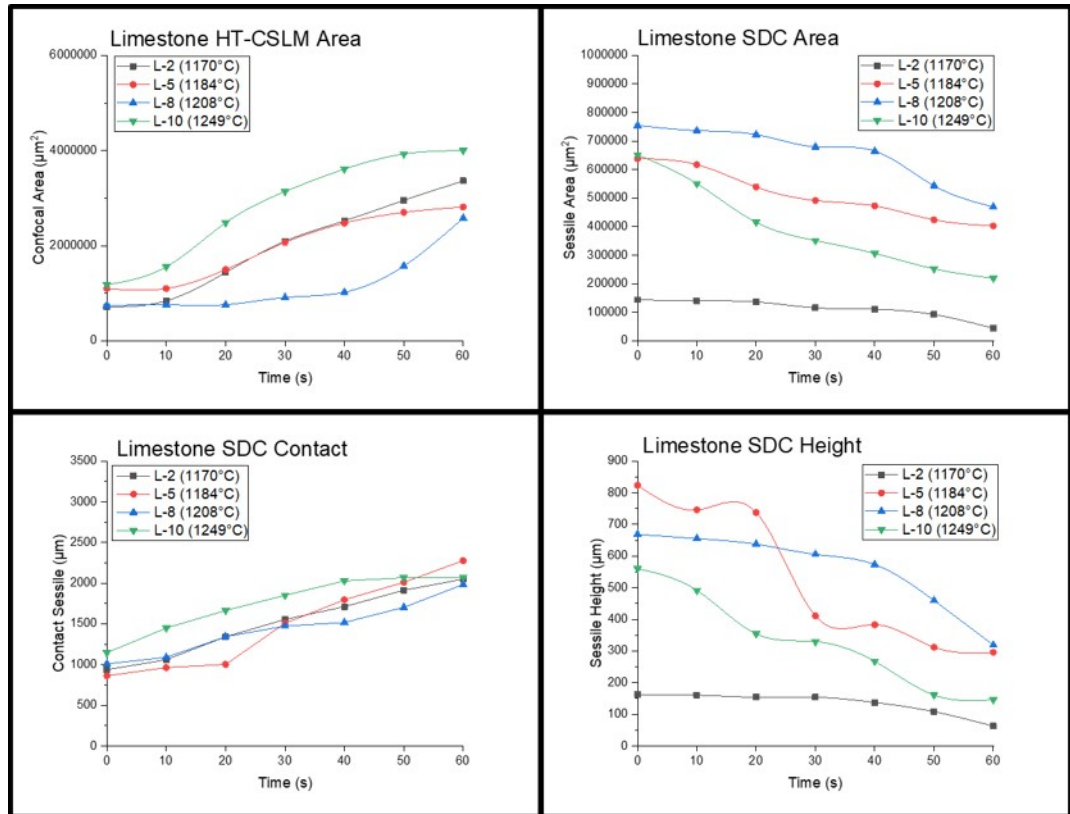
Figure 8-13: Graphs of how the particles that reacted with Limestone changed over 60s by measurements of HT-CSLM planer area, SDC planer area, SDC contact and SDC height.

The temperature that these particles reach activation should also determine the speed of the reaction between the two reactants. This is because the energy in the system is higher at higher temperatures. The results show that temperature does not improve the rate of reaction. The particle C-13 results were recorded at the highest temperature of all the particles. However, the results showed that it has the lowest rate of reaction in all the particles throughout the measured variables. This continued with the limestone samples as their reaction speed are more consistent indeterminate of the temperature that they are reacting.

The reaction rates between the iron ore particle and limestone offers a higher rate than that of the iron ore particle and CaO and is demonstrated in two ways. Firstly, the rate of reaction in the first 30 seconds of the reaction is higher in the limestone samples than in the CaO samples. The second is that the shape of the cure suggests that the limestone reactions are finished in the 60 s while this is not reached in the 60 s for the CaO samples.

122

Overall, the reaction rate seems to be determined more by the composition of the individual particles rather than the shape, contact area or temperature. The heterogeneous particle composition in a commercial iron ore means that the reactions with CaO will not be determined in the cyclone of the CCF. As the results showed that, none of these factors affected the reaction rate and thus the diffusion of CaO into the iron ore will be the determining step. CaO interaction will more likely occur on the walls of the CCF rather than in the free space of the furnace. If the particles were more homogeneous from particle to particle, the common factors of the kinetic would take more of an effect on the reaction rate.

These compositional effects are evident most in particle L-8 because it has extremely high CaO in the particle with a weight percentage of 16.5 wt. %. This affects the rate of reaction as it starts slowly and then increases quickly at 40 s. This suggest that the CaO in the system is reacting with the particle meaning it is less reliant on diffusion from the pellet. Using this material is quicker as the interaction with the pellet is though the contact point. Once the system requires more CaO then the interaction with the pellet will start and progress at a quicker rate.

8.5 Conclusion

This chapter conducted a detailed examination into the reaction of iron ore particles with CaO based materials in the CCF of the HIsarna process. The introduction of iron ore into the process suggests that the particles will be dispersed in the process and then react with the CaO. Material will be on a particle scale until the material flows on the wall of the CCF to the SRV. The heterogeneous nature of the composition from particle to particle (of iron ore) means the compositions will change the reaction with CaO based materials. The outcomes of this experimental data provide understanding on the influence of the impurities in the ore on the interaction with CaO.

Silica is shown to have the biggest effect on the melting of a particle with high content drastically increasing the melting point of the particle. The results show that a particle with over 40 wt. % of SiO_2 drastically increases the melting point and follows the phase diagram in terms of CaO, Fe_2O_3 and SiO_2. Suggesting that if HIsarna would use a high silica iron ore the chances of a more solid material may increase the probability of accretion formation. The other components such as alumina and magnesia do not need to be scrutinised as much as the silica in the ore selection. However, it is still important to have the knowledge of how they interfere with the components and increase the amount of CaO that is needed to decrease

the melting point. The melting point changes and the difference in how the material melts will also affect the viscosity as a non-Newtonian fluid. As lower temperature the slag could see the benefits of shear thinning increasing the flow. While knowledge of precipitate may increase the viscosity due to the shear thickening effects of the material which must be avoided for the formation of accretions.

The kinetics study conducted showed that the composition of each individual particle is more important than the normally beneficial aspects of kinetics. The contact size, temperature and other size aspects of the particle did not show an increase in the rate of reaction. If the particles were more homogeneous in terms of composition, these factors would be more visible in a similar test. This finding could lead to materials being selected on an engineering preference rather than chemical control requirements. These findings also give the possibility of using degraded CaL sorbent as a fluxing agent as the material is structurally compromised after the reactions in the process.

The results suggest that the reaction with CaO would benefit the process in terms of increasing fluidity of the ore at lower temperatures. The reaction would take place on the walls of the CCF rather than in transit in the CCF from the tuyeres. The CaO would have more time to diffuse into the bulk material on the walls of the CCF, where the iron would be in a more homogeneous form and closer to that given in the bulk iron ore composition.

Continuing the evaluation of different sources of CaO shows the benefits of newly formed lime like that found in (Chapter 7). The lower average melting point of the particles when reacting with limestone along with the comparisons of particles with similar composition, shows the similar trends evidencing that the reaction comes to completion at a quicker rate. This continues to suggest newly formed CaO from limestone has production benefits. HIsarna can benefit from using these sources of limestone without using kilns to form quick lime adding to the environmental benefits of the process. This may come with no drawbacks, however the high CO_2 content within the CCF may hinder the calcination process, as this is a product from the reaction. The production of CO_2 from the limestone could enrich the CO_2 production in the process and make the off gas more suitable for CCS.

The theoretical calculations that have been conducted from FactSage^{TM} with different amounts of CaO were calculated to see the effect on the melting point of each sample. The results show how a single composition reacts with a CaO and from this 20 wt. % of CaO has the greatest effect on most compositions of the material. It also gives an idea of how different levels of CaO will affect the fluidity of the materials in the CCF with the correct balance of iron ore and CaO.

Chapter 9

Conclusion

9.1 Accretion Growth and Removal

From the examination of the accretion sample in Chapter 6, the growth of HIsarna accretion has been theorised. The nature of the split structure and its properties orientation of the accretion in relation to the wall of the CCF including the time spent in the CCF have been clearly observed. The split structure ended up being a dense section and a porous section. The assumption was that the dense section was on the refractories of the CCF for a long period and thus was able to solidify slowly allowing a dense solid structure. The porous section suggests the material has not settled and captured gas from the CCF to form the pores, which also could be formed by a quick quench at the end of a trial. The dendritic crystals found in the dense section of the accretion also suggests a slower melting while the uneven needle crystalline structure is observed in the porous structure.

Historically alkali content most commonly the K_2O is the source of accretion growth and the compositions gained from EDS show that the accretion has as much as 4.4 wt. % in the sample compared to the 0.2 wt. % in the bulk iron ore. This suggests that alkali help the agglomeration to build on the refractory walls in CCF. However, the temperatures in the CCF reach upward to 1450 °C that is well above the melting point of most potassium complexes of $\sim$1100 °C. This means that the alkali content in the process should not have an influence on the accretion formation.

The measured solidification of the accretion showed that this occurs between 1463 °C and 1473 °C. This is in the region found in the CCF that sits between 1450 °C and 1500 °C. This also indicates that the sample could be solid in the CCF. This becomes more likely as HIsarna has an extensive cooling system in the refractories when compared to the ones found in the BF to protect the refrac-

tories. The cooling could be key to the build-up of the accretion in the contact with the refractories.

Viscosity of the accretion calculated by FactSage$^{\text{TM}}$ showed that the viscosities of the dense and porous sections were higher than the bulk iron ore which means as the material becomes the composition of the accretion the material flows slowly. The increase amount FeO in the system would increase fluidity but as the material in the CCF should have a Higher FeO content this is not enough so stop the formation of the accretion. The addition of CaO has the opposite effect on the viscosity making it flow slower however, the chemical benefits of a molten medium will benefit the flow more than a semi solid system that the calculation ignore.

From the result of Chapter 8 the residuals in the ore have shown to increase the melting point of the iron ore in the CCF. The most problematic residual is SiO_2 as this increase the melting point as seen by the particles with a high SiO_2 content had the highest melting point of all samples. The other components such as Al and Mg species have been shown to remain solid in a sample. These residuals could be the cause of agglomerations of solids and can be a reason to the growth of accretion.

9.2   Fluxing Agent

By adding a fluxing agent to the process with iron, ore in the CCF the melting point of the iron ore can be reduced significantly. As seen in the basic Fe_2O_3/CaO binary phase diagram, the addition of 20 wt. % of CaO can lower the melting point of Fe_2O_3 by 400 °C. This effect may hinder the building of accretion in the CCF and help improve the fluidity of the material and flow through to the SRV.

One of the main reported benefits of the HIsarna process as an alternative to BF ironmaking process is its flexibility of the primary materials with no need for pre-processing of raw materials. Iron ore does not need to be sintered and coal does not need to be coked or of coking standard. The possibility of extending this to the fluxing agent has been shown with limestone and BOF slag. Both limestone and BOF slag showed promising as a fluxing agent in effecting the melting point of iron ore in the CCF as all samples showed evidence of melting at temperature of 1350 °C.

The most effective Ca-based material was shown to be limestone from both the bulk 50/50 tests and the particle test observed in the research. This was due to the calcination of limestone to CaO being more reactive than pure CaO. This is accounted to the formation of a metastable form of CaO formed as CO_2 releases from the $CaCO_3$ and proved to have a massive effect on the liquid fraction of the iron ore. The benefit to HIsarna is a molten ore in the CCF and using limestone

instead of quicklime from kilns reduces the environmental benefits. BOF slag is a source of CaO that is readily available to modern integrated steel mills and can offer an interesting alternative with significant environmental benefits in terms of BOF slag or CaL sorbent utilisation.

9.3   Compositional effects

The compositional analyses of the particles of the industrial iron ore showed that on a particle level the compositions varied from the bulk compositions given. The resulting reactions showed the effects that impurities in the ore could have on the reaction with fluxing agents. In Chapter 8 the experiment showed that of the increased amount Fe_2O_3 content in the particle lowered the melting point to its lowest temperatures. SiO_2, Al_2O_3 and MgO all had negative effects on the fluxing of CaO.

High SiO_2 content disrupted the interaction the most and showed that a SiO_2 content of over 40 wt. % had a negative effect on the interaction with CaO. The interactions between Ca and Si oxides meant that the iron was left in solid form and was left to higher temperature to become molten. Other impurities like Al_2O_3 and MgO also effect the interaction with Ca-based materials, increasing the melting point of interaction as they hinder the diffusion of iron into the molten state. The Al_2O_3 causes the less effect than the MgO, but it is a more common complex in the ore.

For the HIsarna process, this means that ore selection can be examined to have the wanted effect of the addition of Ca based flux into the CCF. This can give reasons to the formation of accretions as the heterogeneous nature of the compositions of the particles may see increased amounts of SiO_2 or other components in the selected area. This could induce the growth of accretions despite the low levels of impurities in the ore being a low level.

9.4   Kinetics of diffusion

Limestone has proven to be more reactive than lime. This is shown in Chapter 7 by showing a more molten iron ore in the 50/50 test, an overall lower temperature and evidence of a more complete reaction in the particle experiment (Chapter 8). This is supporting the CaO produced from the calcination of limestone is more reactive. This is theorised to be due to a meta stable structure formed during this calcination process and the surface area of the escaped CO_2 is the reason behind this.

BOF slag is an interesting alternative fluxing agent when compared to lime and limestone. As shown in Chapter 7 that it forms a liquid medium and may

help the diffusion of CaO into the iron ore. The change from a solid solid reaction to a solid liquid reaction where the contact is increased, and diffusion times are quicker. This may also benefit the reduction of the iron ore if a liquid state is achieved at lower temperature as the reaction of CO and CO_2 will diffuse through a liquid. This will change from the diffusion through a solid particle as theorised in the shrinking sphere model.

The findings of the chemical composition being a driving factor in the interaction with the Ca based materials. This can offer the HIsarna process an interesting benefit as the size of the ore does not have to be dictated by chemical control. This allows the process to pick particles size for engineering preference to benefitting the running of the process.

Chapter 10

Future work

10.1   Furnace to Mimic HIsarna

The gas furnace (Figure 10-1) is a bespoke furnace developed for reactions to be done in reactive atmospheres; it has the capabilities to run at temperature up to 1600 °C under different atmospheres. The gases that can be used in the furnace are argon, nitrogen, hydrogen, carbon dioxide, carbon monoxide and methane. As it is capable of running with hydrogen, it has been designed with many safety features installed to minimise the risk of using this gas. The furnace has also been designed with two sampling bellows mounted above the reaction vessel and has the ability to sample while at high temperatures multiple times without interfering with the atmosphere in the reaction chamber.

Figure 10-1: Image of the gas furnace chamber and gas board with bellows.

The bellows also have the ability to add material to the reaction crucibles while under temperature and atmosphere. The capabilities of the furnace offer great opportunities for the research because the atmosphere is controlled including carbon dioxide, which is found in the CCF of HIsarna. The bellows allow for the addition of fluxes to samples, such as melting pre-reduced iron ore to simulate the drippings of the CCF then through the bellows add the flux to study the interaction.

During this PhD the development of this furnace in its design and instalment through rigorous testing and discussion. The instalment process came with the understanding of the system and functions such as the bellows and gas uses. This also came with the safety devices in place for this equipment to use hydrogen in a safe environment.

Following this a series of test was conducted for understanding the limitations of the furnace and reported potential design issues to the suppliers. These tests resulted in parts being changed that improved the atmosphere within the chamber

and added safety feature to the furnace. These changes improved the process in terms of functionality and running of the furnace.

The furnace has potential to be a valuable research method for the iron-making industry. The controlled atmosphere will allow reactions to be studied in bigger quantities than can be used in the HT-CSLM. However, the main feature is being able to safely use reducing atmospheres at high temperature. HIsarna and other novel ironmaking methods using a DRI method can benefit from the use of the furnace and these capabilities. The ability to add materials such as slags, fluxes or coal to another material via the bellows means that additions of materials under different atmospheres can be tested with a bespoke piece of equipment.

10.2 Continuing the work

Below are suggestions on how future work can be built on the findings of this body of work.

1. To investigate the reactions of limestone with the iron ore in a reducing atmosphere. This may indicate if a high concentration of CO_2 will affect the production of lime from limestone and confirm the benefits of using limestone are still viable in the process.

2. From the work and the use of the novel gas furnace established in the research group, benefits of adding CaO in the CCF increases the pre-reduction of the iron ore. This will also be able to determine what level of CaO has the best effect on the iron ore.

3. How the pre-reduced ore with a higher FeO content will change the interaction with Ca-based fluxing agents. Pre-reduced iron ore is the nature of the material in the CCF.

4. The kinetic research can be continued to study how the properties such as size, shape and temperature has on a particle with consistent composition, so the chemical factors seen driving the reactions in this work are negated. Providing a further understanding of the shape and size on the reaction.

5. To investigate how a bulk amount of iron ore in CCF conditions changes as a Ca-based material is added to the ore. This will reveal if adding a quick burst of CaO can remove accretion found in the CCF or study the diffusion of CaO into an accretion or iron ore on the walls of the CCF.

131

6. To implement the addition of CaO-based materials into the CCF and determine how this affects the process in terms of accretion and overall process. To aid the continuing the development including upscaling of HIsarna process.

Bibliography

[1] Jun Fu, Min Wang, and Qimin Cai. *Climate Mitigation and Adaptation in China*. Springer Singapore, 2022.

[2] Isnaldi R. Souza Filho, Hauke Springer, Yan Ma, Ankita Mahajan, Cauê C. da Silva, Michael Kulse, and Dierk Raabe. Green steel at its crossroads: Hybrid hydrogen-based reduction of iron ores. *Journal of Cleaner Production*, 340(February):130805, 2022.

[3] European Commission. *Communication from the Commision: A Roadmap for Moving to a Low Carbon Economy in 2050*, volume 112. 2011.

[4] Anne Carpenter. *CO_2 Abatement in the Iron and Steel Industry*. 2012.

[5] P D Burke and S Gull. *HIsmelt - The Alternative Ironmaking Technology*, chapter 7, page 61–71. Number December. Allied Publishers, 2002.

[6] Total Material. The cyclone converter furnace process (ccf), 2014.

[7] V.S. Ramachandran, P.J. Sereda, and R.F. Feldman. Mechanism of hydration of calcium oxide. *Nature*, 201:288–289, 1964.

[8] Harold R Kokal and Madhu G Ranade. Metallurgical uses fluxes for metallurgy. page 661–675, 1985.

[9] F. Van Loo, J.-F. Douce, M. Martinez Pacheco, M. Evrard, R. Pietruck, and H. Schmid. *Improved Sinter Mix Preparation While Using Challenging Raw Materials (IMSIMI) Research Fund for (European Commission EUR 27901)*. 2014.

[10] WorldSteel Association. *Steel Statistical Yearbook 2016*. 2016.

[11] SteelConstruction.info. Recycling and reuse, 2021.

[12] Hardarshan S. Valia. *Coke Production for Blast Furnace Ironmaking*. 1994.

[13] H.W. Gudenau, K. Mavrommatis, and A Babich. *Ironmaking*. Lecture te edition, 2002.

[14] Anne M Carpenter. *Use of PCI in Blast Furnaces*. Number September. 2006.

[15] Marcel Schulz, Klaus-Peter Paul Leuchtmann, Jin Hyung Chung, and Yong Mook Kang. Using modern coke oven technology at the new hyundai steel coke plant. In *Ais Tech 2015*, page 1–18. Association for Iron Steel Technology, 2015.

[16] Rohde W. Nashan, G. and K Wessiepe. Some figures and facts on the present status and new proposals for a future-oriented cokemaking technology. *Cokemaking International*, 12:50–55, 2000.

[17] A Babich and D Senk. *Coal use in Iron and Steel Metallurgy*, volume 2, chapter 12, page 267–311. Woodhead Publishing Limited, 1 edition, 2013.

[18] A Babich, D Senk, H. W Gudenau, and K Mavrommatis. *Ironmaking Textbook*. Aachen, Mainz GmbH, 2008.

[19] Lopamudra Panda, A. K. Sahoo, A. Tripathy, S. K. Biswal, and A. K. Sahu. Application of artificial neural network to study the performance of jig for beneficiation of non-coking coal. *Fuel*, 97:151–156, 2012.

[20] Andreas Orth, Nikola Anastasijevic, and Heinz Eichberger. Low CO_2 emission technologies for iron and steelmaking as well as titania slag production. *Minerals Engineering*, 20(9 SPEC. ISS.):854–861, 2007.

[21] Sushil Gupta and Veena Sahajwalla. *The Scope for Fuel Rate Reduction in Ironmaking Technical*. Number January. 2005.

[22] H M Lee and R W Zeigler. *The Blast Furnace Facility and Equipment*, chapter 9, page 643–698. The AISE Steel Foundation, 11 edition, 1999.

[23] P.L. Walker Jr, F Rusinko Jr, and L.G. Austin. *Gas Reaction of Carbon*, volume 11, page 133–221. Elsevier Inc, 1959.

[24] R.J Fruehan. The making, shaping, and treating of steel:. *Ironmaking Volume AISE Steel Foundation*, page 1999, 1999.

[25] Primetals Technologies. *COREX: Efficient and Environmentally Friendly Smelting Reduction*. 2015.

[26] Seetharaman Sridhar and Zushu Li. Can there be a sunrise in steel town? *Ironmaking Steelmaking*, 43(9):642–649, 2016.

[27] S.K Gupta and S.S Gupta. Corex process- one of the dynamic routes for gel making with special reference to the sucess of jvsl.

[28] Subrata Pal and Ashok Kumar Lahiri. Mathematical model of corex melter gasifier: Part i. steady-state model. *Metallurgical and Materials Transactions B*, 34B(February):103–114, 2003.

[29] Lawrence Berkeley. *The State-of-the-Art Clean Technologies (SOACT) for Steelmaking Handbook*. Number December. 2010.

[30] Primetals Technologies Austria GmbH and POSCO EC. The finex® process - eeconomical and environmentally at lower costs and emissions. *A joint venture of Siemens, Mitsubishi Heavy Industries and Partners*, 2020.

[31] W Hillisch and J Zirngast. Status of finmet plant operaction at bhp dri, australia. *Steel Times International*, page 20, Mar 2001.

[32] Sang Ho Yi, Moo Eob Choi, Do Hyung Kim, Chang Kuk Ko, Woo Il Park, and Sun Young Kim. Finex® as an environmentally sustainable ironmaking process. *Ironmaking and Steelmaking*, 46(7):625–631, 2019.

[33] Taehyeok Kim and Moo Eob Choi. *Feasibility Assessment for Recycling Copper Slag as Ferrous By-Products in FINEX®: An Alternative Ironmaking Process*, chapter Part V, page 221–228. TMS, 2019.

[34] Francesco Memoli, Federico Picciolo, Jeremy A.T. Jones, and Niccolò Palamini. The use of dri in a consteel® eaf process. *Iron and Steel Technology*, 12(1):72–80, 2015.

[35] Denys M. Lasar J. Birat J.P. Still G. Meijer, K. and B Overmaat. Ulcos: Ultra-low CO$_2$ steelmaking. *Ironmaking Steelmaking*, 36(4):249–251, 2009.

[36] K Meijer, C Guenther, and R J Dry. Hisarna pilot plant project. *InSteelCon*, (July):1–5, 2011.

[37] V.R Radhakrishnan and A.R Mohamed. Neural networks for the identifcation and control of blast furnace hot metal quality. *Journal of Process Control*, 10(6):509–524, 2000.

[38] Christian Sartorius and Stefan Zundel. *Technological Competition and Time Windows in Iron and Steel Production*, chapter 12, page 277. Edward Elgar Publishing, 2005.

[39] M Corbett, C Treatgold, P Granati, G Malgarini, J.M van Langen, and Koen Meijer. *The Converted Blast Furnace (CBF) and the Cyclone Converter Furnace (CCF)*. Number 21. 1995.

[40] Jacques Pilote. Future of hismelt® in india. *Steel Scenario Journal*, 21(March), 2012.

[41] Peter Klinger. Rio terminates kwinana hismelt plant. *The West Austrailia*, Jan 2011. NULL.

[42] Yue Zhengchao, Qing Shan, and Wang Hua. Numerical modelling of a slag-metal behavior of smelting reduction process: Ironmaking technology based on the hismelt. In ICEMI'09, editor, *The Ninth International Conference on Electronic Measurement Instruments*, page 482–485. IEEE, 2009.

[43] Koen Meijer, Chris Treadgold, Christiaan Zeilstra, Guss Keilman, Cor Teerhuis, Maarten Ouwehand, and J. van Boggelen. *HIsarna Experimental Campaigns B and C*. 2015.

[44] M. Mstsushima, S. Yadoomaru, K. Mori, and Y. Kaxai. A fundamental study on the dissolution rate of solid lime into liquid slag. *Iron Steel Inst. Jpn.*, 17:442–49, 1977.

[45] C.W Natalie and J.W Evans. Iron and steelmaking. *Iron and Steelmaking*, 6(3):101–109, 1979.

[46] Z. S. Li, M. Whitwood, S. Millman, and J. van Boggelen. Dissolution of lime in bos slag: from laboratory experiment to industrial converter. *Ironmaking Steelmaking*, 41(2):112–120, 2014.

[47] Gupta Sudhir Kumar, Anushuya Ramakrishnan, and Yung-Tse Hung. *Lime Calcination*, chapter 14, page 611–633. 2007.

[48] T. Shimizu, T. Hirama, H. Hosoda, K. Kitano, M. Inagaki, and K. Tejima. A twin fluid-bed reactor for removal of CO_2 from combustion processes. *Chemical Engineering Research and Design*, 77(1):62–68, 1999.

[49] Isabel Martínez, Gemma Grasa, Jarno Parkkinen, Tero Tynjälä, Timo Hyppänen, Ramón Murillo, and Matteo C. Romano. Review and research

needs of ca-looping systems modelling for post-combustion CO_2 capture applications. *International Journal of Greenhouse Gas Control*, 50:271–304, 2016.

[50] M. Alonso, N. Rodríguez, B. González, G. Grasa, R. Murillo, and J. C. Abanades. Carbon dioxide capture from combustion flue gases with a calcium oxide chemical loop. experimental results and process development. *International Journal of Greenhouse Gas Control*, 4(2):167–173, 2010.

[51] Dennis Y. Lu, Robin W. Hughes, and Edward J. Anthony. Ca-based sorbent looping combustion for CO_2 capture in pilot-scale dual fluidized beds. *Fuel Processing Technology*, 89(12):1386–1395, 2008.

[52] A. Charitos, C. Hawthorne, A. R. Bidwe, S. Sivalingam, A. Schuster, H. Spliethoff, and G. Scheffknecht. Parametric investigation of the calcium looping process for CO_2 capture in a 10 kwth dual fluidized bed. *International Journal of Greenhouse Gas Control*, 4(5):776–784, 2010.

[53] S. Plötz, A. Bayrak, A. Galloy, J. Kremer, M. Orth, M. Wieczorek, J. Ströhle, and B. Epple. First carbonate looping experiments with a 1 mwth test facility consisting of two interconnected cfbs. In *21st International Conference on Fluidized Bed Combustion*, page 421–428, 2012.

[54] H. Dieter, C. Hawthorne, A. R. Bidwe, M. Zieba, and G. Scheffknecht. The 200 kwth dual fluidized bed calcium looping pilot plant for efficient CO_2 capture: Plant operating experiences and results. In *21st international conferance on fluidized bed combustion*, volume 1, page 397–404, 2012.

[55] M. H. Chang, C. M. Huang, W. H. Liu, W. C. Chen, J. Y. Cheng, W. Chen, T. W. Wen, S. Ouyang, C. H. Shen, and H. W. Hsu. Design and experimental investigation of calcium looping process for 3-kwth and 1.9-mwth facilities. *Chemical Engineering and Technology*, 36(9):1525–1532, 2013.

[56] Anton I. Lysikov, Aleksey N. Salanov, and Aleksey G. Okunev. Change of CO_2 carrying capacity of CaO in isothermal recarbonation-decomposition cycles. *Industrial and Engineering Chemistry Research*, 46(13):4633–4638, 2007.

[57] Jun Young Kim, Naoko Ellis, C. Jim Lim, and John R. Grace. Effect of calcination/carbonation and oxidation/reduction on attrition of binary solid species in sorption-enhanced chemical looping reforming. *Fuel*, 271(September 2019):117665, 2020.

[58] J. Blamey, E. J. Anthony, J. Wang, and P. S. Fennell. The calcium looping cycle for large-scale CO_2 capture. *Progress in Energy and Combustion Science*, 36(2):260–279, 2010.

[59] Diego Alvarez and J. Carlos Abanades. Pore-size and shape effects on the recarbonation performance of calcium oxide submitted to repeated calcination/recarbonation cycles. *Energy and Fuels*, 19(1):270–278, 2005.

[60] Sara Yasipourtehrani, Sicong Tian, Vladimir Strezov, Tao Kan, and Tim Evans. Development of robust CaO-based sorbents from blast furnace slag for calcium looping CO_2 capture. *Chemical Engineering Journal*, 387(November 2019):124140, 2020.

[61] M. Kowalski, P.J. Spencer, and D. Neuschütz. *Binary Oxide System*, chapter 3.2.2, page 57–58. Verlag Stahleisen mbH, 2nd edition, 1995.

[62] Bert Phillips and Arnulf Muan. Phase equilibria in the system CaO-iron oxide in air and at 1 atm. O_2 pressure. *Journal of the American Ceramic Society*, 41(11):445–454, 1958.

[63] William M McKewan. Kinetics of iron ore reduction. *Transactions of the American Institute of Mining and Metallurgical Engineers*, 212:791–793, 1958.

[64] Yingxia Qu. *Experimental Study of the Melting and Reduction Behaviour of Ore Used in the HIsarna Process PhD thesis Yingxia Qu*. 2013.

[65] Stephen Spooner. *Quantifying the Transient Interfacial Area During Slag-Metal Reactions*. PhD thesis, University of Warwick, 2017.

[66] Michael D. Abràmoff, Paulo J. Magalhães, and Sunanda J. Ram. Image processing with imagej. *Biophotonics International*, 11(7):36–41, 2004.

[67] The international Organisation for Standardisation. *ISO:9035 Iron Ores- Determination of Acid Soluble Iron (II) Content- Titrimetric Method*. 1989.

[68] Andre N Assis, Jason Warnett, Stephen Spooner, Richard J Fruehan, Mark A Williams, and Seetharaman Sridhar. Spontaneous emulsification of a metal drop immersed in slag due to dephosphorization: Surface area quantification. *The Minerals, Metals Materials Society and ASM International*, 46B:568–576, 2015.

[69] S V Filatov, I F Kurunov, Ya M Gordon, D N Tikhonov, and S N Grachev. Extending the campaign life of an intensively operating blast furnace. *Metallurgist*, 60(9):17–22, 2017.

[70] A.J. Dzermejko, D.F. Baret, and D.H. Hubble. Ironmaking refractory systems. *Making, Shaping and Treating of Steel - Ironmaking Volume*, page 229–258, 1999.

[71] G.R. Rigby. Investigations relating to scaffolds in blast furnace. *Journal of Iron and Steelmaking*, 161(4):295–300, 1949.

[72] J Davison. Scaffold formation and removal in bf's. *Steel Times International*, 11(1):23, 1987.

[73] N.D. Yegorov, V.A. Kostrov, V.I. Solodkov, A.P. Kotov, and E.A. Ivanov. Scab formation in blast furnace and its avoidance during charging of zinc-containing burden. *METALLURG*, 25(5):12–15, 1980.

[74] J Williams. Investigations into scaffolding in blast furnaces and scaffold removal by blasting. *Stal und Eisen*, 84(2):57–62, 1964.

[75] T. Yamamoto Y. Sakamoto, T. Sakai and I. Kurashige. Diagnosis techniques for in-operation blast furnace linings. *Taikabutsu Overseas*, 2(1):65–70, 1982.

[76] T.P. Fredman. Accretion in the blast furnace stack- background factors. *Canadian Metallurgical Quarterly*, 41(4):475–486, 2002.

[77] C Sammuelsson. Impurity flow due to waste recycling. *MiMeR Report nb*, 3(4):2000, 2000.

[78] Maharshi Ghosh Dastidar, Bitan Kumar Sarkar, Manoj Kumar Mitra, and Rajib Dey. Effect of alkali on different iron making processes. *Material Science Engineering International Journal*, 2(6):304–313, 2018.

[79] R. Nicolle and W.K Lu. Waste oxide recycling in steel plants. In Department of Metallurgy Science and Materials, editors, *Proceedings of Symposium on" Waste Oxide Recycling"*, page 1974. McMaster University, 1974.

[80] Stephen Spooner, Claire Davis, and Zushu Li. Modelling the cumulative effect of scrap usage within a circular uk steel industry–residual element aggregation. *Ironmaking and Steelmaking*, 47(10):1100–1113, 2020.

[81] S.H. Brooks. Ref 8 s.h. brooks. tms/aime, 1968, pp. 18-25. In *TMS/AIME*, page 18–25. TMS, 1968.

[82] J.H. Stassburger. Weirton's new sintering plant. *Journal of Metals*, page 840–842, 1956.

[83] H. Wysocki and D Winzer. Condition of the refractory coating of two fire ranges after extinguishing. *Stahl und Eisen*, 96(13):618–624, 1976.

[84] M Iguchi, H Tokunaga, H Tatemichi, and Z Morita. The mechanism of thermal accretion (mushroom) formation and the bubble and flow characteristics during cold gas injection. *Int. J Multiphase flow*, 19(12):173–186, 1993.

[85] Conference Paper and Joel Kapusta Bba. The savard-lee shrouded injector: a review of its adoption and adaptation from ferrous to non-ferrous. In *Proceeding of copper*, number June, 2013.

[86] Mansoor Barati. *Application of Slag Engineering Fundamentals to Continuous Steelmaking*, volume 2, chapter 3.3, page 305–357. Elsevier Ltd., 2014.

[87] Mansoor Barati. *Application of Slag Engineering Fundamentals to Continuous Steelmaking*, volume 2, chapter 3.3.3. Con, page 305–357. Elsevier Ltd., 2013.

[88] An International Journal, Basak Anameric, and S Komar Kawatra. Mineral processing and extractive metallurgy review properties and features of direct reduced iron. *Mineral Processing and Extractive Metallurgy Review*, 28:59–116, 2007.

[89] B. Bhoi, A. K. Jouhari, H. S. Ray, and V. N. Misra. Smelting reduction reactions by solid carbon using induction furnace: Foaming behaviour and kinetics of FeO reduction in CaO-SiO_2-FeO slag. *Ironmaking and Steelmaking*, 33(3):245–252, 2006.

[90] Jose Henrique Noldin Jr. An overview of the new and emergent ironmaking technologies. *Raw Materials and Ironmaking*, (November):19–25, 2011.

[91] Koen Meijer, Christiaan Zeilstra, Cornelis Teerhuis, Maarten Ouwehand, and Jan Van Der Stel. Developments in alternative ironmaking. *Transactions of the Indian Institute of Metals*, 66(5–6):475–481, 2013.

[92] Amit Chatterjee and B.D Pandey. Chatterjee, amit pandey, b.d. *Ironmaking Steelmaking*, 8(6), 1981.

[93] Geiseler Eisenh. Properties of iron and steel regarding their use. *Slag Symposium*, page 1–14, 2000.

[94] Yan Junjie. Progress and future of breakthrough low-carbon steelmaking technology (ulcos) of eu. *International Journal of Mineral Processing and Extractive Metallurgy*, 3(2):15, 2018.

[95] Tobias S Hilding. *Investigation of Accretion Formation in Blast Furnace Shaft*. PhD thesis, Lulea Tenkniska Univeritet, 2001.

[96] J. C. van Dyk, F. B. Waanders, S. A. Benson, M. L. Laumb, and K. Hack. Viscosity predictions of the slag composition of gasified coal, utilizing factsage equilibrium modelling. *Fuel*, 88(1):67–74, 2009.

[97] Mao Chen, Dianwei Zhang, Mingyin Kou, and Baojun Zhao. Viscosities of iron blast furnace slags. *ISIJ International*, 54(9):2025–2030, 2014.

[98] Zhengchao Yue, Shan Qing, and Hua Wang. Numerical modelling of a slag-metal behavior of smelting reduction process: Ironmaking technology based on the hismelt. In *ICEMI 2009 - Proceedings of 9th International Conference on Electronic Measurement and Instruments*, page 4482–4485. IEEE, 2009.

[99] Peter Liovic, Murray Rudman, and Jong Leng Liow. Numerical modelling of free surface flows in metallurgical vessels. *Applied Mathematical Modelling*, 26(2):113–140, 2002.

[100] Zhiyuan Chen, Yingxia Qu, Christiaan Zeilstra, Jan van der Stel, Jilt Sietsma, and Yongxiang Yang. Thermodynamic evaluation for reduction of iron oxide ore particles in a high temperature drop tube furnace. *Ironmaking and Steelmaking*, 47(2):173–177, 2020.

[101] Wei Ti Chang, Chi Ming Lin, Yu Lang Su, Chia Chun Li, Yu En Chang, Jyun Ming Shen, and Weite Wu. Effect of FeO content on foaming and viscosity properties in $FeO-CaO-SiO_2-MgO-Al_2O_3$ slag system. *Metals*, 11(2):1–10, 2021.

[102] Zefeng Ge, Lingxue Kong, Jin Bai, Huiling Zhao, Xi CaO, Huaizhu Li, Zongqing Bai, Bernd Meyer, Stefan Guhl, Ping Li, and et al. Effect of CaO/Fe_2O_3 ratio on slag viscosity behavior under entrained flow gasification conditions. *Fuel*, 258(August):116129, 2019.

[103] Sharif Jahanshahi, John G. Mathieson, and Henk Reimink. Low emission steelmaking. *Journal of Sustainable Metallurgy*, 2(3):185–190, 2016.

[104] Mohammed A Tayeb and Stephen Spooner. Phosphorus: The noose of sustainability and renewability in steelmaking. 66(9):1565–1571, 2014.

[105] Bert Phillips and Arnulf Muan. Phase equilibria in the system CaO-iron oxide-SiO$_2$ in air. *Journal of the American Ceramic Society*, 42(9):413–423, 1959.

[106] D. R Glasson. Reactivity of lime and related oxides. i. production of calcium oxide. *Journal of Applied Chemistry*, 8(12):793–797, 1958.

[107] North America, United States, and South America. World crude steel production - summary the largest steel producing countries. (January):1–2, 2020.

[108] Ting Zhi Ren, Xin Jin, Hong Yan Ben, and Cheng Zhong Yu. Burden distribution for bell-less top with two parallel hoppers. *Journal of Iron and Steel Research International*, 13(2):14–17, 2006.

[109] Jose Manuel Valverde and Santiago Medina. Crystallographic transformation of limestone during calcination under CO$_2$. (41012):21912–21926, 2015.

[110] M. Kowalski, P.J. Spencer, and D. Neuschütz. *3.2.3 ternary Oxide System*, chapter 3.2.2, page 126–127. Verlag Stahleisen mbH, 2nd edition, 1995.

[111] Arnulf Muan. Trans metallurgical society. *Trans Metallurgical society AIME journal of metals*, 203(9):965/7, 1955.

[112] M. Kowalski, P.J. Spencer, and D. Neuschütz. *Binary Oxide System*, chapter 3.2.2, page 63. Verlag Stahleisen mbH, 2nd edition, 1995.

[113] Hao Liu, Yuelin Qin, Yanhua Yang, Qianying Zhang, and Nengyun Deng. Influence of Al$_2$O$_3$ content on the melting and fluidity of blast furnace type slag with low TiO$_2$ content. *Journal of Chemistry*, 2018:6, 2018.

[114] Kexin Jiao, Jianliang Zhang, Zhengjian Liu, and Chunlin Chen. Effect of MgO/Al$_2$O$_3$ ratio on viscosity of blast furnace primary slag. *High Temperature Materials and Processes*, 38(2019):354–361, 2019.

[115] Yacen Deng, Zengkun Dan, Xiaobo Yan, Qiangqiang Wang, and Shengping He. Investigation of rheological behavior for commercial mold slags. *Journal of Materials Research and Technology*, 9(5):9568–9575, 2020.

[116] Saki Kondo, Kenji Tateishi, and Nobuo Ishizawa. Structural evolution of corundum at high temperatures. *Japanese Journal of Applied Physics*, 47(1 PART 2):616–619, 2008.

[117] J. A. Ball, S. T. Murphy, R. W. Grimes, D. Bacorisen, R. Smith, B. P. Uberuaga, and K. E. Sickafus. Defect processes in $MgAl_2O_4$ spinel. *Solid State Sciences*, 10(6):717–724, 2008.

[118] Tao Jiang, Shuai Wang, Yufeng Guo, Feng Chen, and Fuqiang Zheng. Effects of basicity and MgO in slag on the behaviors of smelting vanadium titanomagnetite in the direct reduction-electric furnace process. *Metals*, 6(5):5–8, 2016.